Advanced laser frequency stabilisation systems for mobile strontium optical lattice clocks

by

Sruthi Viswam

A thesis submitted to
the University of Birmingham
for the degree of
DOCTOR OF PHILOSOPHY

Quantum Matter Research Group
School of Physics and Astronomy
College of Engineering and Physical Sciences
The University of Birmingham

September 2019

Abstract

Strontium optical lattice clocks have undergone vast developments in the past decade with world leading frequency stability and uncertainty records. Now, a lot of scientists are moving from laboratory based clocks to transportable, and portable clocks for applications including space, fundamental science, finance, and communication. The research team at the University of Birmingham are working towards developing transportable apparatus for studying fundamental physics, global positioning system (GPS), and geodesy applications. This thesis reports on the progress towards two different transportable strontium optical lattice clocks, which we will call 'miniclock' and 'Space Optical lattice Clock 2' (SOC2).

A diode-seeded tapered amplifier based narrow linewidth laser is developed and used to realise second stage cooling of strontium in miniclock apparatus. The laser has achieved a linewidth of 1 kHz after stabilising to a 3 cm long optical reference cavity. A multiple frequency stabilisation unit (FSU) for strontium lattice clocks is established. It is a robust, portable, and compact frequency stabilisation unit with a volume of 593 cm^3. Three different lasers are currently locked simultaneously to the FSU cavity, which could be extended to any number of lasers, enabling to use a single cavity for locking all the lasers required in a strontium lattice clock, except the clock laser. FSU is designed specifically for use in compact clocks. In the SOC2 system, realisation of clock transition and its characterisation are performed. A transition linewidth of 3 Hz is obtained for the SOC2 strontium clock. Further details and results are described in the thesis.

Acknowledgements

I would like to extend my gratitude to Kai Bongs, Professor and Head of Cold Atoms group in the University of Birmingham, for offering me a position in his Cold Atom's research group to pursue my doctoral studies. He has been a great inspiration and motivation through out the course. I acknowledge the funding from EU ITN project- FACT (id: 607493) under Marie Curie early stage researcher fellowships program. I also thank DSTL and QTea funding for the fulfilment of this project work. I am very grateful to Yeshpal Singh for his constant supervision and support towards me and rest of the Strontium team members.

My sincere thanks to the clock team members for making lab life memorable and enjoyable. I acknowledge Ole Kock, Wei He and Dariusz Świerad for introducing me into the cold atom experiments. Thank you for your sincere guidance. My gratitude to Joshua Hughues for his help and support during my second year of PhD. A lot of thanks to Markus Gellesch for your sincere support during my thesis writing period. I would also like to thank rest of the cold atoms members for all the supports you have given so far. I wish you all very best from the bottom of my heart.

I am thankful to Christian Lisdat and Uwe Sterr for allowing me to undertake my secondment at PTB on the SOC2 project. My sincere thanks to both of you for your sincere supervision and numerous fruitful discussions. Many thanks to Stefano Origlia and Pramod Mysore for supporting me as I was a beginner in clocks that time. I would also extend my gratitude towards Ali Masoudi and Stefan Vogt for numerous discussions that we made during my stay at PTB.

My gratitude towards Elizabeth Bridge for being a sincere supporter and friend. I am so thankful that you have given me an opportunity to visit NPL for two weeks for further research. It was a really good learning time for me.

I would like to acknowledge Steven Brookes and his team members in the mechanical workshop for manufacturing all required components for the project. You have played a major role in my PhD completion. Many thanks to Kathleen Hynes and Raquel Fernandez for being FACT project managers and constantly supporting all students including me within it.

Last but not least, I would like to express my sincere gratitude towards my beautiful family for giving cent percent support through out my life including PhD. I am extremely thankful to my parents and my husband for being my backbone. Without all your support and love, I would not have accomplished my research. Many thanks to my relatives and friends for your motivation, support, and encouragement. This made me stay strong. All of you made me feel that distance does not matter. I strongly believe in the grace of almighty without which I would not have completed anything.

Contents

List of Tables

List of Figures

Chapter 1

Introduction to time and frequency measurements

Time is one among the necessary and fundamental quantities from which many physical and mathematical derivations, and formulae are evolved. It also has played a crucial role in the evolution of the world and the mankind. The measurement of time has been a very important factor as the human life is highly dependent on it. The agriculture, travel, and development of science are among the list of things which are performed depending on time. This chapter gives an insight to the history of time keeping and the recent developments in the time and frequency measurements, and their applications.

1.1 Sundial to atomic clocks

We can feel, see, hear, weigh or even smell many of the quantities but, time is something that can be understood only by consciousness and observation. During ancient years, the appearance of the Sun was recorded to count the date and time. Later on, the rotation and revolution of the Earth around the Sun, and the revolution of the Moon around the Earth served as a clock and was used to regulate the daily and seasonal activities like sowing and harvesting of crops. These can be denoted as natural clocks. As time passed, the requirement for more precise time keeping increased. This led to the development of various time keeping mechanisms. During 3500 B.C, moving shadows were used to understand the time of the day. Later in 1500 B.C, sundials were developed by the Egyptians. It divided the sunlit hours of the day into 10 different portions.

The invention of the pendulum clock is described as one of the milestones in time keeping. It has a much better short term stability compared to natural clocks, water clocks, candles, and sundials. Pendulums can also divide and measure time into smaller portions, even to seconds and

more. The earlier models of the clock lost 15 s per day [9], and the later versions developed during 1920s achieved an accuracy of 1 ms per day [10]. The terms stability (precision) and accuracy (certainty) are widely used in the field of frequency standards and measurements. The section below explains the terms with suitable diagrams.

1.2 Stability and accuracy of a frequency standard

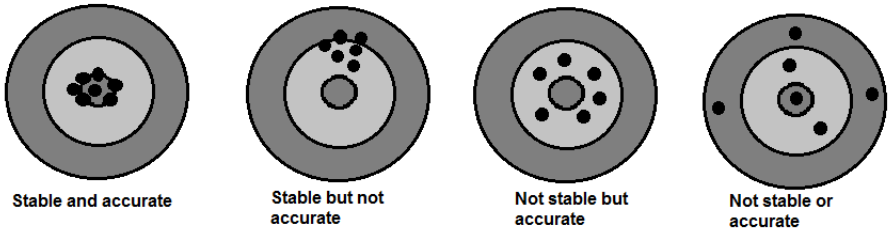

Figure 1.1: Schematic diagram illustrating the difference between stability and accuracy.

Stability and accuracy are the two factors with which a frequency standard is characterised. The difference between the two factors is illustrated in Figure 1.1. Stability can be described as the ability of an oscillator to generate the same result over several measurements and accuracy is the measure of how strictly the measured results match the expected values such the unperturbed natural transition frequency of an atom if the atom is used as a reference. For example, an oscillator is stable (precise) when it ticks several times per second, but it is accurate only if it maintains the same duration between each tick. By increasing the number of ticks per second (frequency), the precision with which the time determined can be increased. This may not necessarily lead to an accurate clock. Therefore, a reference should be added to an oscillator to maintain the same duration between each tick through a feedback loop. A simplified diagram of a clock with a reference and feedback is shown in Figure 1.2. A clock works by counting the ticks that its oscillator generates with respect to the reference.

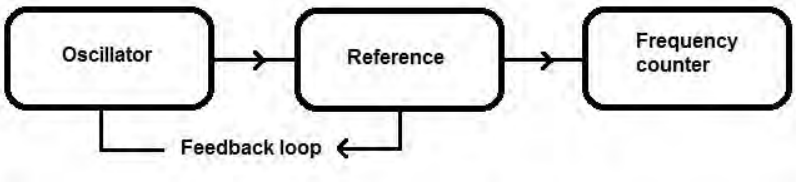

Figure 1.2: Schematic diagram illustrating a simple clock.

The need for higher precision (stability) led the scientists to invent clocks using devices that

can oscillate much faster than that can be detected using human eyes and senses. This thought paved the way for quartz clocks. It was invented by Warren A. Marrison in 1929. The resonant frequency of the quartz depends on the shape and size in which it is cut. It can be driven using an electric voltage. The quartz crystal is mounted within a feedback system to be used as a clock. High quality crystal clocks allowed time keeping with an inaccuracy approximately 1 ms per month [11]. Further developments in the design and manufacturing of the crystal led to an inaccuracy of 1 s in 100 years [12]. Along with the quartz crystal clocks, the 20th century also witnessed a huge progress in time keeping as atoms came into the forefront. Atomic clocks marked the new era of frequency standards.

1.3 Atomic clocks

Atomic clocks are developed by monitoring the frequency of the transition between different energy levels of an atom when it is placed in a radiation field. This is considered as a great advancement as atoms are natural resonators whereas a pendulum clock requires an exact length, and a quartz crystal needs to be cut very finely to the correct size.

Preparing an atom to be used as a clock has been a lengthy process as there were many questions to be answered: Which atom is the best to use? How to excite the atom between the energy levels? How to get the desired frequency? How to count the clock ticks? All these questions are answered as years progressed. A simple clock consists of a resonator, an oscillator, a counter, and a feedback loop. The signal from the oscillator is transmitted through the resonator leading to a vibration within the resonator. A signal that is proportional to the frequency difference between the oscillator and resonator is employed as a feedback to the oscillator using a loop which is composed of electronic circuits.

Isidor Rabi and his group in Columbia University were the first to introduce the idea of using atoms as frequency standards during 1930s. Later, they had to halt the work due to World War II [13]. He had informally discussed the idea of atomic frequency standards with a research group at National Bureau of Standards (NBS). Later in 1949, the first atomic frequency standard, based on ammonia molecule (NH_3), was developed at NBS by Harold Lyons and his group [14, 15]. A quartz crystal oscillator which generates a frequency near the resonant frequency of ammonia is used. When both frequencies match, ammonia absorbs most of the radiation. Any radiation that passes through the ammonia is used to correct the frequency of the crystal. The natural transition frequency of ammonia is 23,870,100,000 Hz. It is the frequency with which the nitrogen atom in the ammonia (NH_3) oscillates in the up and down direction through the base of the NH_3 pyramid structure. The ammonia clock has a fractional frequency uncertainty of 2×10^{-8} [11].

The low velocity and heavy size made caesium a popular candidate for developing as a frequency standard. Essen and Parry from the National Physical Laboratory, United Kingdom built the first caesium based frequency standard with an accuracy of 1×10^{-9} [16]. In 1967, the hyperfine transition in caesium atom was accepted as the definition of the second by the International System of Units (SI) [17]. The definition is:

"The second is the duration of 9,192,631,770 periods of the radiation corresponding to the transition between the two hyperfine levels of the ground state of the caesium 133 atom. This definition refers to a caesium atom at rest at a temperature of 0 K."

Caesium atomic clocks still continue as the international primary frequency standard having now reached a fractional frequency uncertainty of lower than 10^{-16} [18]. Ammonia and caesium clocks are referred to as microwave frequency standards as the vibration frequencies are in the microwave region of the electromagnetic spectrum. Caesium atomic clocks are reaching the limits of what is achievable with such systems, and their uncertainty is now limited by collisions between the atoms and effects due to the microwave power dependence [19]. Also, higher frequencies are preferred for clocks as they can provide a higher level of frequency stability. This led to the invention of atomic clocks working in the optical domain. Strontium [20], ytterbium [21], magnesium [22], mercury [23], calcium [24], cadmium [25], and aluminium [26] are the candidates in optical atomic clocks.

1.4 Atomic optical clocks

A straightforward approach to develop more stable (precise) clocks are by using frequency standards with higher transition frequencies. The solution was to move from mircowave to optical regime, thus paving way for atomic optical clocks. Frequency instability of the atomic clock is described using the following equation [27]:

$$\sigma_y(\tau) \approx \frac{\Delta\nu}{\nu_0\sqrt{N}}\sqrt{\frac{T_c}{\tau}}, \tag{1.1}$$

where ν_0 is the resonant frequency of the atomic transition, $\Delta\nu$ is the linewidth of the transition, τ is the averaging period, N is the number of atoms, T_c is the time required for completing one measurement cycle. The equation conveys that instability of the clock reduces when the linewidth of the transition and duration of measurement cycle decreases, and atom number and averaging time increases. The use of optical frequency standards instead of microwave frequency standards increased the quality factor (Q=$\nu_0/\Delta\nu$) of the clock. Along with Q, the number of atoms used in the stability measurement is important as it increases the signal to noise ratio (SNR) according to the equation 1.1.

Optical clocks are mainly of two categories: optical lattice clocks and ion clocks. Work described

in this thesis are related to optical lattice clocks. In an ion clock, only a single ion can be used since capturing multiple ions will result in Coulomb interaction between the ions leading to the trapped ions being pushed out of the trap. This led to the development of neutral atom based lattice clocks. Isolation from environmental perturbations along with low Doppler effect increased the importance of neutral atom lattice clocks, which are developed by trapping neutral atoms in optical lattice formed by the interference of the so called lattice laser which subsequently generates a standing wave pattern. Neutral atoms exhibit only short ranged interactions compared to long range Coulomb interactions of charged particles, therefore a larger number of atoms can be trapped in the lattice. Figure 1.3 shows the progress in fractional frequency uncertainty of microwave and optical clocks between the years 1955 and 2019. In the figure, caesium (Cs) and hydrogen (H) represent microwave frequency standards, whereas strontium (Sr), ytterbium (Yb), mercury (Hg), aluminium (Al) and calcium (Ca) are examples for optical frequency standards. Optical frequency standards have reached much lower fractional frequency uncertainty values than that due to microwave frequency standards as time progressed.

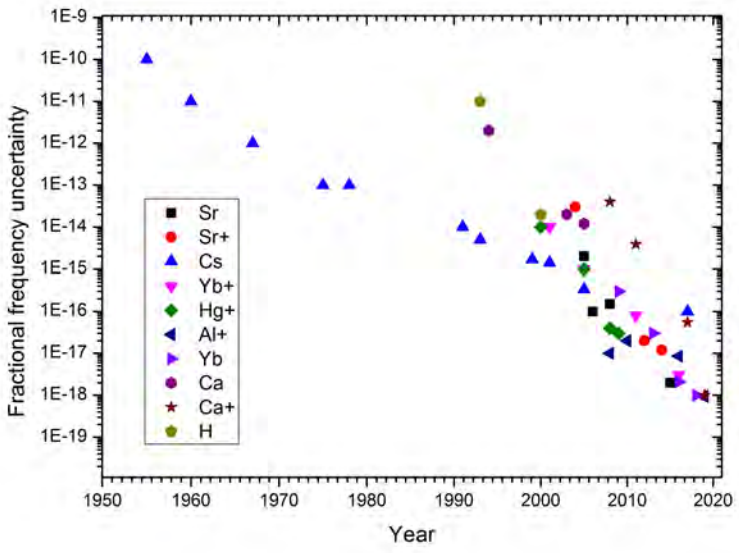

Figure 1.3: Progress in the fractional frequency uncertainty of atomic clocks over years. Graph recreated from [3, 4, 5, 6].

1.5 Different components of an optical clock

As mentioned in section 1.3, a clock is a device composed of three different units. It is the same with any clock from pendulum to the latest atomic optical clocks. The three units are an oscillator,

a frequency reference, and a counter. Figure 1.4 shows the schematic diagram of an optical lattice clock. This section will briefly describe each component in a clock.

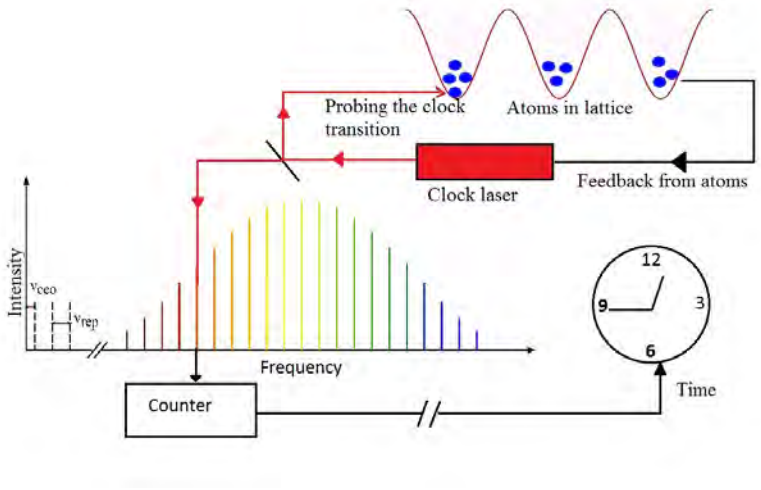

Figure 1.4: Schematic diagram of an optical lattice clock. It consists of a laser as an oscillator, atoms trapped in the lattice as reference, and frequency comb as a counter.

An oscillator in a clock is a device that generates the frequency that is finally to be converted into time. A frequency reference is required to keep the oscillator ticking at a constant frequency. Any change in the oscillation frequency with respect to the reference can be noticed, and a feedback from the reference can be provided to the oscillator to maintain the correct frequency. In an optical clock, a laser is the oscillator and an atomic transition is the reference. A laser, before being used to interrogate narrow-linewidth atomic transitions, is pre-stabilised to optical cavities which provides short-term stability to the laser. Since the laser is now locked to the optical cavity, care must be taken that there is no variation in the optical path length of the cavity as it can lead to a frequency shift. For example, a 1 fm length change in the optical path length of a 10 cm cavity will lead to a frequency variation of 4.35 Hz to a laser emitting 689 nm (435 THz). Therefore, materials used for manufacturing the spacers used in the optical cavities are chosen such that their expansion is very low: ultra-low expansion (ULE) glass is an example.

A narrow linewidth atomic optical transition is employed as the reference in an optical clock. The laser (oscillator) is used to interrogate the unperturbed atomic optical transition whose frequency ν_0 is given by:

$$\nu_0 = \frac{E_2 - E_1}{h}, \tag{1.2}$$

where E_2 and E_1 are the excited and ground state energy of the transition respectively, and h is the Planck's constant. The energy gap between the two states determine the frequency at which

the clock ticks. Chapter 5 explains the interrogation and measurement of such an optical transition of strontium atom.

With the oscillator and the reference, it is possible to obtain a precise and accurate frequency. However, counting the frequency of oscillations is an important task without which we are unable to determine the frequency. Microwave clocks have electronic counters to count the oscillations up to 50 GHz, but due to the higher 100s of THz frequency range, the optical clocks require an intermediate device to link the higher THz frequency to the electronic counter. Femtosecond optical frequency combs are developed to link the optical frequency to microwave frequencies. A beat note measurement of the optical reference frequency with a nearest known mode from the frequency comb results in the generation of a microwave frequency which can then be counted using an electronic counter. See section 1.6 for more details.

1.6 Optical frequency comb

Optical frequencies are larger by a factor of 10^4 - 10^5 compared to the microwave frequencies. Until 1996, it remained very difficult to count the optical frequencies. H. Schnatz and his group in Physikalisch-Technische Bundesanstalt (PTB), Germany introduced a way to bridge the frequency difference between the caesium clock (9.2 GHz) and calcium frequency standard (456 THz). They used a chain of several phase locked oscillators [28]. Later, in 1999, T.W. Hänsch and his group at the Max-Planck Institute for Quantum Optics developed the first frequency comb to bridge the gap of 18.39 THz between the 335 THz caesium D1 line and the fourth harmonic of the He-Ne laser stabilised to methane at 88.4 THz [29]. In 2002, a company named Menlo systems made the first commercial frequency comb. J.L. Hall and T.W. Hänsch received Nobel Prize in 2005 for their contributions to the development of frequency combs.

Frequency combs are used as frequency counters in optical atomic clocks. They are pulsed laser systems composed of equally spaced spectral lines with a fixed repetition rate. Figure 1.5 represents a frequency comb. The frequency of n^{th} comb line can be expressed as:

$$\nu_n = \nu_{ceo} + n.\nu_{rep}, \qquad \text{where} \qquad \nu_{ceo} = \frac{\Delta\phi\nu_{rep}}{2\pi}, \tag{1.3}$$

ν_{ceo} is the offset frequency and ν_{rep} is the repetition rate, and $\Delta\phi$ is the phase change.

The repetition rate of the frequency comb is measured using a photodiode and referenced to a Rb microwave frequency standard. The carrier envelope offset (*ceo*) of the modes, which occurs as a result of a varying phase occurring on the pulse trains, is measured using self-referencing technique in which the frequency of comb lines from different part of the frequency comb is compared by mixing both radiations on a photodiode to determine the ν_{ceo} (see [30] for details) and lock to the

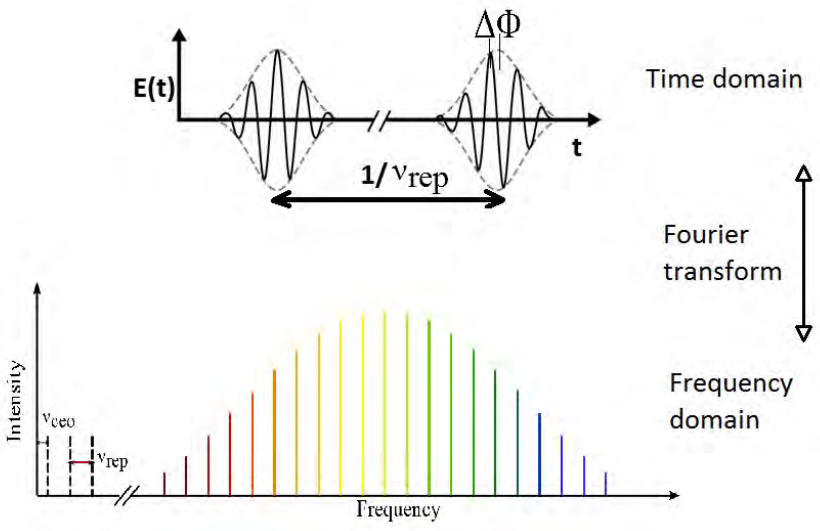

Figure 1.5: The top figure is the time domain signal, and the bottom figure is the frequency domain representation of an octave-spanning frequency comb.

Rb frequency standard so as to employ the comb as a frequency ruler. i.e,

$$\nu = 2(n\nu_{rep} + \nu_{ceo}) - (n'\nu_{rep} + \nu_{ceo}) = (2n - n')\nu_{rep} + \nu_{ceo}, \tag{1.4}$$

the equation reduces to ν_{ceo} when $2n{=}n'$, and the frequency offset can be measured in this way [31].

Once the repetition rate and offset frequency are known, the frequency of all the comb lines can be calculated. An unknown frequency can be measured by co-aligning the frequency with a comb mode. This will result in a beat frequency ν_{beat} which is the frequency difference between the unknown frequency and the comb line. With all the aforementioned values, the unknown laser frequency can be calculated from the following equation:

$$\nu_{unknown} = \nu_{ceo} + n''.\nu_{rep} \pm \nu_{beat}, \tag{1.5}$$

where n, n', n'' are mode numbers.

1.7 Applications of atomic clocks

Applications of atomic clocks include Global Navigation Satellite Systems (GNSS), chronometric geodesy, data transfer over wired networks, very long base line interferometry, test of fundamental physics etc...

1.7.1 Global Navigation Satellite System

Global Navigation Satellite System (GNSS) serves as a global navigation tool constituted by constellation of satellites such as USA's Global Positioning System (GPS), Russia's Global Navigation Satellite System (GLONASS), China's BDS and the European's GALILEO. GNSS provides navigation and positioning services globally and regionally.

The GPS is launched by the U.S. government in 1978. It has 31 satellites in orbit. It's made of three parts: network of satellites, ground stations on Earth and receivers (example: mobile phone). Satellites, which are at known positions, send radio wave signals to receivers. A receiver can collect information from three or four satellites to map the location very precisely. The signals from the satellites travel with the speed of light. Depending on the position of the satellite, the time taken by the signals from the satellites to reach the receiver varies. The signal also contains information about the satellite which sent that signal and the time at which the signal left the satellite. Such information from three or four satellites can locate the position on Earth with high precision. Atomic clocks are employed in these satellites for precisely measuring the time taken by the signal from the transmitter to reach the receiver [32]. Increase in the number of satellites enhances the accuracy of positioning. GLONASS, and BDS have 24 satellites each. GALILEO will have 30 satellites, of which 16 satellites have been launched into orbit.

1.7.2 Testing fundamental physics

The Atomic Clock Ensemble in Space (ACES) [33] and Search for Anomalous Gravitation using Atomic Sensors (SAGAS) missions [34, 35] are to be launched onto the International Space Station (ISS) for studying fundamental physics and relativity. ACES with Pharao, which is the caesium clock mounted, will study general and special relativity and try to find if there is any disagreement with the results that were previously obtained. SAGAS aims at exploring gravity in the solar system using quantum technology. It also will study the distribution of mass of the Jupiter and perform a number of gravitational physics tests.

1.7.3 Geodesy

Geodesy deals with the shape of the Earth. Atomic clocks are being used to understand even minor variation in gravitational potential at different places on the earth, and any variation in the potential is reflected on the atomic clocks as a shift in its frequency relative to the height difference in the location of each atomic clock [36]. The following equation represents the relation between difference in gravitational potential at two locations $U(z_1), U(z_2)$ and corresponding variation in atomic clock frequencies$f(z_1), f(z_2)$.

$$\frac{f(z_1)}{f(z_2)} \approx 1 - \frac{U(z_2) - U(z_1)}{c^2}. \tag{1.6}$$

Considering ΔU=$U(z_2)$-$U(z_1)$, corresponding height Δh difference between the locations can be obtained from the following equation:

$$\Delta U \approx \frac{GM_E \Delta h}{R_E^2}, \tag{1.7}$$

where G is Newton's gravitational constant, M_E is Earth's mean mass and R_E is Earth's mean radius. Further details regarding the equations and their derivations relating the atomic clock frequency variations to gravitational potential differences and the corresponding geoid heights are described in [37, 38]. Satellites or fibre links between different clocks can be used to compare the performance of clocks at different locations. The measurements are dependent on the gravitational potential at the locations where the clocks are situated. A recent fibre link clock comparison done by PTB and SYRTE were able to correct the gravitational redshift between the two strontium optical lattice clocks with an accuracy equivalent to 4 cm height [39].

1.8 Thesis outline

This thesis contains the work that has been performed by me during the doctoral course. It contains details about a frequency stabilisation cavity for strontium atomic clocks, development of a master oscillator power amplifier laser system and its application to a miniaturised strontium optical lattice clock (miniclock), and clock transition spectroscopy of a transportable strontium optical lattice clock under the SOC2 project. Each part is discussed in dedicated chapters.

Chapter 2 gives an introduction to the components and concepts required for developing strontium optical lattice clocks. I have included useful concepts on laser cooling and trapping of atoms, optical lattices, strontium optical lattice clocks, clock transition spectroscopy, and optical reference cavities.

Chapter 3 describes the narrow linewidth, high power master oscillator power amplifier (MOPA) based laser system at 689 nm that we have developed as a second stage cooling laser in strontium optical lattice clock. It includes the development and characterisation of the laser system, laser frequency stabilisation, and its application to obtain the very first red MOT from the miniclock apparatus.

Chapter 4 presents the development of a frequency reference cavity for strontium optical lattice clocks. It contains detail about the cavity assembly, the methods and results of the characterisation of the cavity under different conditions, and development and characterisation of a frequency stabilisation unit for locking multiple lasers.

Chapter 5 is dedicated to the work performed on a transportable strontium optical lattice clock. I am presenting the methods and results of clock laser spectroscopy performed on the strontium lattice clock (SOC2) apparatus.

Finally, **Chapter 6** gives a summary and outlook of the work presented in this thesis.

Chapter 2

Components and concepts of strontium optical lattice clocks

In this chapter we outline the components and basic concepts needed to design and build a strontium optical lattice clock. It covers laser cooling and trapping, interrogation of the clock transition, and optical reference cavities for laser frequency stabilisation.

Optical lattice clocks are one of the most studied clocks these days due to their world leading fractional frequency stability [40] and fractional frequency uncertainty [41]. In order to make an optical lattice clock, we need to use a narrow linewidth laser to accurately measure the energy difference between the two clock states of the atom. Strontium (Sr) and ytterbium (Yb) are widely used for optical lattice clocks. In our research group, we are working with strontium. In strontium, the clock transition is from $5s^2\ {}^1S_0$ to $5s5p\ {}^3P_0$ level due to its ultra-narrow linewidth, and requires a laser with a wavelength around 698 nm. The energy level diagram for strontium using the data from [42] is shown in Figure 2.1. See section 2.3 for details on the Sr energy level diagram.

There are a number of groups around the world working on strontium clocks. The details of the groups are tabulated in Table 2.1. Here in Birmingham we are working on building a compact transportable Sr lattice clock apparatus, which we refer to as the miniclock. We have chosen to work with the bosonic isotope of strontium (^{88}Sr) as opposed to the commonly used fermionic isotope (^{87}Sr) due to the large natural abundance and simple electronic structure of ^{88}Sr.

2.1 Basic concepts of laser cooling

The development and progress in the area of laser cooling paved the way for tremendous changes in atomic physics. Using this process, atoms can be cooled to ultracold temperatures, and can be used for studying fundamental as well as advanced science. Laser cooling is basically the use of

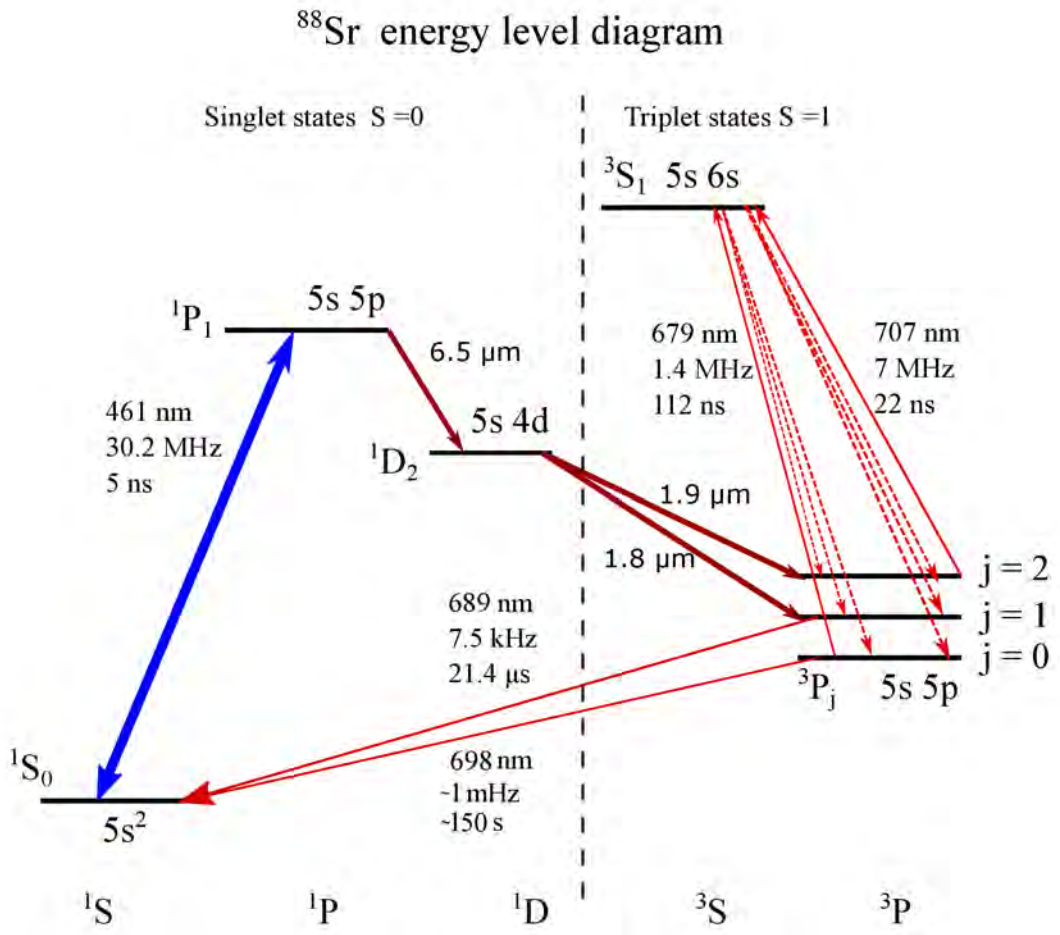

Figure 2.1: Energy level diagram for ^{88}Sr. First stage cooling (Blue MOT): $^1S_0$ to $^1P_1$, Second stage cooling (Red MOT): $^1S_0$ to $^3P_1$, Clock transition: $^1S_0$ to $^3P_0$, Repumping transitions: $^3P_2$ to $^3S_1$ and $^3P_0$ to $^3S_1$.

Table 2.1: Stability and fractional frequency uncertainty of strontium optical lattice clocks at different laboratories.

Species	Stability ($\sqrt{s^{-1}}$)	Uncertainty	Laboratory
^{87}Sr	4.8×10^{-17}	2×10^{-18}	NIST, PTB [43]
^{87}Sr	1.8×10^{-16}	7.4×10^{-18}	Uni. of Tokyo [44]
^{87}Sr	7×10^{-16}	2.1×10^{-17}	SYRTE [45]
^{87}Sr	2×10^{-16}	3×10^{-17}	PTB [46, 47]
^{88}Sr	3×10^{-15}	7×10^{-15}	LENS, PTB [48]
^{87}Sr	5×10^{-17}	1×10^{-17}	NPL [49, 50]
^{88}Sr	3×10^{-18}	2×10^{-17}	PTB, UoB [51, 7]

a carefully chosen laser beam to reduce the kinetic energy of atoms. The concept was proposed in 1975 by Schawlow and Hansch [52] and, Dehmelt and Wineland. Later in 1997, Steven Chu [53], Claude Cohen-Tannoudji [54], and William D Phillips [55] received the Nobel Prize for their contributions to laser cooling and trapping. In this section, a brief introduction to laser cooling is included.

When a photon from a light source such as a laser hits an atom whose velocity $\vec{v}$ is antiparallel to the propagation vector $\vec{k}$ of the photon, the atom absorbs the photon and due to the conservation of momentum, the photon momentum $\vec{p}_p$=$\hbar\vec{k}$ where $\hbar$ is $\frac{1}{2\pi}$ times Plank's constant (h) is absorbed by the atom. After absorbing the photon, atom gets excited to a higher energy level with a change in momentum from $\vec{p}_m$=$m\vec{v}$ to $m\vec{v}$+$\hbar\vec{k}$ where $\vec{p}_m$ and m are the atomic momentum and mass, respectively. The excited atom subsequently decays spontaneously by emitting a photon in a random direction, with a symmetric average distribution it lead to a net zero momentum and consequently a reduction in the velocity of the atom.

Due to the Doppler effect, the atom that's moving towards a laser beam will see a relative frequency shift (higher frequency) for the photons exiting the laser. Therefore, a lower detuned laser frequency is used for laser cooling. In other words, the photons moving in opposite direction to the atoms are Doppler shifted in respect to the resonance frequency. Let $\hbar\omega_0$ be the energy difference between two states in the atom, ω_0 indicates the angular transition frequency of the atom. The frequency of the light beam absorbed by the atoms is then given by [56]:

$$\omega_{ab} = \omega_0 + \vec{k} \cdot \vec{v} + \frac{\hbar k^2}{2m}, \tag{2.1}$$

and the emitted photon frequency is given by:

$$\omega_{em} = \omega_0 + \vec{k'} \cdot \vec{v'} - \frac{\hbar k^2}{2m}. \tag{2.2}$$

The second term on the right side of equations 2.1 and 2.2 corresponds to the Doppler shift between the atom under motion with respect to the stationary laboratory reference frame, and the third term gives the recoil frequency which is generated as a result of the energy and momentum conservation due to the transfer of photon momentum to the atom. In equation 2.2, the Doppler shift term averages to zero due to the average symmetric distribution of the emission process. As a result, the change in kinetic energy of the atom is:

$$\Delta E = \hbar(\omega_{ab} - \omega_{em}) = \hbar\left(\vec{k} \cdot \vec{v} + 2\frac{\hbar k^2}{2m}\right). \tag{2.3}$$

When $\vec{k}$ and $\vec{v}$ are antiparallel ($\vec{k} \cdot \vec{v} < 0$) and $\mid \vec{k} \cdot \vec{v} \mid > 2\hbar k^2/2m$, the kinetic energy of the atom is reduced, means atom is cooled.

The random absorption and the consequent emission of photons by the atoms result in heating of the atoms due to velocity fluctuations. The heating is proportional to the rate of scattering and

the cooling is proportional to the kinetic energy of atoms. At low atomic velocities, the heating is independent of kinetic energy and both the heating and the cooling reach an equilibrium at a certain average kinetic energy of the atoms resulting in the temperature to which the atomic cloud can be cooled. This is the Doppler cooling temperature [55]. i.e,

$$m\langle {v_i}^2\rangle = k_B T = \frac{\hbar\Gamma}{4}(\frac{\Gamma}{2\delta} + \frac{2\delta}{\Gamma}), \tag{2.4}$$

where δ is the frequency detuning between the unperturbed atomic frequency and laser, m is the atomic mass, v is the atomic velocity, Γ is the linewidth due to spontaneous emission from atomic excited state, k_B is the Boltzmann constant and T is temperature. In a two level atom, the lowest

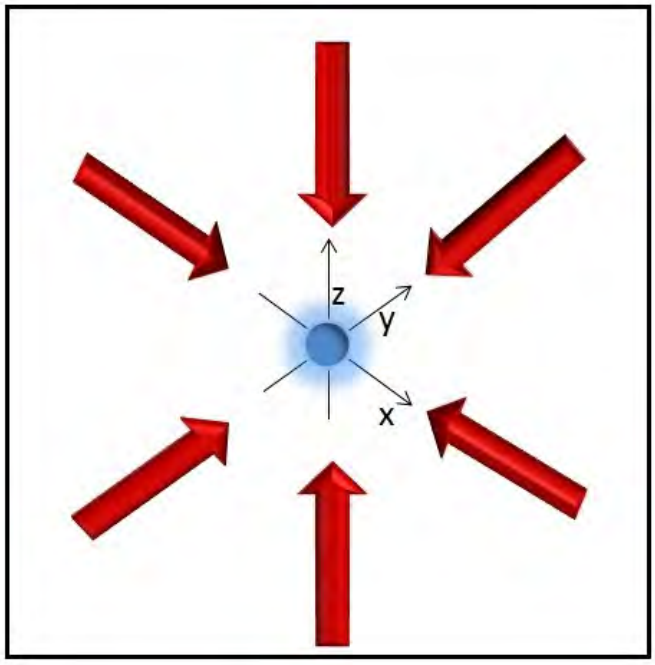

Figure 2.2: Three dimensional optical molasses.

attainable temperature of an atom is called Doppler cooling limited temperature and it is obtained when δ=-$\frac{\Gamma}{2}$ which is given by:

$$T_D = \frac{\hbar\Gamma}{2k_B}. \tag{2.5}$$

Another characteristic temperature is the recoil limited temperature T_r. It is the minimum temperature limit when the recoil energy experienced by the atom is larger than that due to the linewidth of the transition. It occurs as a result of the finite energy shift experienced by an atom when it absorbs a photon. T_r is given by,

$$T_r = \frac{\hbar^2|k|^2}{mk_B}. \tag{2.6}$$

The laser configuration to cool the atoms can be visualised as 'optical molasses' [57] due to the viscous force on atoms by the laser field. The Figure 2.2 shows a three dimensional optical molasses

where laser beams are shone from six directions. A pair of laser beams in the three coordinate axes result in cooling of atoms in three dimensions (3D).

The optical molasses configuration provides only velocity dependant force on the atom. In order to achieve perfect confinement, along with cooling, the atom needs to be trapped as well. To trap the atom, a spatially dependent magnetic field, which is provided by a pair of anti-Helmholtz coil, is also applied to the atom along with the laser beams. The process of using a combination of magnetic field and laser beams for the cooling and trapping of atoms is known as magneto-optical trapping (MOT).

2.2 Magneto-Optical Trapping (MOT)

Optical molasses can be converted to a magneto-optical trap (MOT) by the correct choice of polarisation of the laser beams and by introducing a magnetic field gradient. Figures 2.3 and 2.4 show the schematic diagram of a three and one dimensional MOT, respectively.

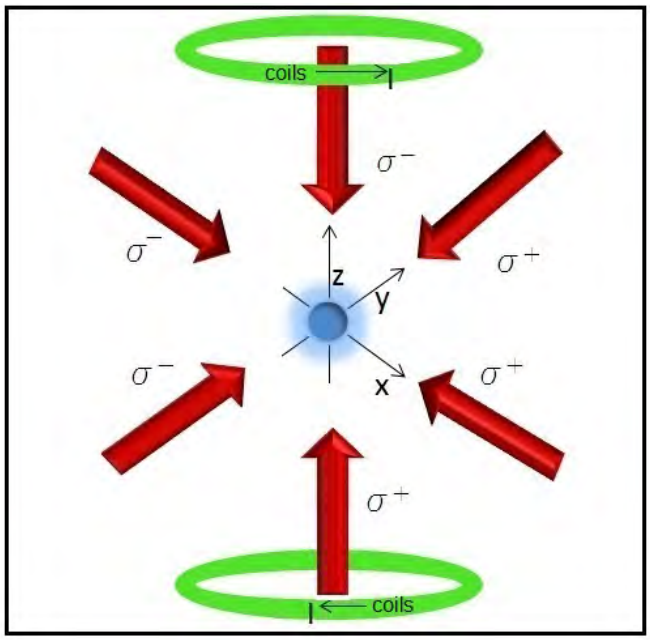

Figure 2.3: Three dimensional magneto optical trap configuration.

Circularly polarised laser beams with $+\sigma$ and $-\sigma$ polarisations are used in a MOT. The applied magnetic field breaks the degeneracy of the magnetic sub-levels in an atom. A pair of anti-Helmholtz coils are used to create the magnetic field gradient required for the MOT. At the centre of the MOT region, the magnetic field due to the coils cancel out and it is zero (B=0). Going away from the centre, where the field is zero, is a linearly increasing field that perturbs the energy levels, i.e, the external magnetic field results in the Zeeman splitting of the magnetic (m_j) sub-levels as:

$$\Delta E(z) = \mu m_j B(z) \rightarrow \omega_0(z) = \omega_0 + m_j \beta z, \tag{2.7}$$

where μ, $B(z)$, βz, and ω_0 are the magnetic moment, magnetic field, Zeeman shift, and resonant absorption frequency of the atom at zero field, respectively. This is depicted in Figure 2.4. Due to the Zeeman effect, the energy of the m_j=±1, 0 levels of the J=1 level change linearly relative to atom's position in the MOT.

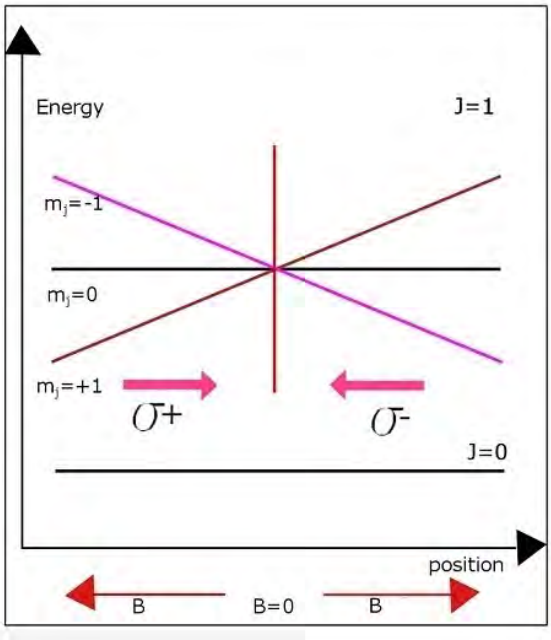

Figure 2.4: Schematic diagram illustrating one dimensional (1D) magneto-optical trapping of an atom with a J=0 → J=1 transition.

Consider a transition from J=0 to J=1 where the displacement of the atom from the trap centre is along the z axis. Here, the m_j=-1 of an atom is shifted away from the resonance at positions z>0 and the -σ polarised beam (left circularly polarised beam) is absorbed by the atoms at this level, and according to the selection rules these atoms are then pushed into the centre of the MOT (z=0) [58]. The force exerted by the circularly polarised laser beam and the spatially varying magnetic field on the atom in the MOT is given by [31]:

$$F_{MOT} = {F_{sc}}^{\sigma+}(\omega_L - kv - (\omega_0 + \beta z)) - {F_{sc}}^{\sigma-}(\omega_L + kv - (\omega_0 - \beta z)) \approx -2\frac{\partial F}{\partial \omega_L} kv + 2\frac{\partial F}{\partial \omega_0}\beta z. \tag{2.8}$$

This equation is valid for smaller atomic velocities $kv \ll \Gamma$ and Zeeman shift $\beta z \ll \Gamma$. Here, ${F_{sc}}^{\sigma+}(\omega_L)$ is the scattering force ($F_{sc} = \hbar\frac{\omega_L}{c}R_{sc}$), R_{sc} is the scattering rate, and $\frac{\partial F}{\partial \omega_L} = \frac{\hbar}{c}(R_{sc} + \omega_L \frac{\partial R_{sc}}{\partial \omega_L})$. The resonant frequency for $\Delta m_J = +1$ is given by $\omega_0 + \beta z$ and for $\Delta m_J = -1$ it is given by $\omega_0 - \beta z$ at position z. As the force is dependant on the frequency detuning ($\delta = \omega_L - \omega_0$), $\frac{\partial F}{\partial \omega_0} = -\frac{\partial F}{\partial \omega_L}$. As

a result, equation 2.8 can be written as:

$$F_{MOT} \approx -2\frac{\partial F}{\partial \omega_L}(kv + \beta z) \approx -\alpha(v + \frac{\beta z}{k}), \tag{2.9}$$

where $\alpha = 2\frac{\partial F}{\partial \omega}k$ is the damping coefficient. The atoms entering the region formed by the intersection of laser beams are slowed down and the position dependant force due to the magnetic field pushes the atoms to the centre of the MOT with zero field and trap them there. As can be seen, the combined action of strong damping and trapping makes MOT very easy to prepare cold atoms for various laser cooling experiments leading to atomic clocks, atom interferometers etc..

2.3 Strontium atom - laser cooling and trapping

Strontium is an alkaline earth element (Z=38) which is located in group 2 and period 5 of the periodic table. Due to the presence of two valence electrons in the atom, two different energy levels with parallel spin and anti-parallel spin are formed: triplet (S=1) and singlet (S=0). The energy levels (see Figure 2.1) are described using the Russel-Saunders notation $^{2S+1}L_J$ where S represents the total spin of the electrons, L is the orbital angular momentum and J is the total angular momentum [59]. There are four different stable isotopes for strontium as described in Table 2.2. They are ^{88}Sr, ^{86}Sr, ^{84}Sr, and ^{87}Sr with the maximum natural abundance for ^{88}Sr and the least for ^{84}Sr. ^{87}Sr is fermionic with nuclear spin I=9/2 while the others are bosonic isotopes with nuclear spin I=0. There is another isotope ^{90}Sr which has a radioactive half-life of 29.1 years [1]. All other unstable isotopes have half-lives of minutes, hours or days.

The 5s^2 ^{1}S$_0$ to 5s5p ^{1}P$_1$ transition to the singlet state at 461 nm is electric dipole allowed and it has a lifetime of 5.2 ns which corresponds to a linewidth (Γ) of $2\pi \times 30.2$ MHz [60]. This transition is used for the first stage cooling in strontium which allows to cool the atoms to the Doppler limit (T_D=0.7 mK). Red frequency detuned and circularly polarised 461 nm laser beams are used to interrogate this transition. The stage is known as blue MOT.

The 5s^2 ^{1}S$_0$ to 5s5p ^{1}P$_1$ transition is not fully closed, and approximately 1 in 50,000 atoms are lost to the 5s5p ^{3}P$_2$ and 5s5p ^{3}P$_1$ states via the 5s4d ^{1}D$_2$ state. Atoms in the 5s5p ^{3}P$_1$ state return to the ground state and complete the cycle. However, the atoms in the 5s5p ^{3}P$_2$ metastable state will be lost to the cooling cycle unless a repump scheme is employed. These atoms can be repumped to the 5s6s ^{3}S$_1$ state using 707 nm laser. From the 5s6s ^{3}S$_1$ state, the atoms decay to all the 5s5p ^{3}P states. From the 5s5p ^{3}P$_0$ state, the atoms are again repumped to the 5s6s ^{3}S$_1$ level using a 679 nm laser. Using the two repumpers, the atoms which decayed to the 5s5p ^{3}P$_{0,1,2}$ levels are transferred back to the ground state. After the atoms are repumped to the ground state, the effective loss rate from 5s5p ^{1}P$_1$ is 1.29×10^3/s, which is small when compared to the cooling transition rate of 2×10^8/s [61]. The use of repumpers can increase the number of atoms, MOT

Table 2.2: Different isotopes of strontium [1].

Isotope	Atomic mass	Natural abundance (%)	Nuclear spin	Half-life period
^{88}Sr	87.905612	82.58(1)	0	stable
^{86}Sr	85.909260	9.86(1)	0	stable
^{87}Sr	86.908877	7.00(1)	9/2	stable
^{84}Sr	83.913425	0.56(1)	0	stable

density, and the lifetime of the trap by a factor of 10. If no repumpers are used, then the Sr MOT loss rate can be written as [61]:

$$R_L = R_0 + \frac{\frac{I}{2I_0}}{1 + \frac{I}{I_0} + [\frac{2\delta}{\Gamma}]^2} A_{^1P_1 \rightarrow {}^1D_2} B_{^1D_2 \rightarrow {}^3P_2}, \tag{2.10}$$

where R_0 is the loss rate caused by the collisions with the background gas, and the second term describes the radiative decay of the atoms from the 5s5p ^{1}P$_1$ to the 5s5p ^{3}P$_2$ state via 5s4d ^{1}D$_2$ level; I and I_0 are the total laser intensity and saturation intensity (43 mW/cm^2), respectively. The Doppler limited temperature of the blue MOT, 0.7 mK, for the atoms is relatively high hence it would be difficult to interrogate these atoms to obtain the very narrow clock transition. Therefore, a second cooling stage is required.

The 5s^2 ^{1}S$_0$ to 5s5p ^{3}P$_1$ transition at 689 nm is used for the narrow line cooling in Sr [62, 63], which we refer to as the red MOT. This transition is between a singlet state and a triplet state (intercombination transition), so is forbidden by the angular momentum selection rules, but is weakly allowed due to the spin-orbit coupling and as a result the transition linewidth (Γ) is $2\pi\times$ 7.5 kHz with a lifetime of 21.4 μs. The red MOT stage is employed for further cooling of the atoms than that obtained in the first stage cooling. Unlike the blue MOT, the red MOT temperature is limited by the recoil momentum of the photons (T_r=450 nK). It is a recoil limited transition because the very narrow linewidth of the second stage transition means that the recoil momentum from the photon is the limiting factor and the Doppler temperature is never reached. A frequency stabilised 689 nm laser beam is sent to the chamber after overlapping with the beams of the blue laser. The red MOT is achieved in two stages, namely, broadband red MOT and single frequency (narrowband) red MOT. In a broadband red MOT, the frequency of the laser is modulated using an AOM before it is sent to the chamber [64]. This broad frequency range (1-2 MHz) which is red detuned to the transition frequency is sufficient to interact with all of the Doppler-shifted atoms in the relatively hot blue MOT. Without a modulated frequency, only atoms falling in a narrow velocity distribution within the whole velocity range can be cooled. This process ensures that a good number of atoms are captured and cooled in the red MOT stage.

Usually, atoms with temperature around 1 μK is achievable in this stage.

Phase space density defines the number of atoms occupied in a cube of de Broglie wavelength λ_{dB},

$$\lambda_{dB} = \sqrt{\frac{h^2}{2\pi m k_B T}}, \tag{2.11}$$

and phase space density, D

$$D = n\lambda_{dB}^3, \tag{2.12}$$

where n is the spatial density of atoms. Phase space density can be maximised by finding the best combination of temperature and atomic density in the MOT. In the SOC2 Sr optical lattice clock reported in Chapter 5, the phase space density of the blue MOT is 4.3×10^{-7} and the red MOT is 2.9×10^{-5}. Recently, a phase space density of 2×10^{-3} is reported for ^{88}Sr red MOT [65]. In optical clocks, we are interested in temperatures low enough to be trapped in a 1D optical lattice. Phase space density increases from blue MOT to red MOT, but it is still far away from the density that is typically required for Bose-Einstein Condensates (BEC). Higher phase space densities ($D \geq$2.612) are required in BEC, for more details see the publications [66, 67].

The $5s^2\ ^1S_0$ to $5s5p\ ^3P_0$ is the clock transition which in the bosonic isotopes is doubly forbidden both by the spin and angular momentum selection rules, ($\Delta S \neq 0$ and J=0 to J=0 transition), and the natural linewidth of the transition is almost zero while in fermions it is approximately 1 mHz. In the bosonic isotopes the transition can be induced using a magnetically induced spectroscopy technique [2]. This is the most important transition in strontium and is employed as the clock transition due to its ultra-narrow linewidth. Additionally, because it is a J=0 to J=0 transition, it is insensitive to external magnetic fields.

2.3.1 Optical lattice trap

Even though atoms trapped in a magneto-optical trap are ultra-cold (of the order of a few microkelvin), they need to be tightly confined in an optical lattice to be used as an atomic reference. An optical lattice is implemented by retro-reflecting a laser beam to form a standing wave with closely spaced potential wells where atoms can occupy. It is shown in Figure 2.5. This configuration gives a high intensity gradient from the nodes to the anti-nodes over $\lambda/2$ distance, thus increasing the trap depth.

The electric field generated by the interference of two counter propagating laser beams travelling in the z direction can be written as [31]:

$$E = E_0 \cos[\omega t + kz] + E_0 \cos[\omega t - kz]. \tag{2.13}$$

The resulting standing wave can be written in the form:

$$E = 2E_0 \cos[\omega t] \cos[kz], \tag{2.14}$$

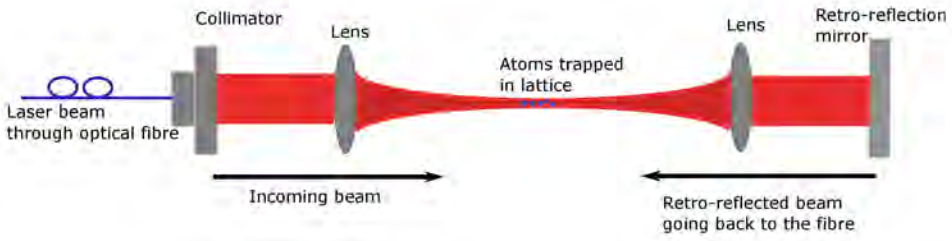

Figure 2.5: An optical lattice formed by retro-reflecting the laser beam.

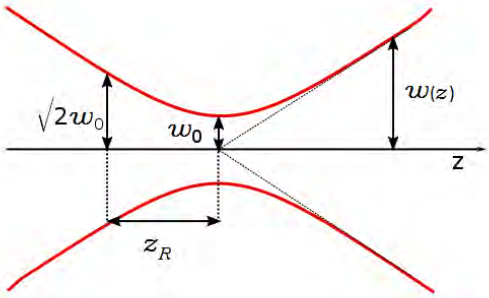

Figure 2.6: Gaussian beam radius $w(z)$ as a function of axial distance z.

where ω, k and E_0 are angular frequency, propagation vector, and electric field amplitude of the laser beam, respectively. The spatially varying intensity of the laser due to its electric field is $I(z)$=4 $I_0\cos^2(kz)$ and the potential (U_L) experienced by the atoms trapped in the optical lattice can be expressed as:

$$U_L \approx U_0 \cos^2[kz]\left(-1 + 2\frac{r^2}{w_0^2} + \frac{z^2}{z_R^2}\right), \tag{2.15}$$

where the potential depth of the lattice U_0 is,

$$U_0 = 4\frac{\hbar\Gamma}{8}\frac{I_0}{I_{sat}}\frac{\Gamma}{\delta}, \tag{2.16}$$

with δ=ω_0-ω_L is the detuning of the optical lattice laser frequency from the atomic resonance frequency ω_0, w_0 is the lattice beam waist radius, z_R is the Rayleigh range (see Figure 2.6), and r=$\sqrt{(x^2+y^2)}$ denotes the transverse distance from the lattice axis and z designates the longitudinal coordinate. The $\cos^2$ term spatially modulates the lattice potential in the axial direction with a $\lambda/2$ period and the confinement can be visualised as a harmonic potential. The resulting axial confinement frequency is:

$$\omega_z = k\sqrt{\frac{2U_0}{m}}, \tag{2.17}$$

and the radial frequency due to Gaussian confinement in the radial direction (orthogonal to the

axial) is given by:

$$\omega_r = \sqrt{\frac{4U_0}{mw_0^2}}. \tag{2.18}$$

In terms of lattice recoil frequency $\nu_{rec} = \frac{h}{2m\lambda^2}$, the equations 2.17 and 2.18 can be written as:

$$\nu_z = 2\nu_{rec}\sqrt{\frac{U_0}{h\nu_{rec}}}, \tag{2.19}$$

and

$$\nu_r = \sqrt{\frac{U_0}{m\pi^2 w_0^2}}, \tag{2.20}$$

where $\omega_z(\omega_r) = 2\pi\nu_z(2\pi\nu_r)$.

2.3.2 Strontium in optical lattice

Absorption of the clock laser photons at 698 nm during the clock transition interrogation will result in recoil frequency shift of the transition which limits the accuracy of the frequency standard. Once atoms are trapped in an optical lattice, the recoil frequency shift can be minimised. In the case of strontium, the atoms are trapped in the optical lattice after the second cooling stage. The lattice laser wavelength for the trap is chosen such that the AC Stark shift caused by the trap light is the same for the ground and excited states of the clock transition that is being interrogated. When both states are shifted by the same amount, the frequency of the clock transition remains unperturbed which is essential for a high accuracy clock [68, 69, 70, 71, 72]. The perturbed frequency can be written as,

$$\omega_p = (\omega_e - \omega_g) - \Delta\alpha(\omega_L, \hat{\epsilon}), |E(\omega_L, \hat{\epsilon})|^2/4\hbar \tag{2.21}$$

where $E(\omega_L,\ \hat{\epsilon})$ is the electric field of the trap laser, ω_e-ω_g=ω_0 is the unperturbed frequency and $\Delta\alpha(\omega_L,\ \hat{\epsilon})$ is the difference between the excited state (ES) and ground state (GS) dipole-polarisability ie., $\Delta\alpha(\omega_L,\ \hat{\epsilon})$= $\alpha_e(\omega_L,\ \hat{\epsilon})$-$\alpha_g(\omega_L,\ \hat{\epsilon})$. The second term in equation 2.21 vanishes if both polarisabilities coincide at a particular laser frequency ω_L and polarisation $\hat{\epsilon}$, and what we observe then is the unperturbed frequency [73] independent of the intensity of the trap laser $I_L \propto |E^2|$. This particular wavelength is known as the "magic" wavelength. The first demonstration of Stark shift cancellation with the magic wavelength was achieved by H. Katori and et al., [71]. They proved experimentally the magic wavelength at 813.420(7) nm [74]. Later on, P. Lemonde et al., recreated and confirmed more precisely the magic wavelength for Sr to be at 813.427 nm [75]. See Figure 2.7, it shows the magic wavelength at which the energy states $^1S_0$ and $^3P_0$ have the same light shift.

When the lattice trap potential is greater than the temperature of atoms ($U_0 > k_B T$), atoms mostly occupy lower vibrational levels and the optical lattice trap potential can be visualized as

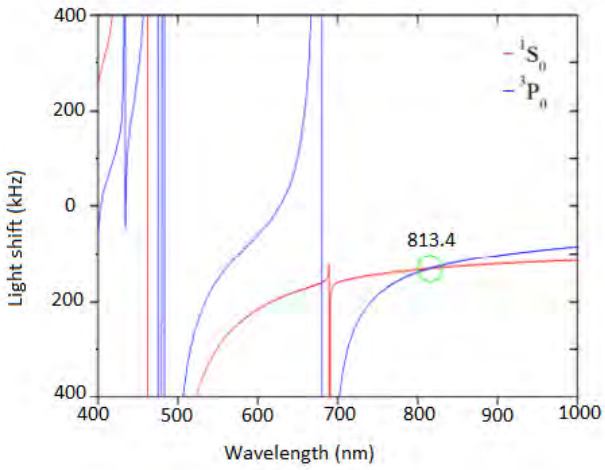

Figure 2.7: The Stark shift of $^1S_0$ and $^3P_0$ energy levels of Sr as a function of wavelength and it was initially found that at 813.420(7) nm, the light shifts coincides.

a quantum harmonic oscillator. The vibrational energy levels in a lattice site (see Figure 2.8) can be written as:

$$E_n = \hbar\omega_z \left(n + \frac{1}{2}\right), \tag{2.22}$$

where ω_z is the oscillation frequency. The regime where the recoil frequency shift of the transition due to the clock laser is much smaller than the oscillation frequency is known as the Lamb-Dicke regime. Atoms for the clock spectroscopy are prepared in the optical lattice, which satisfies the conditions for the Lamb-Dicke regime ($\eta \ll 1$, where $\eta = \sqrt{\frac{\omega_r}{\omega_z}}$; ω_r is the recoil frequency), for minimizing the residual Doppler shifts due to the probe beam [76, 73, 77, 78].

In a one dimensional optical lattice trap, the atomic population in the vibrational energy levels while interrogating a transition with frequency ω_0 and linewidth Γ with a laser frequency ω_L is characterised using a probability distribution function *P(n)*. Here, n describes the energy levels in the harmonic oscillator. The absorption signal generated by the atoms when a laser with frequency ω_L is used to obtain the clock transition is given as:

$$\sigma(\omega_L) \propto \sum_{n_i,n_f} P(n_i) \frac{|\langle n_f| e^{ikz} |n_i\rangle|^2}{1 + 4\left[\omega_0 - \omega_L + (E_{nf} - E_{ni})/\hbar\right]^2 / \Gamma^2}. \tag{2.23}$$

The absorption signal strength depends on the overlap between the atom's wave-function (e^{ikz}) in the initial (n_i) and final (n_f) energy states and the probability distribution function. If $\langle kz \rangle < 1$, then the matrix element in 2.23 can be expanded to:

$$\langle n_f| e^{ikz} |n_i\rangle \approx \langle n_f| ikz |n_i\rangle + \langle n_f| 1 |n_i\rangle = \delta_{nf,ni} + i2\pi z_0(\delta_{ni+1,nf}\sqrt{n_i+1} + \delta_{ni-1,nf}\sqrt{n_i})/\lambda, \tag{2.24}$$

where $z_0 = \sqrt{\hbar/m\omega_z}$ is the characteristic oscillator length and by squaring the matrix element in

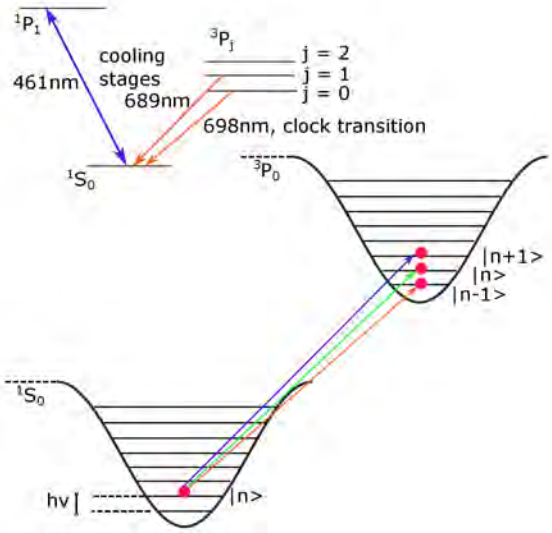

Figure 2.8: The vibrational energy states of the $^1S_0$ to $^3P_0$ transition is shown. Green arrow in the middle is the carrier frequency, accompanied by red and blue sideband frequencies where the motional state decreases and increases by 1.

2.24, we obtain:

$$Bn_f n_i \equiv |\langle n_f| e^{ikz} |n_i\rangle|^2 \approx \delta_{nf,ni} + \eta^2((n_i+1)\delta_{ni+1,n_f} + n_i\delta_{ni-1,nf}), \tag{2.25}$$

where η=$2\pi z_0/\lambda$ is Lamb-Dicke parameter which can also be expressed in terms of recoil and oscillation frequency as mentioned in the paragraph above.

The Lamb-Dicke regime occurs when the atom is tightly confined in the lattice potential well. The analysis of the equation 2.23 leads to the following conclusion: The atom with a natural transition frequency ω_0 absorbs a photon from the laser beam with frequency ω_L only if the laser frequency is equal to the sum of the natural transition frequency and the frequency between the motional energy states (E_{nf}-E_{ni})/$\hbar$. That is, ω_L=ω_0+(E_{nf}-E_{ni})/$\hbar$. The equation 2.25 gives three cases during which an atom absorb a photon:

When the atoms are trapped in the magic wavelength (n_i=n_f), the change in motional quantum number is zero and the last two terms of the equation 2.25 become zero. The atomic transition then occurs between n_i and n_f energy states when ω_L=ω_0. The frequency ω_0 is then called the carrier frequency.

When n_i-n_f=1, $\delta_{ni+1,n_f} \neq 0$, and the atoms absorb only when the laser frequency ω_L=ω_0+ω_z. This is called the blue sideband frequency as it is higher than the carrier frequency.

When n_i-n_f=-1, $\delta_{ni-1,n_f} \neq 0$, and the atoms absorb only when the laser frequency ω_L=ω_0-ω_z. This is called the red sideband frequency as it is lower than the carrier frequency.

The conditions are described in the figure 2.8. The conclusions are made by assuming that the atoms trapped in the lattice potential depends on the position z as z^2. But in actual case, the position dependence is $\cos^2(kz)$. This leads to anharmonicity in the trap. Trap anharmonicity modifies the energy of the motional energy states in the lattice trap. However, if the lattice is formed at the magic wavelength, then the change in the trapping potential for the ground and excited energy states are the same and it leads to a net zero trap anharmonicity on the carrier frequency.

2.4 The forbidden clock transition in ^{88}Sr

The ultra-narrow transition, $5s^2\ ^1S_0$ to $5s5p\ ^3P_0$, in ^{88}Sr is doubly forbidden due to the selection rules, as $\Delta S=1$ and $J=0\rightarrow0$. The change in spin and angular momentum are forbidden here. There are a number of ways the transition can be induced, in order to make it accessible for use in an optical clock. The initial concepts used two photon and three photon electromagnetically induced transparency to induce a transition in the doubly forbidden levels [79, 80]. However, the equipment required for the experiment make the set-up more complex due to the need of more laser systems. In 2006 A.V Taichenachev et al. proposed a magnetically induced clock transition [2].

2.4.1 Magnetically induced spectroscopy

In magnetically induced spectroscopy (MIS), a magnetic field B is introduced to induce the clock transition $5s^2\ ^1S_0$ to $5s5p\ ^3P_0$ by mixing the $5s5p\ ^3P_1$ and $5s5p\ ^3P_0$ states. The transition between $5s5p\ ^3P_1$ and $5s^2\ ^1S_0$ is weakly allowed due to the selection rule $J=1\rightarrow0$ ie., $\Delta J=1$. Therefore, by mixing the $5s5p\ ^3P_1$ and $5s5p\ ^3P_0$ using a magnetic field, it is possible for the $5s5p\ ^3P_0$ level to obtain a small admixture of the atoms in the $5s5p\ ^3P_1$ level. This allows a weak transition between the $5s5p\ ^3P_0$ and $5s^2\ ^1S_0$ states. Consider Figure 2.9 for detailed explanation on MIS: in order to excite the doubly forbidden clock transition from $|1\rangle$ to $|2\rangle$ at a frequency ω_{21}, a static magnetic field B is applied which mixes the $|2\rangle$ and $|3\rangle$ levels which are split by Δ_{32} frequency. The coupling matrix element Ω_B due to the magnetic field mixing is given by [2]:

$$\Omega_B = \frac{\langle 2|\,\hat{\mu}\cdot B\,|3\rangle}{\hbar}, \tag{2.26}$$

where $\hat{\mu}$ is the operator for the magnetic dipole moment. If $|\frac{\Omega_B}{\Delta_{32}}| \ll 1$, then the $|2\rangle$ state gets partly admixtured from the state $|3\rangle$ due to the static field, B. That is,

$$|2'\rangle = |2\rangle + \frac{\Omega_B}{\Delta_{32}}\,|3\rangle\,. \tag{2.27}$$

A laser beam with electric field E and frequency ω can create a resonant transition between the $|1\rangle$ and $|2\rangle$ states by acting via the intercombination states $|1\rangle$ and $|3\rangle$. The Rabi frequency of this intercombination transition $|1\rangle$ to $|3\rangle$ is given as:

$$\Omega_L = \frac{\langle 3|\, \hat{d} \cdot E\, |1\rangle}{\hbar}, \tag{2.28}$$

where $\hat{d}$ is the operator for the electric dipole moment. A resonance frequency ω=ω_{21} occurs between the doubly forbidden states $|2\rangle$ and $|1\rangle$ due to the admixture of $|2\rangle$ and $|3\rangle$ in the presence of the static magnetic field.

The effective Rabi frequency for the induced transition from $|2'\rangle$ to $|1\rangle$ state is:

$$\Omega = \frac{\Omega_B \Omega_L}{\Delta_{32}}. \tag{2.29}$$

The natural linewidth of the magnetically induced transition γ' depends on the linewidth γ and Rabi frequency of the intercombination transition between $|1\rangle$ and $|3\rangle$, Rabi frequency of the forbidden level, and the frequency difference between $|2\rangle$ and $|3\rangle$ levels. It is given by:

$$\gamma' = \gamma \frac{\Omega_B^2 + \Omega_L^2/4}{\Delta_{32}^2}. \tag{2.30}$$

Introducing the second order Zeeman shift Δ_B and the light shift Δ_L of the transition frequency between $|1\rangle$ and $|2\rangle$, the effective Rabi frequency can be modified as:

$$\Omega = 2\sqrt{|\Delta_B \Delta_L|}, \tag{2.31}$$

where,

$$\Delta_B = -\frac{\Omega_B^2}{\Delta_{32}} \qquad \text{and} \qquad \Delta_L = \frac{\Omega_L^2}{4\Delta_{32}}. \tag{2.32}$$

Different combinations of Δ_B and Δ_L can be used to generate the Rabi frequency providing flexibility to perform the experiment.

Equation 2.29 can be modified by considering the vector form of the applied electric and magnetic field:

$$\Omega = \frac{1}{\hbar^2} \frac{\langle ||\, \mu\, || \rangle \, \langle ||\, d\, || \rangle \, (B \cdot E)}{\Delta_{32}}, \tag{2.33}$$

where $\langle ||\mu|| \rangle$ is the reduced matrix of the magnetic dipole moment on the transition from $|3\rangle$ to $|2\rangle$ and $\langle ||d|| \rangle$ is the reduced matrix of the electric dipole moment on the transition from $|1\rangle$ to $|3\rangle$. $\langle ||\mu|| \rangle$ is equal to $\sqrt{2/3}\mu_B$ for the even isotopes of strontium; μ_B is the Bohr magneton. Equation 2.33 can be rewritten by combining $\langle ||\mu|| \rangle$ and $\langle ||d|| \rangle$ into a constant α which gives the value of the Rabi frequency induced per unit of both magnetic and electric fields.

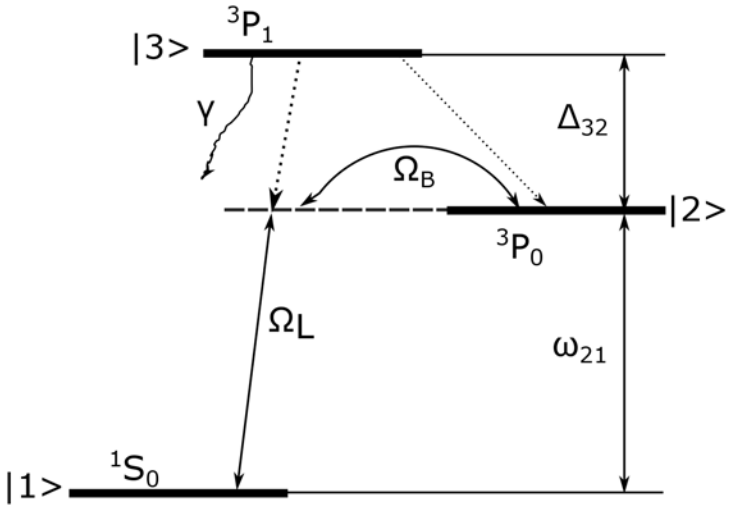

Figure 2.9: Illustration of magnetic field induced transition in $^3\mathbf{P}_0 \rightarrow {}^1\mathbf{S}_0$ levels in the alkaline earth elements [2].

Table 2.3: The constants which are used for the calculation of magnetically induced transition in ^{88}Sr [2].

Δ_{32}	γ	α	κ	β	ζ
THz	kHz	Hz/(T$\sqrt{(mW/cm^2)}$)	mHz/(mW/cm^2)	MHz/T^2	dimensionless
5.6	7.5	198	-18	-23.3	0.30

$$\Omega = \alpha\sqrt{I}|B|cos\theta, \tag{2.34}$$

where α gives the rate of induced transition and I is the laser beam intensity, and θ is the angle between the electric field due to laser beam and the linearly polarised magnetic field. Equation 2.34 can be written in terms of Zeeman shift Δ_B=βB^2, where β is the Zeeman shift coefficient, and Stark shift Δ_L=κI, where κ is the Stark shift coefficient, as:

$$\Omega = \zeta\sqrt{|\Delta_B\Delta_L|}cos\theta, \tag{2.35}$$

where ζ is a dimensionless coefficient which is equivalent to $\alpha/\sqrt{\beta\kappa}$ which is used to relate the induced field shifts with the excitation strength. The parameters used to find the Rabi frequency of transitions are solely determined by the atoms. The spectroscopic parameters for strontium atom are tabulated in 2.3. These can be employed for finding Rabi frequencies of transitions as done in section 5.4.2. A.V Taichenachev et al. have reported the constants for Sr, Yb, Ca, and Mg in [2]. MIS is the approach we plan to use in our strontium optical lattice clock.

2.5 Clock frequency measurements

A strontium optical lattice clock system is ready for clock transition frequency measurements after the following steps: first stage cooling (461 nm), broadband second stage cooling (689 nm), single frequency second stage cooling (689 nm), loading atoms in the lattice (813 nm), and spin state preparation (see section 2.4.1). A magnetically induced ultra-narrow transition can be used as a 'clock' by locking the frequency of a pre-stabilised clock laser (698 nm) to the transition. A π-pulse is used to excite the transition. If the π-pulse is exactly at the clock frequency, then all the atoms are expected to transit from the ground state to the higher energy state, a measurement of this would confirm that the clock laser was on resonance with the clock transition. However, if the laser frequency drifted away from the centre of the transition we would observe a reduction in excitation probability, but we would not know in which direction to apply the laser frequency correction to bring it back on to resonance. If a π-pulse is applied when the laser frequency is half the transition linewidth ($\gamma/2$) away from the resonance centre, then there is only 50% excitation probability. But now, when the laser drifts from resonance we can use the change in excitation probability to determine the direction and magnitude of the frequency correction to be applied. The frequency distribution when a laser interrogates the clock transition is a Lorentzian function. It can be written as:

$$P = P_{max}\frac{\gamma^2}{\gamma^2 + 4\delta^2}, \tag{2.36}$$

where P is the excitation probability, γ is the linewidth of the clock transition and δ is the frequency detuning from the centre.

Laser frequency stabilisation to the clock transition is established by a series of frequency scanning across the atomic transition. At first, the laser frequency is set to -$\gamma/2$ so that the excitation probability is 0.5 and in the next step, it is set to +$\gamma/2$ which is above the centre frequency. The points a and a' in Figure 2.10 describe the situation. Even though the clock lasers are stabilised to ultra-stable references, there can still be mHz level drifts. Any drift in the laser frequency leads to a variation in the excitation probability. The conditions b and b' in Figure 2.10 refer to a laser drift situation. The variation shows whether the frequency is approaching or moving away from the centre. This frequency shift is monitored and fedback to the laser to correct the laser frequency in accordance with the atomic frequency. These steps are repeated to lock the laser frequency to the atomic line centre.

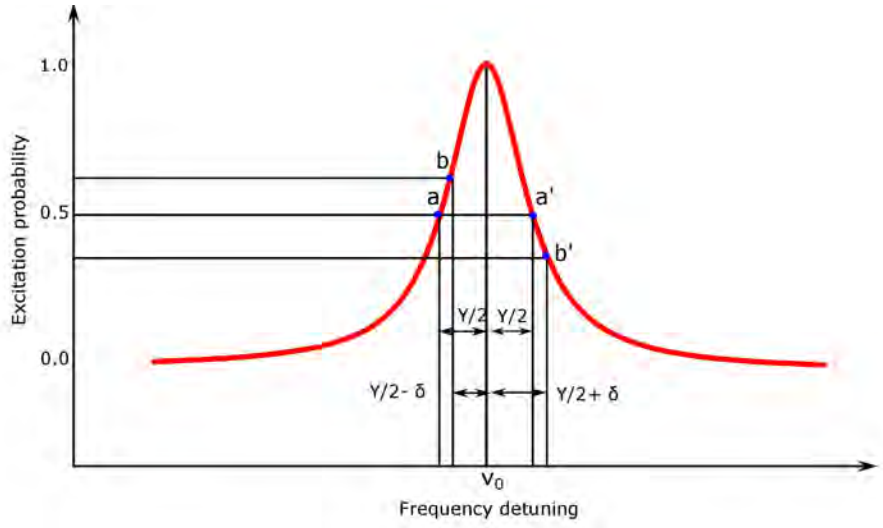

Figure 2.10: Illustration of locking a laser to the peak of the ultra-narrow clock transition. Laser frequency is scanned across the transition step by step in the directions above and below the centre of the transition. Any drift in laser causes a frequency detuning δ from the centre ν_0.

2.6 Stability and accuracy of a strontium optical lattice clock

As described in section 1.2, the stability and accuracy are the two factors that are essential in understanding the performance of a clock. The clock stability over a time period can be measured by detecting the noise of the clock and the accuracy can be determined by measuring the shifts that cause a deviation of the frequency from its true (unperturbed) value. Clock stability is measured by performing an Allan deviation measurement, where the frequency of the laser which is stabilised to the atomic transition is continuously logged for a long time using a frequency counter.

The fractional instability of an atomic clock is written as shown in equation 1.1. It can be re-written as [81]:

$$\sigma_y(\tau) = \frac{1}{\pi Q}\sqrt{\frac{T_c}{\tau}}\sqrt{\frac{1}{N} + \frac{1}{N n_{ph}} + \frac{2\sigma_N^2}{N^2} + \gamma}, \tag{2.37}$$

where T_c is the cycle time of the experiment, N is the number of atoms, n_{ph} is the number of photons detected for each atom, σ_N is the uncorrelated root mean square atom number fluctuation, and γ is the frequency noise of the probe laser. Each term under the second square root gives the signal to noise ratio for different types of noises. The first term is the quantum projection noise (QPN) which causes fundamental limits to instability of the atomic clocks by causing a population fluctuation in the system. QPN can be improved by spin squeezing of the atomic sample [82, 83]. Spin squeezed states can be created by means of atomic interactions. Squeezing the atomic pseudo-

spin via measurement of the atomic clock state populations suppresses quantum projection noise down to the Heisenberg limit that scales with $1/N$ where N is the number of atoms. The next noise term represents the photon shot noise. As a result of longer life time for the clock state ($^3P_0$) and stronger laser cooling transition at $^1S_0$ to $^1P_1$ from the ground level, shelving detection is possible. After the clock excitation between $^1S_0$ and $^3P_0$ states, the first stage cooling laser which is resonant with the transition $^1S_0$ to $^1P_1$ is used for fluorescence detection of the atoms in the ground state. Then the repumper laser is turned on to repump the atoms in the $^3P_0$ state back to ground state and again the $^1S_0$ to $^1P_1$ is probed with a resonant light. This process (shelving detection) is repeated to detected atoms in the clock state. As many atoms are collected, photon shot noise becomes lower than the quantum projection noise. The third term is the noise due to technical fluctuations in the atom number while interrogating the transition. This problem can be solved by measuring the atoms in both ground and excited states using shelving detection scheme, calculating the normalised fractional excitation against the number of atoms. The fourth (last) noise term is due to the frequency noise of the clock laser. During the clock measurement cycle (T_c), there are several milliseconds when the actual clock interrogation doesn't happen because of the time needed for atom preparation for clock interrogation. This is called the dead time and during this time, this clock interrogation laser frequency is not compared to atoms. This dead time causes degradation of the long term stability of the clock due to the down conversion of frequency noise of the clock laser at Fourier frequencies at the harmonics of $1/T_c$. This was proposed by Dick et al., and is known as Dick effect [82, 84, 85]. The Dick effect can be minimised by using a non-destructive read-out method. This leaves most of the atoms trapped in the lattice, thereby reducing the cycle time from 100s of milliseconds to 10s of milliseconds [86].

Accuracy is the measure of how strictly the measured clock laser frequency matches with the unperturbed transition frequency of the atom. There are several factors that affect the accuracy of an optical lattice clock. The most significant of which are the Stark shift and Zeeman shift on the atomic energy levels, cold collision shift, and quantum tunnelling effect.

As described in section 2.3.2, Stark shift occurs in the presence of a laser light. The electric field of the laser beam results in the splitting up of the energy levels of the neutral atom as the atom becomes polarised. By operating the optical lattice at magic wavelength one can eliminate the scalar Stark shift for clock state $^1S_0$ and $^3P_0$, see Figure 2.7. As this state has a zero total angular momentum, the vector light shift induced on these levels is zero.

While the first order Zeeman shift is absent in the bosonic isotope of strontium (^{88}Sr) due to the absence of nuclear spin, quadratic Zeeman shift is present in ^{88}Sr isotope due to the interaction of the energy levels $^3P_0$ and $^3P_1$ with the magnetic field required to induce the forbidden clock transition, see section 2.4.1 [87, 88]. The quadratic Zeeman shift has a magnitude typically around

$10^{-6}B^2\text{Hz}/\mu\text{T}^3$ [89]. The uncertainty in the shift, which is mainly caused due to the applied static magnetic field, is evaluated by varying the static magnetic field and observing the related atomic frequency shift. Therefore, the applied field has to be controlled to reduce the uncertainty. An uncertainty of 10^{-16} is reported in [90] for (^{88}Sr) which is obtained by calibrating the magnetic field better than 10 μT .

Black body radiation (BBR) which arises from the heat sources mounted near the atomic chamber can cause frequency shifts [91]. At room temperature, differential BBR shift of two atomic energy levels becomes the largest contributor to uncertainty budget in a clock transition. Hence it is required to characterise the effect of BBR shift on the transition frequency. Proper thermal stabilisation of the system can reduce the system uncertainty up to 1×10^{-18} [92]. There are experiments with cryogenic optical clocks which recently resulted in an accuracy of 2×10^{-18} over a 2 hours averaging time [44].

Another major cause of uncertainty is the collisional shift of atomic transition frequencies. Optical lattice clocks require a large ensemble of atoms to increase the signal to noise ratio; however, the atom density when large numbers of atoms occupy the same potential wells of the finite optical lattice will lead to atomic interactions leading to perturbation of the transition frequency. Bosonic isotope (^{88}Sr) allows multiple atoms having identical wave functions to occupy in the same quantum state which results in s-wave collisions [81] causing a shift in the energy levels in case of elastic collisions. Inelastic collision leads to density dependant broadening of the transition. The rate of loss of atoms in the optical lattice are higher for the excited state atoms due to their collision with ground state or other excited state atoms whereas the ground state atoms can collide only with excited state atoms which in turn leads to a different lifetime for the atoms in the excited and ground levels resulting in density dependant broadening of the transition [90, 93].

2.7 Reference cavities for frequency stabilisation

In an atomic clock, stable lasers play a vital role. Referencing to an atomic transition is possible only if there is a laser beam with a stable frequency and linewidth comparable to the atomic transition. The free running lasers are not good enough to probe narrow and ultra-narrow transitions due to their higher drift rates. Therefore, scientists started thinking of a way to reduce the frequency drift of laser sources by referencing them to stable or ultra-stable optical reference cavities. The idea is to transfer the length stability of the optical reference cavity to the frequency stability of the laser. Optical cavities are created when light propagates between two or more mirrors, separated by spacers. It allows light to circulate in a closed path, and confines and stores light at certain resonance frequencies. There are stable and unstable resonators depending on the

transverse beam offsets. The criteria for determining whether a cavity is stable or unstable is known as the cavity stability criteria. See section 4.1.1 for details.

The simplest case of an optical resonator is a linear cavity formed of two planar mirrors. It is also known as a planar Fabry-Perot (FP) cavity. When a light beam with amplitude E is incident on the first mirror (input coupler mirror), part of the beam is reflected by the mirror and part is transmitted. Here, it is assumed that the reflection occurs at the mirror surface which faces towards the inner side of the cavity where the medium is a high refractive index one compared to air, and hence a phase shift of π is suffered by the reflected beam. This phase shift occurs when the beam travels from a lower refractive index to higher refractive index medium. The amplitude of the transmitted beam (E_T) is the superposition of the directly transmitted part of the beam and the beams that couple out after multiply circulating inside the resonator. It is written as [94]:

$$E_T = Et_1t_2e^{-i\omega L/c}\left[1 + r_1r_2e^{-i\omega 2L/c} + r_1^2r_2^2e^{-i\omega 4L/c} + ..\right], \tag{2.38}$$

where E is the amplitude of the incoming beam, t_1 (r_1) and t_2 (r_2) are the transmission (reflection) coefficients of the first mirror and the second mirror, respectively, and $2\omega L/c$ is the phase shift. The phase factor, $\exp i(\omega t - \vec{k}.\vec{r})$ is choosen as unity at the surface of the first coupling mirror and it acquires a phase factor $\exp(-i\vec{k}.\vec{r}) = \exp(-i2\omega L/c)$ during each round-trip within the resonator.

Optical cavities with plane mirrors have larger diffraction losses and generally, curved mirrors or combination of curved and planar mirrors are used for resonators requiring high finesse. In Chapter 4, a FP cavity configured using a concave and plane mirror is discussed.

2.7.1 Laser frequency stabilisation

The most widely used technique to lock a laser to the cavity is the Pound-Drever-Hall technique [95]. Here, a frequency modulated laser beam is coupled into a reference cavity, the reflected beam from the cavity is collected using a photodetector (PD) and sent to a mixer used to demodulate the signal by comparison to the modulation signal. The demodulated beam is sent to the PID (proportional-integral-differential servo) controller which gives a feedback to the laser controllers to correct for any change in frequency [95, 96]. A dual sideband modulation scheme [97] can be used to offset the laser lock frequency up to several GHz from the cavity mode frequency depending on the free spectral range of the cavity. This technique has the advantage of obtaining larger tunability for the laser while in lock [98]. Further explanation of this technique and how to implement it is given in section 3.4.1.

There are several groups across the world who use cavities to narrow down the frequency of their lasers that are used for interrogating transitions in atomic clocks, atom interferometry etc. In 1997, S.Schiller and team have demonstrated the first mHz linewidth laser (0.7 Hz,

1064 nm) by locking to a cryogenically cooled sapphire optical cavity [99]. It resulted in a fractional frequency instability of 2.3×10^{-15} in 15 s. Later in 1999, sub-hertz frequency stabilisation of visible laser (0.6 Hz, 563 nm) is achieved by a group at NIST [100]. They used a high finesse ULE cavity under vacuum. Later, scientists start looking into the materials for cavity spacers and mirror substrates, as they play a major role in the stability of the cavity. The JILA group experimented with materials like ULE, Zerodur, and fused silica to understand the performance of each system [101]. It is important to mount the cavity wisely in a rigid housing. Viton balls or glass balls can be used to position the cavity within the housing. This ensures that the optical axis of the cavity remains unchanged. This also prevents any structural deformations occurring due to the bending of cavity material due to induced vibrations. J. Ye and team have performed simulations and experiments to test different mounting geometries for the cavity [102]. The Max-Planck institute in Germany also worked on laser frequency stabilisation to cavities with vertical orientation, achieving linewidth as narrow as 0.5 Hz [103]. NPL in the UK chose to stabilise their laser to a horizontally mounted cavity to get rid of the vertical low frequency fluctuations [104]. At PTB Germany, F. Riehle, J. Ye, and team have build a 210 mm long silicon cavity (spacer and mirror are silicon) to which a 1.5 μm laser is locked to a linewidth of 40 mHz. They have reported a short term stability of 1×10^{-16} [105].

In this chapter we have discussed the main components and concepts behind a strontium optical lattice clock. In the following chapters we will cover in detail the apparatus we have built for use in the miniclock and Space Optical lattice Clock (SOC2) projects. Chapter 3 covers the development and application of a second stage cooling laser at 689 nm for the miniclock apparatus. We also discuss the plans for optical trapping in this apparatus. Chapter 4 details the optical reference cavity built for the miniclock system. We also describe the development of a frequency stabilisation unit (FSU) using the optical reference cavity to lock multiple laser wavelengths required for strontium optical lattice clocks. Chapter 5 is about the progress and updates about the SOC2 apparatus. In chapter 6, we review the work covered, and look to the future.

Chapter 3

Development and application of lasers for strontium, with major emphasis to second stage cooling laser

As explained in chapter 2, the linewidth of the second stage cooling transition in strontium is 7.5 kHz at 689 nm, which is very narrow compared to the first stage cooling transition which has a 30.2 MHz linewidth. In order to cool and trap the atoms using this transition we need a laser that has a narrow linewidth and low drift rate. For this purpose, we have built a laser with tapered amplifier (TA) seeded by an external cavity diode laser (ECDL), which is also called a master oscillator power amplifier (MOPA). After stabilising the laser frequency to an external optical reference cavity, the laser is used to obtain a MOT of cold strontium atoms in a homebuilt vacuum chamber. Details of the laser design and development, and its application to cool atoms in an atomic chamber are described in this chapter.

3.1 External cavity diode lasers

External cavity diode lasers are the most widely used lasers in the field of cooling and trapping atoms due to their numerous advantages like low cost, tunability, compact size, and large availability at the required wavelengths. Laser diodes are commercially available. They can be bought and integrated in an extended cavity to build an ECDL. The laser diode is essentially a PIN diode with the active layer in the intrinsic region (I). Carriers pumped from the P (holes) and N (elec-

trons) regions are recombined in the I region to emit laser light. The energy bandgap between the conduction band (N) and the valence band (P) determines the wavelength of the emitted light. By tuning the temperature of the diode, the wavelength can be tuned precisely. The front facet of the laser diode usually acts as a low reflectivity mirror and hence, gives optical feedback. A small cavity length and low finesse due to the low reflectivity lead a laser to become unstable due to multi-mode operation and mode hopping (competition between different modes). This limitation paved the way for the development of extended cavity diode lasers. A longer cavity length improves the frequency stability of the laser according to equation 4.2 discussed in chapter 4. It has a longer damping time for the intra-cavity power which allows a lower phase noise and a narrower linewidth. External cavities are constructed using a collimating lens, and a diffractive grating to select the wavelength and feedback a single frequency to the laser gain medium. There are two different configurations for ECDLs: the Littrow configuration and the Littmann-Metcalf configuration [106], see Figure 3.1. In Littrow configuration, the first order beam is reflected back to the laser diode to provide the feedback. The zeroth order beam is reflected out of the extended cavity and is used in further experiments, e.g., for seeding the TA, and locking to a reference cavity. The feedback is optimised by tuning the grating. The only issue with this configuration is that, while tuning the grating, the direction of the output beam is also changed causing a misalignment in the whole laser system. The Littmann-Metcalf configuration has an additional reflector (mirror) which reflects the first order beam coming from the grating. Due to the dual pass of the first order beam through the grating, a narrower linewidth is obtained. However, the system gives low output power as the light is lost to the zeroth order diffraction during the second pass through the grating. Therefore, we have chosen the Littrow configuration for all our ECDLs.

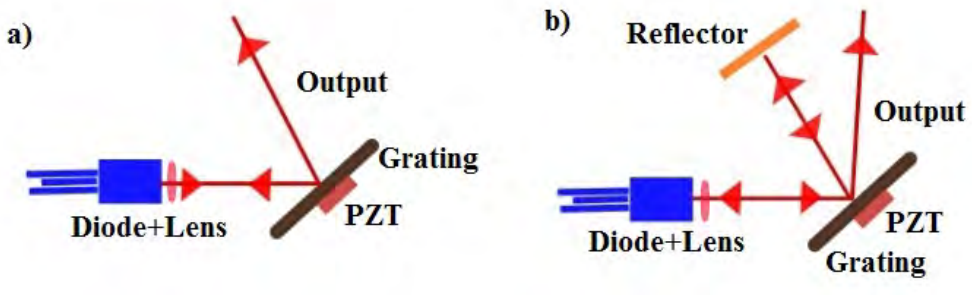

Figure 3.1: Figure a) shows the Littrow configuration and b) shows the Littman-Metcalf configuration.

3.2 Design of the MOPA for second stage cooling of ^{88}Sr

A master oscillator power amplifier (MOPA) is a laser configuration consisting of a master seed laser and a laser beam power amplifier. Fibre amplifiers [107] and semiconductor optical amplifiers (SOA) [108] are examples for power amplifiers. SOA can be used in different configurations to form a MOPA. The most common form of a MOPA is the tunable extended cavity diode laser and a tapered amplifier (TA) configuration. We choose an ECDL and TA design for the 689 nm laser rather than a master and slave set-up due to the high power. The quality of the TA output spatial mode can be improved by incorporating cylindrical lenses just after the TA output. It also maintains the narrow linewidth feature of the seed laser. In this setup, a grating-stabilised laser beam from an ECDL is used to seed the TA. An illustration of the MOPA is shown in Layout

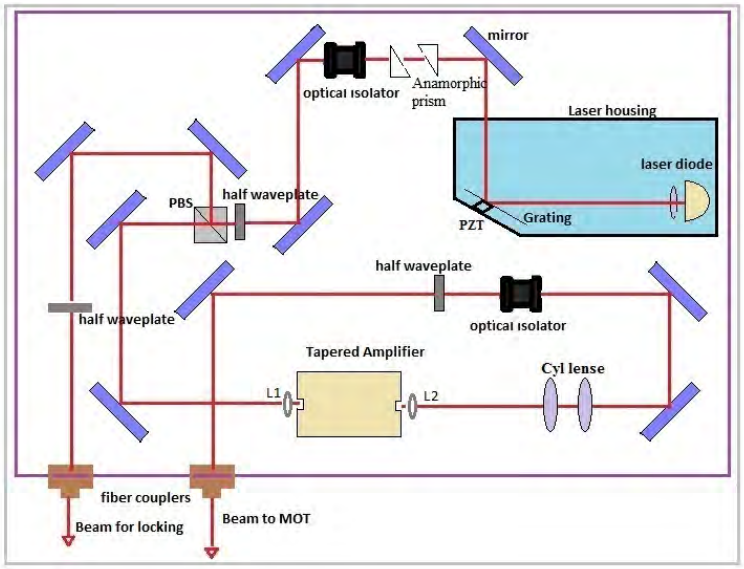

Figure 3.2: Layout of the second stage cooling laser at 689 nm for strontium. It's an ECDL seeded TA laser with fibre coupled outputs.

3.2. In this design a 689 nm laser diode, and a 1800 lines/mm diffraction grating form the extended cavity. The output of the diode is collimated using a 4 mm aspheric lens which is attached to an adjustable lens mount. A piezo actuator (PZT) is attached to the back facet of the grating. The diode, lens, grating, and PZT are housed in a 12 cm long housing. The extended cavity length, which is the distance between the diode and the grating, is 10 cm. The linewidth of the ECDL is inversely proportional to the square root of the cavity length [106]; however, a larger cavity length leads to issues such as vibration induced frequency variations. The ECDL housing is temperature stabilised using a peltier element (TEC) and a 10 kΩ thermistor. Temperature and current determine the lasing gain profile of the diode. By tuning the temperature, the diode cavity expands

or contracts leading to a change in the wavelength of the gain profile of the diode [109]. The profile is spectrally quite broad and has many competing lasing modes. So the diffraction grating is used to selectively reflect one of these modes back to the laser, resulting in amplification and lasing of this mode. The frequency of this mode can then be adjusted by changing the diffraction grating angle and cavity length. After providing feedback to the laser diode by tuning the grating, the laser achieves an output power of 28 mW at 160 mA current. An anamorphic prism pair is used to shape the beam coming out of the ECDL. An optical isolator placed after the ECDL prevents any back-reflected beam from going back to the diode. The total laser power is split into two parts using a polarising beam splitter (PBS) and half wave plate: 7 mW are sent to the reference cavity through an EOM and 17 mW are directed to the TA as seed input.

3.2.1 Seeding a tapered amplifier

The diode seeded semiconductor optical amplifier that is being used in the laser system is commercially bought (Eagleyard Photonics, Germany). The amplifier has a small index guided section with an aperture of 3 μm for the propagation of a beam, and a tapered gain guided region with a wider aperture of 70 μm to amplify the output power. The output of TA is diverging, asymmetric, and astigmatic. The beam divergence in the horizontal and vertical direction are 14° and 28°, respectively. The TA amplifies the input power by maintaining the same energy density as prior to the amplification. The amplifier has a groove on its entrance region which deflects the higher order modes to prevent heating up of the TA chip. A minimum of 10 mW laser power should be sent to the TA before it is turned on and it should not exceed the maximum power limit at which the TA saturates, which is 50 mW in our case. Any change in the power limits can likely cause damage to the TA due to thermal degradation. When the amplifier is optically seeded, electrical power in the amplifier is converted into optical power. If there is no sufficient seed power, this conversion will not occur. As a result, the electrical power is dissipated as heat energy causing thermal degradation of the TA. The TA is stabilised to room temperature using a peltier element and 10 kΩ thermistor. Home built current and temperature controllers are used to operate the TA. To allow a compact design of the electronics, the related drivers are built using a chip (ATLS200MA103-D) from Analog Technologies. The maximum current for the TA is 1.2 A.

Seeding the laser beam into the TA is a tedious task due to the large mismatch between the TA input aperture diameter and the laser beam diameter. An aspheric lens (L1) with a focal length of 6.24 mm is used to focus the beam onto the entrance facet of the TA. In order to mount the lens on the TA housing, the lens is fixed on a x-y-z translation stage (a manual translation stage is employed as the automatic one is not ideal for very precise adjustments of the position of the lens). An ammeter onto which the TA is connected reads the photocurrent corresponding to the laser

beam entering the TA. A power of 10 mW is used for seeding the TA during the alignment process. The lens position as well as the coupling mirrors are tuned to maximise the current on the ammeter. When a current of 2125 μA is reached, the lens is glued onto the TA housing using an epoxy and left overnight for curing. A collimating lens (L2) with 4.25 mm focal length is mounted after the TA. It collimates the beam in vertical direction. It is also fixed on a x-y-z translation stage and the output power is measured on a photodetector which is mounted after the lens. The lens position is optimised by increasing the detected output power before gluing. The output beam profile of the 689 nm TA system is astigmatic and diverging as shown in Figure 3.3. This characteristic leads to a loss of power after coupling the beam into an optical fibre. Therefore, the astigmatism is reduced by mounting two cylindrical lenses in the beam path after the TA, see Figure 3.2. The

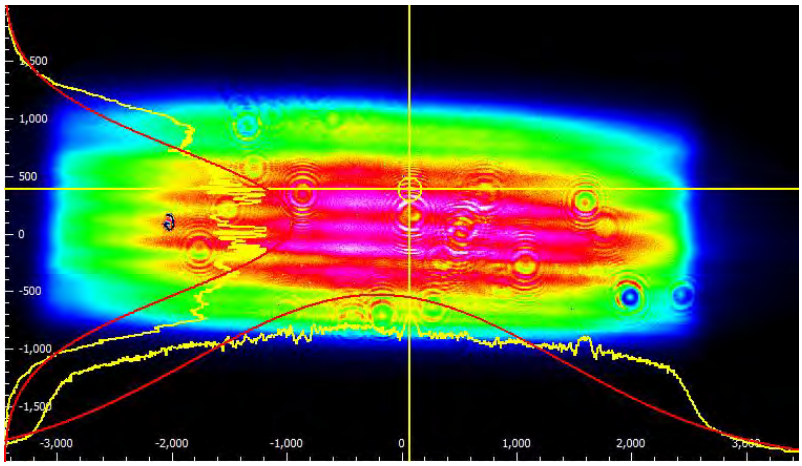

Figure 3.3: Beam profile of the 689 nm ECDL seeded TA output. The beam diameter of the X axis is 6457 μm, and that of Y axis is 2484 μm.

beam has a focal point in the horizontal direction after passing through the aspheric collimating lens. The two cylindrical lenses with focal lengths of 70 mm, and 50 mm collimate the beam in the horizontal, and vertical direction, respectively. The distance between the lenses is 18 mm. The lenses are mounted by identifying a position where the laser beam profile becomes circular. An optical isolator is mounted after the cylindrical lenses to avoid any back reflection falling onto the TA. The TA output is used for cooling and trapping strontium atoms.

3.3 Characterisation of the free running laser

The characterisation of the ECDL and the TA is carried out to evaluate the performance of the MOPA system. The lasing threshold of the ECDL is 70 mA with a maximum forward current of 160 mA. The MOPA gives a maximum output power of 330 mW when the TA drive current is 1 A and seed power 17 mW. The measured data is plotted in Figure 3.4. This measurement is

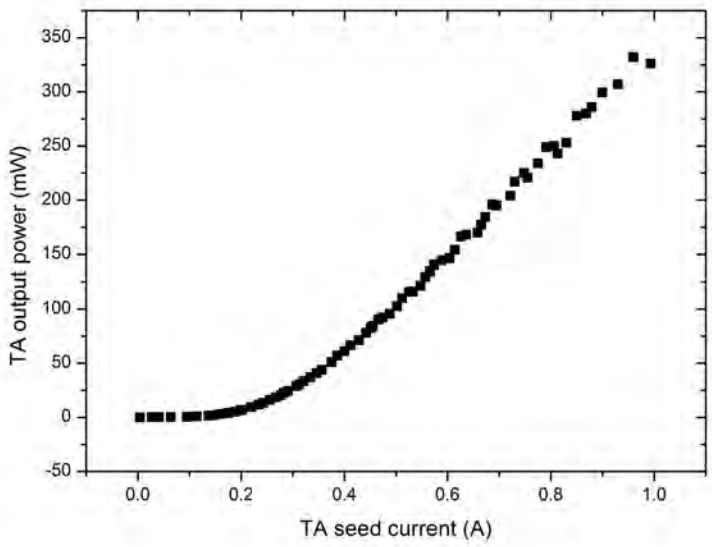

Figure 3.4: ECDL seeded TA output measured for a seed power of 17 mW at different TA drive currents.

taken directly after the collimation lens (L2) which is mounted after the TA, see Figure 3.2.

Figure 3.5 shows the output power of the TA after the optical fibre for a range of seed powers. Due to the non-optimised beam profile of the TA output, the coupling efficiency into the optical fibre is only 40-45%. This is better than the 25-35% coupling efficiency which is reported in [110]. Figure 3.6 shows the comparison between the TA output immediately after the TA and after the optical isolator at different seed powers with a forward TA current of 0.45 A. A linear fit to the TA output power indicates that the output varies linearly by 4.2 mW per mW of input power. The power after the isolator follows a linear change of 2.5 mW per mW of input power.

3.4 Stabilisation of the laser to a reference cavity

The second stage cooling laser requires a linewidth less than 7.5 kHz in order to be used for the cooling of strontium atoms. In order to narrow the laser linewidth from 700 kHz (free running laser linewidth) measured over 1 s to less than 7.5 kHz, and reduce the frequency drift we lock the laser to an optical reference cavity using the Pound-Drever-Hall (PDH) technique [95]. Since the frequency of the resonant mode of the cavity may not always be the same as that required for the cooling transition, we need to lock the laser with an offset frequency. To do this we use a dual sideband frequency modulation technique. The dual sideband lock scheme is chosen instead of a normal PDH locking technique due to the larger free spectral range (see section 4.5.3) of 5 GHz for

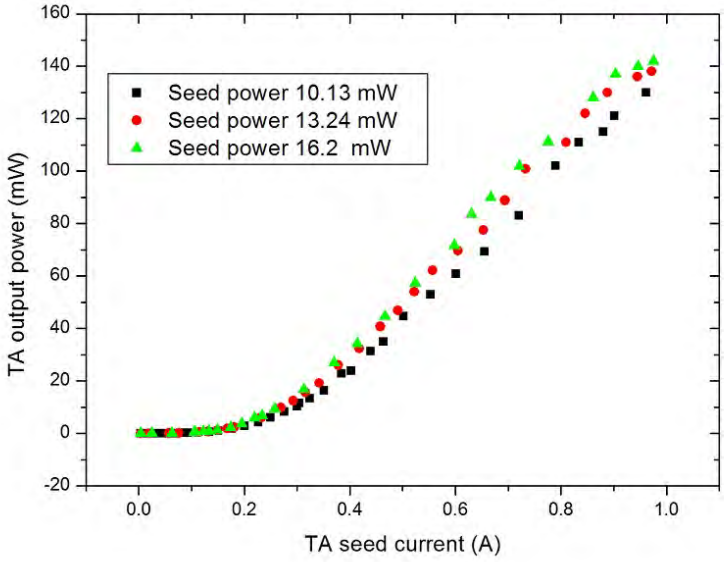

Figure 3.5: ECDL seeded TA output taken with different seed powers. Data are taken after coupling the beam into an optical fibre. An optical isolator is used between the TA output and optical fibre.

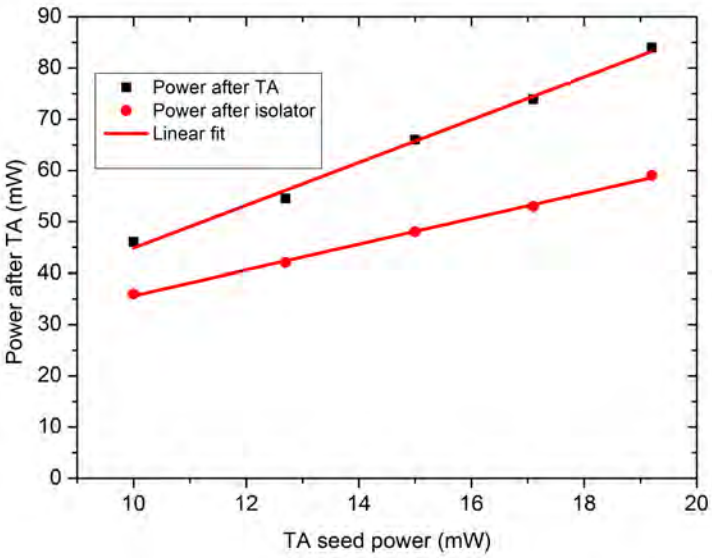

Figure 3.6: Output of the ECDL seeded TA measured at two points: a) immediately after the TA, b) immediately after the isolator. TA drive current during the measurement is 0.45 A.

the optical reference cavity. In other words, the TEM_{00} mode (transverse mode of electro-magnetic wave, see Figure 3.11) of the cavity occurs every 5 GHz. Therefore this mode is highly likely to have an offset between the required frequency and its resonance frequency. This gap is bridged using the dual sideband modulation technique [97]. The following subsections describe aspects of the locking set-up.

3.4.1 Dual sideband locking

In order to lock a laser to an optical cavity resonance, an error signal which is proportional to the frequency difference between the cavity resonance and the laser is required. The generation of such a signal is realised by applying the PDH locking method. This technique uses a phase modulation to stabilise the frequency of a laser with respect to an optical resonator. Here, the phase of the carrier beam with angular frequency of ω_c is modulated using an EOM with an angular frequency of ω_1. The electric field is given by,

$$E = \sqrt{P_0} \exp i(\omega_c t + \beta \sin(\omega_1 t)), \tag{3.1}$$

where P_0 is the input power to the EOM, and β is the modulation depth. The frequency modulation with the EOM generates two sidebands at the frequencies ω_c+ω_1 and ω_c-ω_1 along with the carrier frequency ω_c.

Dual sideband modulation is an extended scheme of the PDH method. It employs two modulation frequencies to generate sidebands. The advantage of this technique is that it provides a tunable frequency for laser locks. Here, the carrier beam can be modulated with two signals of angular frequencies ω_1 and ω_2, where $\omega_1 > \omega_2$, with respective modulation depths β_1 and β_2. This way the generated electric field is given by,

$$E = \sqrt{P_0} \exp i[\omega_c t + \beta_1 \sin(\omega_1 t) + \beta_2 \sin(\omega_2 t)]. \tag{3.2}$$

Expanding the equation using Bessel functions will result in a carrier with angular frequency ω_c, sidebands with angular frequencies ω_c+ω_1 and ω_c-ω_1 , and dual sidebands with frequencies ω_c+ω_1±ω_2 and ω_c-ω_1±ω_2 (see the cavity transmission in Figure 3.7). The error signal is generated by demodulating the reflected spectrum of one of these sidebands employing ω_2 as the demodulation frequency. The lock is performed on this dual sideband and the carrier frequency remains tunable within the free spectral range of the cavity. The tunability of the carrier band can be controlled by adjusting the frequency ω_1.

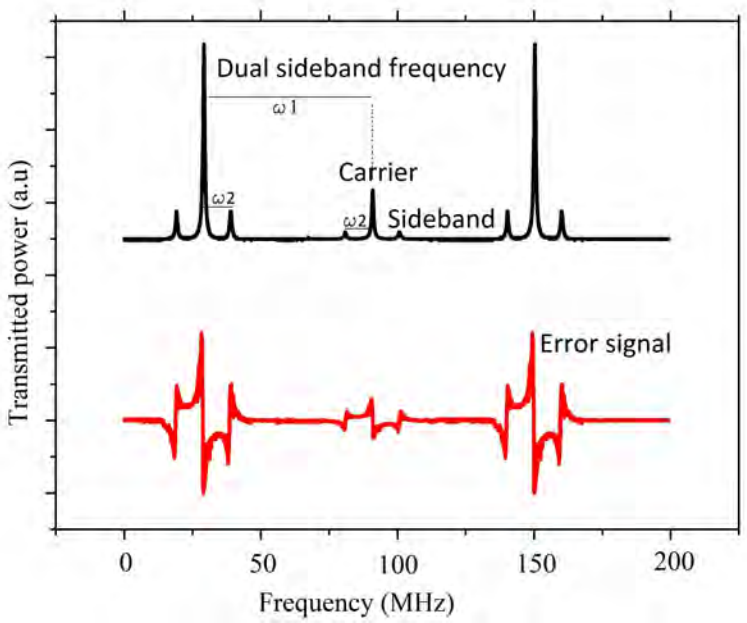

Figure 3.7: Error signal and the transmission signal obtained during the dual sideband modulation. The black trace shows the frequency modulated spectrum of the 689 nm laser. The red trace shows the error signal.

3.4.2 Laser locking set-up

Figure 3.8 describes the laser locking scheme for the 689 nm laser. One of the two outputs of the 689 nm laser is coupled to a fibre-coupled electro optic modulator (EOM) from Jenoptik. Details about EOM modulation can be found in [94]. The EOM is modulated with a ω_2=10 MHz radio frequency (RF) from a function generator. We use a direct digital synthesizer (DDS) to generate this RF signal.

A second modulation frequency ω_1, which is called the dual modulation frequency, is additionally applied to the EOM. The plot in Figure 3.7 shows the cavity transmission obtained by scanning the frequency of the laser across the resonance frequency of the optical reference cavity and error signal generated due to the dual sideband modulation method. The modulated output of the fibre EOM is connected to the beam collimator which contains a 4.5 mm lens. The beam is coupled into the cavity using two mirrors between the collimated laser output and the cavity. Information about the reference cavity is detailed in chapter 4. The polarising beam splitter cube and waveplate are for picking the light off, so that all the reflected signal goes to the photodetector (PDA10A). The photodetector output is connected to the phase detector along with the 10 MHz modulation frequency from the function generator. The phase detector demodulates the photodiode signal to create an error signal. The error signal goes to the locking electronics which includes a PID (Proportional-Integral-Derivative) controller (Fast Analog Linewidth Controller,

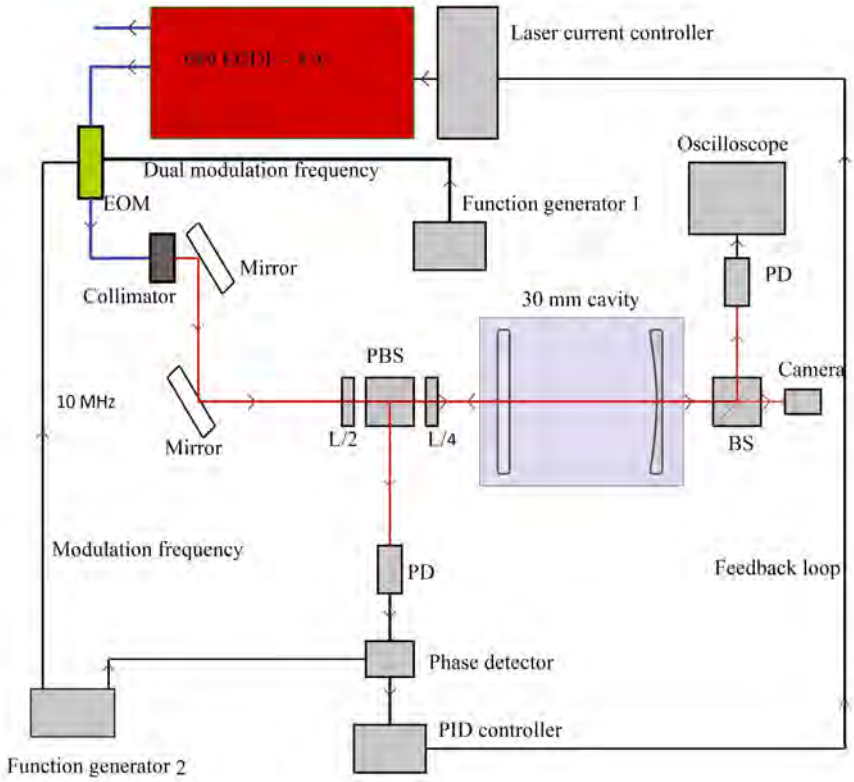

Figure 3.8: Schematic of a 689 nm laser frequency stabilisation unit using a dual sideband modulation technique. In this figure, red, black and blue lines indicate laser beam, electronic signal and optical fibre, respectively. Abbreviations used: PBS-polarising beam splitter, L/2-half wave plate, L/4-quarter wave plate, PD-photodetector and, PID-proportional integrational differential controller.

FALC) and a scan controller (SC 110), both from Toptica. The FALC and SC110 are connected internally. Therefore, the error signal is connected only to the FALC.

The output of the locking electronics is fedback to the laser current controller and the PZT driver. By adjusting the loop parameters (PID gains) the laser frequency is locked to the resonance frequency of the reference cavity. A suitable way to optimise the PID gains is to monitor the in-loop photodiode signal. A small amount of the signal (centred at the 10 MHz modulation frequency) is picked off using a directional coupler, and sent to a spectrum analyser. An example of this trace is shown in Figure 3.9. This servo signal consists of a centre peak and noise sidebands. For

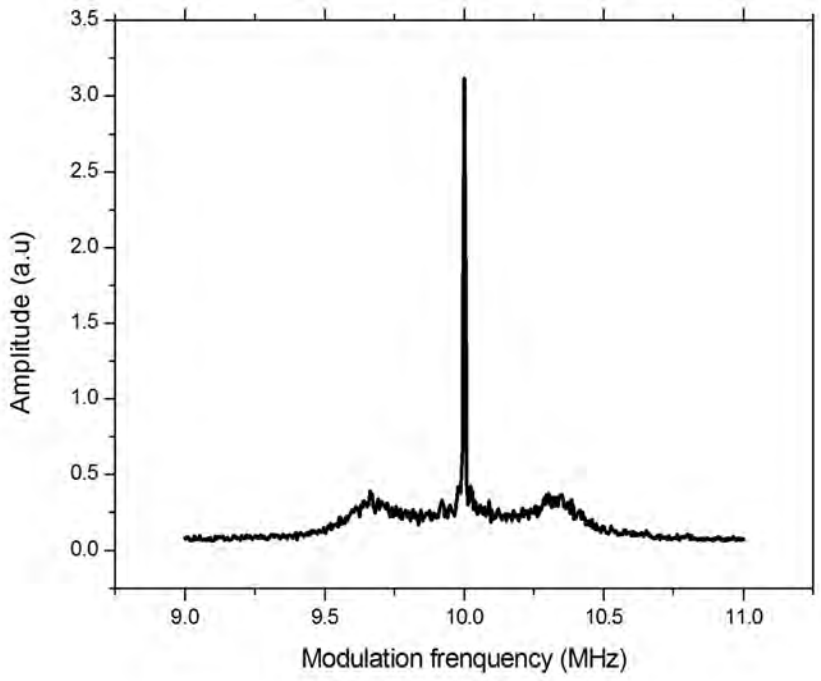

Figure 3.9: Servo bandwidth of the 689 nm laser when locked to the cavity. Modulation frequency for the laser is 10 MHz and the servo bandwidth is 0.35 MHz.

a good lock, the noise amplitude must be lowered and the bandwidth of the sidebands needs to be increased. These are achieved by changing the PID gains. When P gain increases, the noise amplitude increases and starts to oscillate. Then, reduce the gain slightly to find a spot where the laser is stable. The bandwidth of the noise sidebands is increased by changing the derivative (D) gain. It indicates the capability of the servo loop to adjust the changes due to any phase variation of the reflected laser beam coming out of the reference cavity. In Figure 3.9, the peak of the noise sidebands occur at 0.35 MHz. It is the lock servo bandwidth.

3.5 Coupling laser beam to the cavity

Beam alignment (coupling) into a reference cavity is the initial step when stabilising a laser frequency to a cavity mode. The laser beam has to be coupled with the TEM_{00} mode of the reference cavity [111]. Mode matching is the process of overlapping the waist of the laser beam with the waist of the cavity. Any change in beam waist and its overlap is likely to cause in-phase coupling with the higher order modes of the reference cavity. This problem can be solved by using a mode matching lens between the laser and the reference cavity [112].

The beam waist of the cavity w is calculated using ray transfer matrix (also known as ABCD matrix) as,

$$w = \sqrt{\frac{2|B|\lambda}{\pi\sqrt{4-(D+A)^2}}}, \tag{3.3}$$

where λ is the wavelength of the laser beam, and A, B and D are the parameters obtained from the ray transfer matrix [113], see section 4.1.1 for details on ABCD matrix. At 689 nm, the reference cavity has a beam waist of 127.1 μm. Figure 3.10 shows the cavity waist calculated for all the ^{88}Sr transition wavelengths. The mode matching for a single laser and cavity configuration can be easily

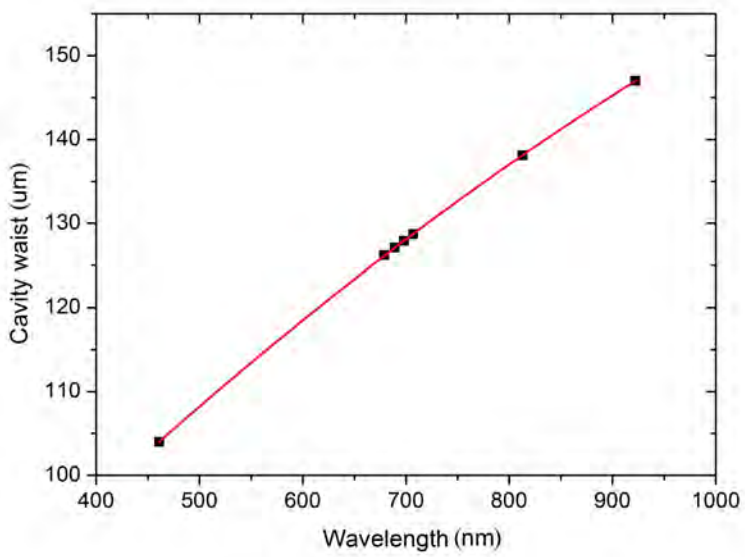

Figure 3.10: Graph showing the theoretical cavity waist at different laser wavelengths required for Sr optical clock. Scattered black data points are calculated and red line is a quadratic fit to the points. The cavity used has a length of 3 cm and approximately 10,000 finesse at 689 nm.

achieved in our system. The output of the EOM is connected to a Schäfter+Kirchhoff laser beam collimator. The 4.5 mm lens within the collimator is movable. By adjusting the position of the

lens, mode matching and thus the laser beam power transmitted through the cavity is improved, which is verified by visualising the photodetector output with an oscilloscope.

The alignment of the 689 nm laser beam to the reference cavity is achieved by monitoring the cavity modes on an imaging source camera connected to a computer. When the laser beam is on resonance with the cavity modes, it is captured by the camera as shown in Figure 3.11. By beam walking, tuning the laser frequency, and changing the scan amplitude, the alignment of the beam with the cavity is improved. When well aligned, and the laser is on resonance with the cavity, the TEM_{00} mode can be seen, as shown in Figure 3.11 (i).

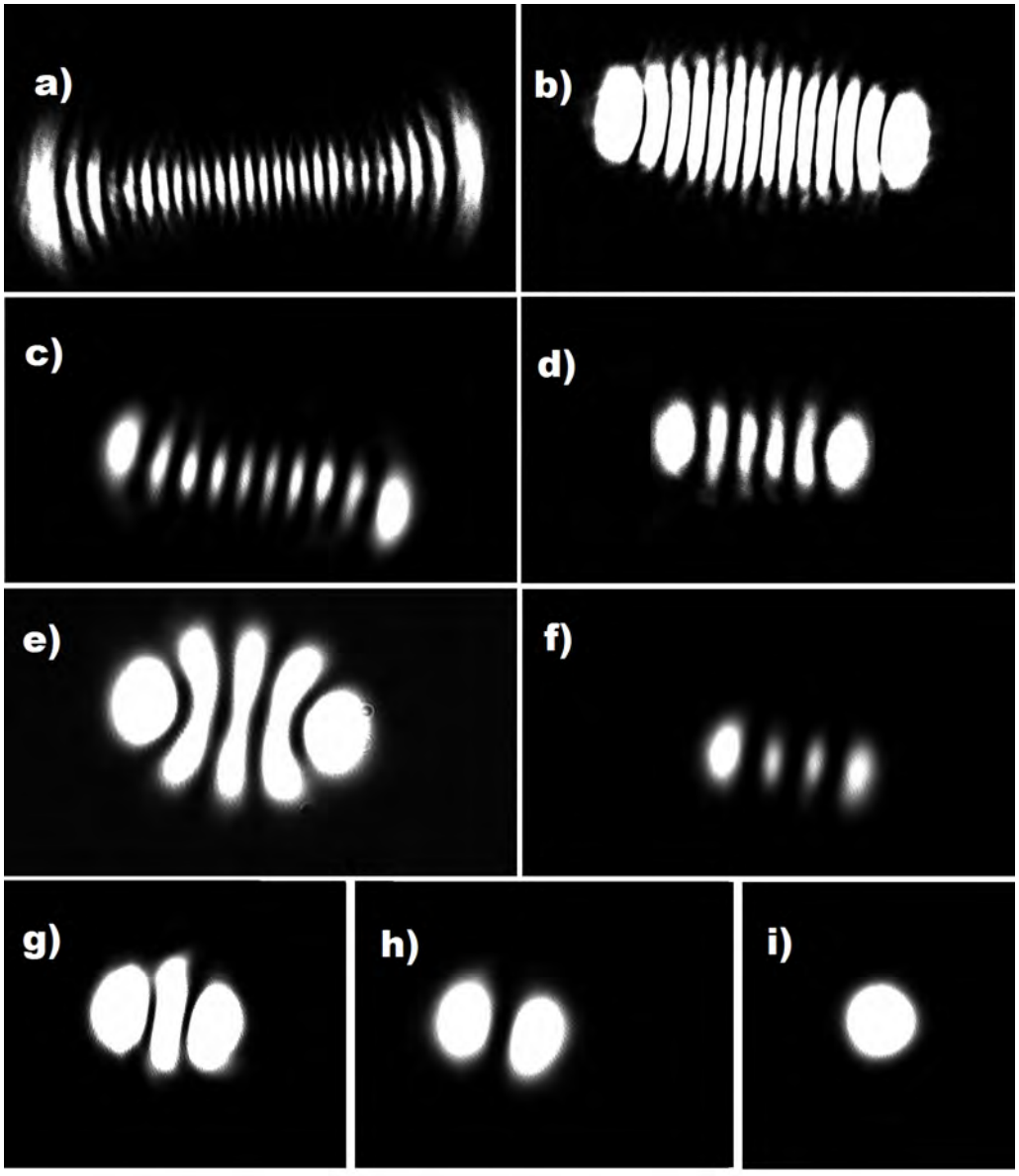

Figure 3.11: Various stages of the laser beam coupling with the cavity. Each figure represents a TEM mode. Part (i) displays the TEM_{00} mode. TEM_{00} mode is used for locking the lasers in this work.

3.6 Application of the laser in the miniclock chamber

The stabilised MOPA is used to realise a strontium MOT in the science chamber, which is otherwise referred to as miniclock chamber in our case. Before describing this process, we will introduce the design of the miniclock chamber which utilises a single-beam configuration to obtain cold atoms. It is important to consider a six-beam MOT and a three-beam MOT before narrowing down the set-up to a single-beam MOT. A six-beam MOT is the conventional MOT configuration that is widely used, the physics of which is described in section 2.2. The system that our lab had built several years ago consists of a 2D MOT pre-cooling chamber, differential pumping stage and 3D MOT chamber [4], see Figure 3.12. A dispenser powered by an electric current is used to emit hot

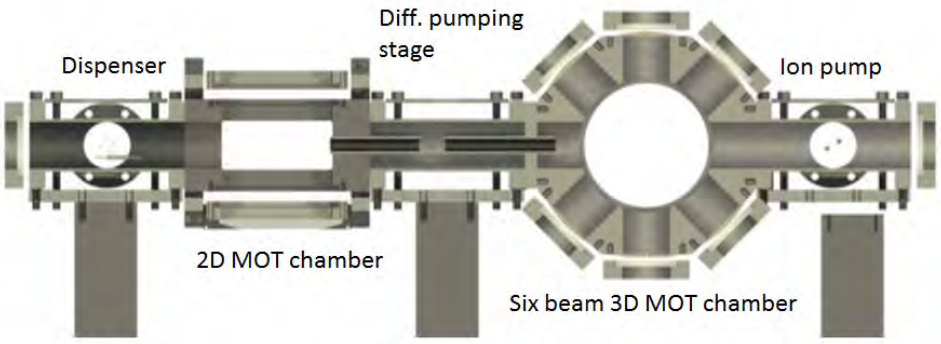

Figure 3.12: CAD drawing of the atomic chamber including a 2D MOT and a six-beam 3D MOT chamber. Image obtained from [4].

strontium atoms. The atoms reaching the 2D MOT chamber are pre-cooled by a 461 nm laser using the transition $5s^2\ {}^1S_0 \rightarrow\ 5s5p\ {}^1P_1$. Permanent magnets with adjustable spacing so as to nullify the magnetic field at the entrance to the 3D chamber are used. Almost 10^8 atoms/second reach the 3D MOT chamber from the 2D MOT chamber. The atoms are further cooled and trapped using a 461 nm laser and water-cooled anti-Helmholtz coils with a magnetic field gradient of 50 G/cm. In order to realise the six-beam MOT scheme, there are six inputs for the laser beam. Each beam is expanded using telescopes which determine the intensity of the beam at the centre of the MOT chamber (5 mW/cm^2 in this system). Since there are six different fibres mounted on opto-mechanics, the system is very sensitive to vibrations. This requires frequent realignment. Ole Kock's PhD thesis describes the layout of the atomics package in more detail [4]. The complexity of the six-beam MOT chamber led to the development of a three-beam MOT chamber which is more robust [114].

Optical fibres are connected to the three-beam MOT chamber using cage systems. Due to the

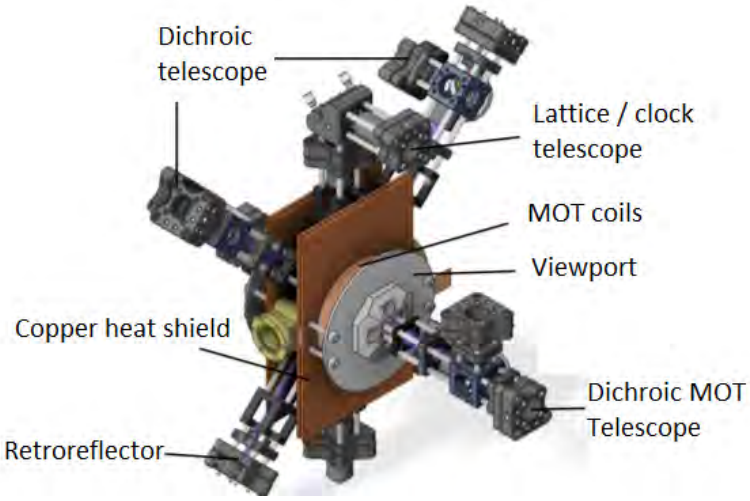

Figure 3.13: CAD drawing of the three beam MOT chamber. Image obtained from [114].

longer length of cage systems (10 cm), vibrations are highly likely to affect the system. There are three fibre inputs and opposite to each of the inputs are retro-reflective mirrors which reflect back the laser beams to make the remaining 3 beams, see Figures 3.13, 5.1. This way, the three-beam MOT achieves similar effect as six-beam MOT, but requires a lower number of fibres and opto-mechanics which reduces complexity and regular maintenance of the system. Moreover, this set-up has only a 3D chamber where the cooling is performed and no requirement for a 2D MOT. The atomic flux coming out of the dispenser is slowed down using a Zeeman slower made of a series of permanent neodymium magnets [115]. Refer to Lyndsie Smith's PhD thesis for more information regarding the layout of the compact atomics package [114]. A further reduction of the number of beams is achieved in the next generation of the chamber design. The latest design, which is described as 'miniclock chamber', has a single beam to realise MOT [116], see Figures 3.14, 3.15.

3.6.1 Overview of the single-beam MOT chamber

The single-beam MOT chamber [117] is designed to allow the construction of a miniaturised clock chamber system. Such a system has all the properties of the other chambers, which includes a first stage cooling, second stage cooling, lattice trap, and clock interrogation stage. However, the system is very compact. Major efforts are taken to reduce the dimensions of the vacuum chamber, lasers, and electronics size to realise a compact and robust system. The scheme uses four right angled silver coated prism mirrors. The mirrors are fixed inside the chamber, as shown in Figure 3.15. These mirrors create two pairs of MOT beams by reflecting the incoming beam. The square space in the centre acts as the path for the third MOT beam pair; there is an external mirror

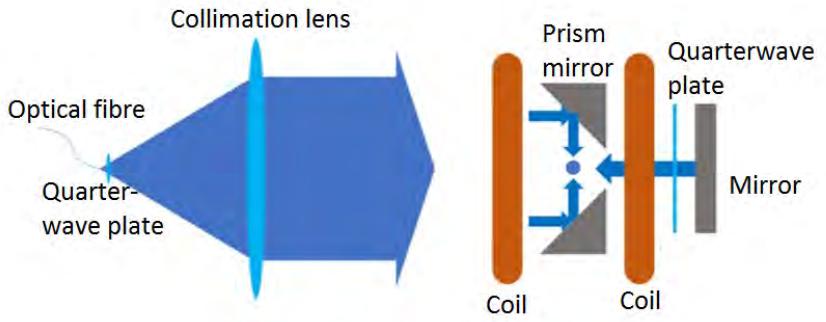

Figure 3.14: CAD drawing of the single beam MOT. Image obtained from [116].

mounted at the back side of the chamber to create the retro-reflection beam for the third MOT beam pair. The space between the mirrors is used to send the atoms into the chamber as well as for camera detection to monitor the MOT. The two vertical spaces are for aligning the clock laser and lattice laser onto the cold atoms.

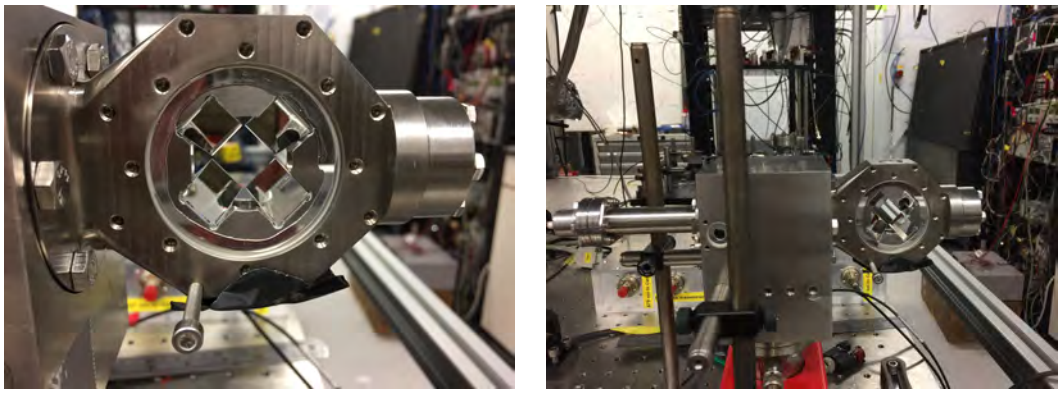

Figure 3.15: Single beam MOT chamber. Left: Mirrors embedded inside the vacuum chamber. Right: Vacuum chamber mounted on an optical table.

Anti-Helmholtz coils are attached to the front and rear facet of the chamber. A hybrid getter ion pump (SAES) is used to maintain the vacuum level of 1.9×10^{-11} mbar in the chamber (pressure level measured when the dispenser was off). Laser beam is sent to the chamber through a beam expansion telescope which is attached to the chamber. The telescope expands and collimates the beam exiting the fibre before entering the MOT chamber. A quarter wave plate used in the telescope cage system creates a circularly polarised beam. A mask which has square openings in

the sides and one square opening in the centre with dimensions similar to the prism mirrors is used to reduce the stray (scattered) light that causes a background noise on the detectors. The mask also carries a neutral density filter to balance the intensity between the central beam and the side beams.

A blue MOT is obtained in the system using a frequency doubled Titanium Sapphire (Ti:Sa) laser (from M Squared Lasers) at 461 nm. A 2.0×10^{-9} mbar vacuum, 4.5 A dispenser current, and 35 G/cm magnetic field gradient is used to obtain the MOT. Repumper lasers are employed to increase the number of trapped atoms. The power in the laser beams are 100 mW, 5 mW, and 5 mW for the 461 nm , 707 nm, and 679 nm lasers, respectively. Out of 100 mW power in 461 nm only 48 mW of light is incident on the atoms, due to the beam geometry and the use of mask. The temperature of the blue MOT atoms is in the range of 3 mK. More details of the vacuum chamber, system assembly, and blue MOT characterisation is available in Wei He's PhD thesis [116].

3.6.2 Broadband red MOT

The main application of the 689 nm MOPA system that we have built is in the cooling and trapping of strontium atoms. We have utilised the MOPA to realise the very first broadband red MOT in the miniclock chamber. The 689 nm laser beam is used to cool the strontium by driving the $5s^2\ {}^1S_0 \rightarrow 5s5p\ {}^3P_1$ transition with a linewidth of 7.5 kHz. With this transition, the atoms can be cooled down to μK level temperatures. One of the two outputs of the laser is sent to the reference cavity and locked to the cavity resonance. The cavity locked linewidth of the laser during the second stage cooling experiment is 99 kHz measured over 1 s (see section 4.8 for linewidth measurement details). The second output, which is the TA output, is coupled into the fibre to which the 461 nm laser beam is already coupled, and sent to the MOT chamber through the beam expansion telescope. As the optical fibre is not equally usable for the 461 nm and 689 nm beams, the coupling efficiency is compromised. Only 13 mW of 689 nm light is obtained out of the fibre after coupling 70 mW input power. In order to obtain a broadband red MOT, the frequency of the laser has to be broadened. Once atoms are trapped in the broadband MOT, the frequency broadening can be reduced and narrowed down to obtain the narrowband red MOT. Further cooling occurs in the narrowband MOT as all the hot atoms in the broadband MOT are blown away.

An acousto optic modulator (AOM) is used for the frequency broadening of the 689 nm laser in order to create frequency broadening needed for the broadband MOT. Before coupling the laser into the MOT fibre, the laser is sent through a single pass AOM operating at 80 MHz. Frequency broadening is obtained by modulating the AOM drive frequency at 14 kHz, with a modulation depth of 1.2 MHz. A function generator (SFG-2010) is used to supply the 14 kHz modulation frequency to the AOM. The function generator output is amplified using an RF amplifier prior to

sending to the AOM. The modulated output frequency spectrum is shown in Figure 3.16. It is the AOM drive signal. When a laser beam propagates through the AOM with a modulated frequency, the laser power is distributed within the spectrum. After broadening, we scan the laser frequency across the atomic resonance frequency in order to find the red MOT.

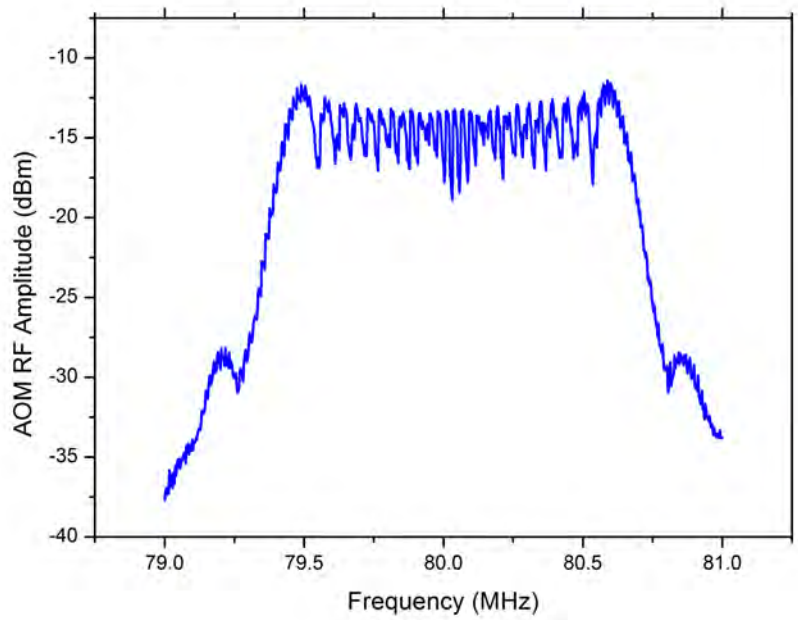

Figure 3.16: Modulated AOM frequency signal applied to the 689 nm laser to obtain the broadband red MOT.

We use a computer programmable field-programmable gate array (FPGA) to control the loading of atoms into the red MOT. Ideally the repumper lasers at 679 nm and 707 nm would remain switched on at all times. In our case, we used only the 707 nm repumper for the results presented here because the 679 nm repumper was not operational (use of both repumpers will increase the number of trapped atoms). The first stage cooling uses 461 nm laser beam with 48 mW of power hitting the atoms. The anti-Helmholtz magnetic field generation coils take 2.5 A current to generate a field gradient of 35 G/cm. About 500,000 atoms are trapped in the blue MOT. After 210 ms, the blue laser power and magnetic field gradient are ramped down to zero and 7 G/cm, respectively over a time period of 50 ms. The 689 nm second stage cooling laser is switched on all the time. Even though 13 mW of 689 nm light comes out of the fibre, only 4 mW is hitting the atoms. This is due to the use of a mask and neutral density filter. After 60 ms of cooling in the broadband red MOT, the blue laser is turned back on for 5 ms to detect the atoms in the red MOT via fluorescence imaging on a CCD camera. A 2 mm diameter MOT is obtained with this process. About 5% of atoms are transferred from the blue MOT to the broadband red MOT

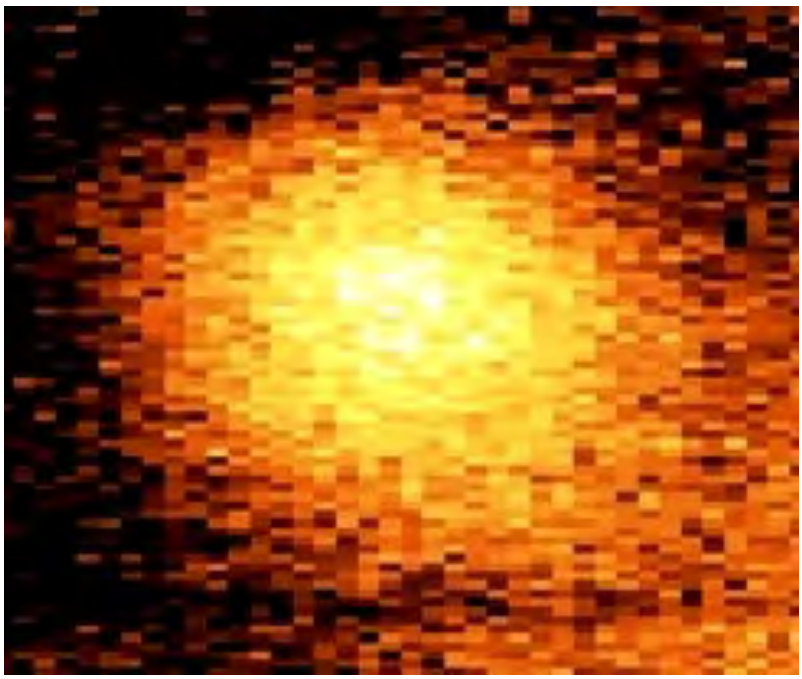

Figure 3.17: Image of the red MOT obtained using the MOPA laser system. It contains 25,000 atoms.

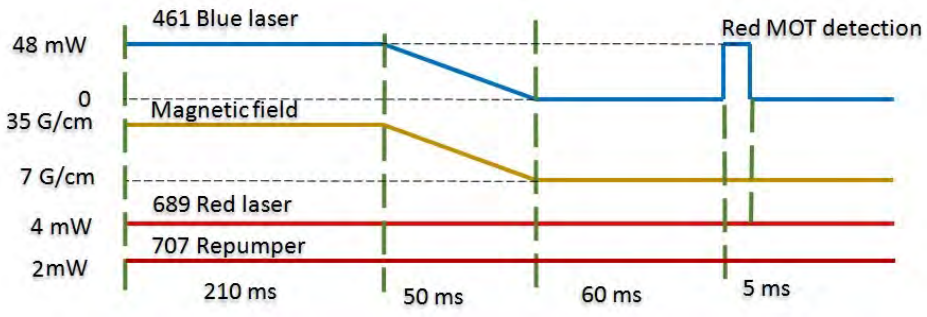

Figure 3.18: Cooling sequence to obtain a red MOT in the miniclock vacuum chamber.

shown in Figure 3.17. The cooling sequence is illustrated in Figure 3.18.

We are yet (as of the time of writing this report) to characterise the red broadband MOT and demonstrate transfer of atoms from the broadband MOT to the narrowband MOT, because the drift of our reference cavity is too high and the laser moves away from the atomic resonance too quickly, see section 4.8. Also, as part of a collaborative project, the device needs to be moved to another Institute (NPL, U.K). In the future we plan to rectify this by building a higher stability cavity, see section 4.12, which is expected to have a drift rate on the order of <1 kHz per hour. This solution requires the design and construction of a new reference cavity which will take several months, so in the shorter term we have considered but not implemented a range of interim solutions such as phase locking of the laser system to a very stable reference laser, or locking the laser to a frequency comb which itself is locked to a clock laser referenced to an ultra-stable ULE (ultra-low expansion glass) cavity.

3.7 Proposed lattice configuration

The third stage of the strontium optical lattice clock is to trap the cold atoms in a 1D optical lattice. This trapping is performed once atoms are captured in the red MOT. A lattice is formed by the interference developed in the centre of the vacuum chamber by transmitting and retro-reflecting the lattice laser beam. For strontium atoms, we use a laser with a wavelength of 813 nm to realise the lattice trap. The initial lattice optics characterisation is performed by using the M Squared Ti:Sa laser system. The optics for the lattice are mounted on a portable breadboard. It can be attached to the vacuum chamber in a vertical orientation. For testing purposes, the optics are assembled away from the vacuum chamber. The scheme is shown in Figure 3.19. Fibre collimator, two aspheric lenses, and retro-reflection mirror are mounted on a portable breadboard with dimension of 27 cm $\times$ 7 cm $\times$ 1.2 cm. After optimising the lattice optics, it is mounted vertically around the chamber such that the chamber is located between the two aspheric lenses. The centre of the chamber should be positioned at the beam waist of the lattice configuration. A photograph taken after mounting the portable lattice optics around the vacuum chamber system is shown in Figure 3.20.

The beam of the lattice laser is coupled into a high power optical fibre (PMJ-A3 HPCA3HPC-780-5/125-5AS-5-1-AR2, OZ Optics) with a mode field diameter of 4.9 μm. The output end of the fibre is connected to a fibre collimator which contains a lens with a focal length of f_c=4.5 mm. The beam exiting the collimator is collimated by observing the beam over a long distance. After the collimator, two aspheric lenses (ASL10142-B, Thorlabs) with focal length f=79 mm each are mounted. The beam waist of the laser at the focus is calculated in order to compare it with the

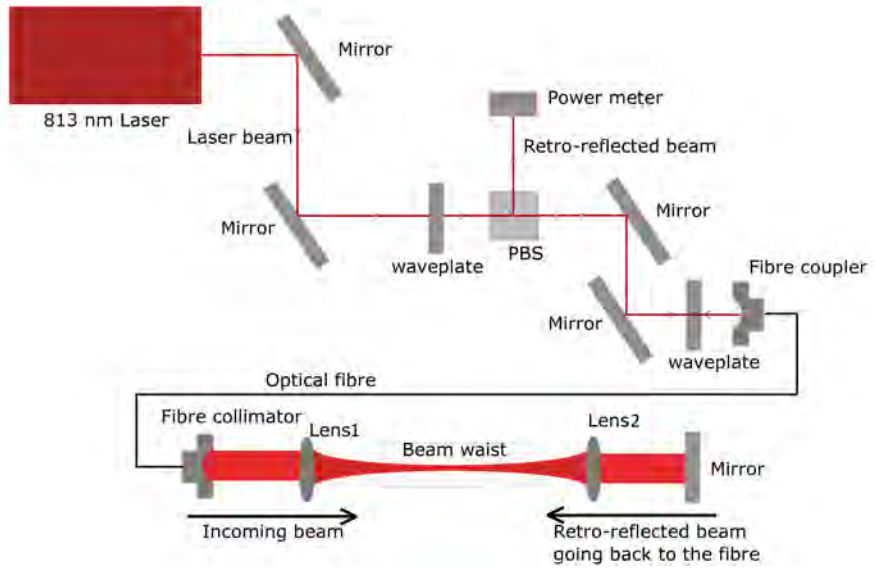

Figure 3.19: Scheme of the optical lattice configuration for the miniclock vacuum chamber. The dotted rectangular region indicates the location of vacuum chamber.

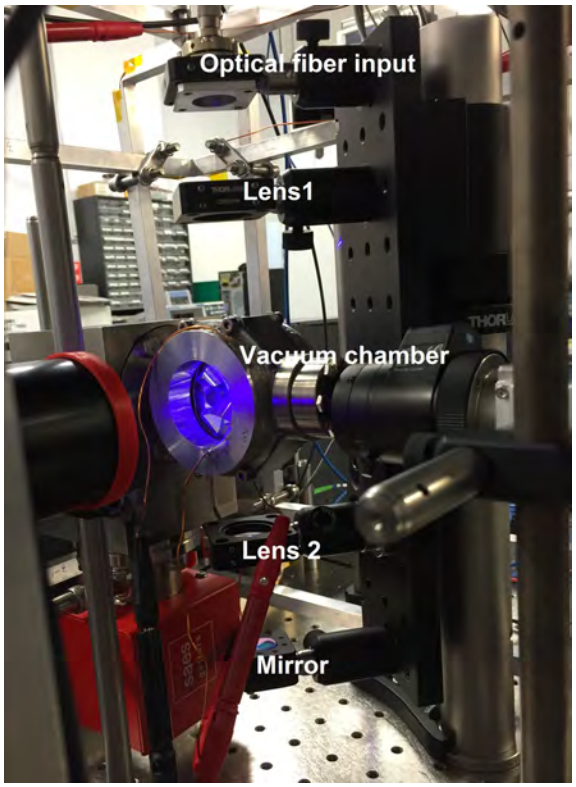

Figure 3.20: Lattice optics mounted on a portable breadboard and aligned on to the vacuum chamber.

clock laser beam waist in the later stage of the experiments (see section 5.3.4 to read about the relevance of clock and lattice laser beam waist measurements). The calculation is as follows:

$$w = \frac{\lambda f}{\pi \omega_c}, \tag{3.4}$$

where λ is the wavelength of the lattice laser and

$$w_c = \frac{NA \times f_c}{F_{NA}}, \tag{3.5}$$

where w is the beam waist (radius) due to the lens in the fibre collimator. NA is the numerical aperture of the optical fibre, and F_{NA} (0.66 at 3% level) is the factor to correct for various definitions of the NA. The calculations result in a beam waist radius of 49.9 μm at the focus.

The profile of the laser beam after the first lens (Lens1) is measured to experimentally understand the beam waist position. The beam waist is 48.74 μm measured at 7.9 cm from the Lens1. The data is plotted in Figure 3.21. A retro-reflection mirror is mounted after the second lens (Lens2). The laser beam hitting the mirror is retro-reflected at 180° to the optical fibre and good overlap is ensured by coupling the beam back down the optical fibre. The retro-reflected beam power is measured using a power meter placed after a PBS mounted before the input end of the fibre, see Figure 3.19. In order to increase the overlap between the incoming and the retro-reflected beam, the retro-reflection mirror and the distance between the lenses are adjusted to increase the power detected by the power meter. 63% of the incoming power is retro-reflected back into the fibre. The distance between the lenses is 15.8 cm in the final set-up. The expected trap depth at a beam waist of 48.74 μm is 37.3 μK when an input power of 500 mW is used.

3.8 Repumper lasers for the strontium clock

A repumper laser is not essential in Sr (like it is in Rb and Cs), because the $5s^2\ {}^1S_0$ to $5s5p\ {}^1P_1$ transition is almost closed (there is only a 1 in 50,000 decay to the $5s5p\ {}^3P_2$ state), and the $5s^2\ {}^1S_0$ to $5s5p\ {}^3P_1$ transition is fully closed, see Figure 2.1. While cooling on the $5s^2\ {}^1S_0$ to $5s5p\ {}^1P_1$ transition repumper lasers will aid the cooling process by effectively closing the cooling cycle so that no atoms are lost, and they can increase the number of atoms in the blue MOT by up to an order of magnitude. The repumping stage includes two intermediate states. Atoms are pumped from $5s5p\ {}^3P_2$ to $5s6s\ {}^3S_1$ using a 707.202 nm repumper laser. From $5s6s\ {}^3S_1$, atoms decay to $5s5p\ {}^3P_{2,1,0}$ states. Atoms in the $5s5p\ {}^3P_1$ state which has a lifetime of 21 μs decay to the ground state $5s^2\ {}^1S_0$. Atoms in the $5s5p\ {}^3P_0$ state are repumped to $5s6s\ {}^3S_1$ state using 679.289 nm repumper laser.

We have designed a laser module which includes two Littrow ECDLs as illustrated in Figure 3.22. One is for the 707 nm and the other is for the 679 nm repumper laser. Both the diodes

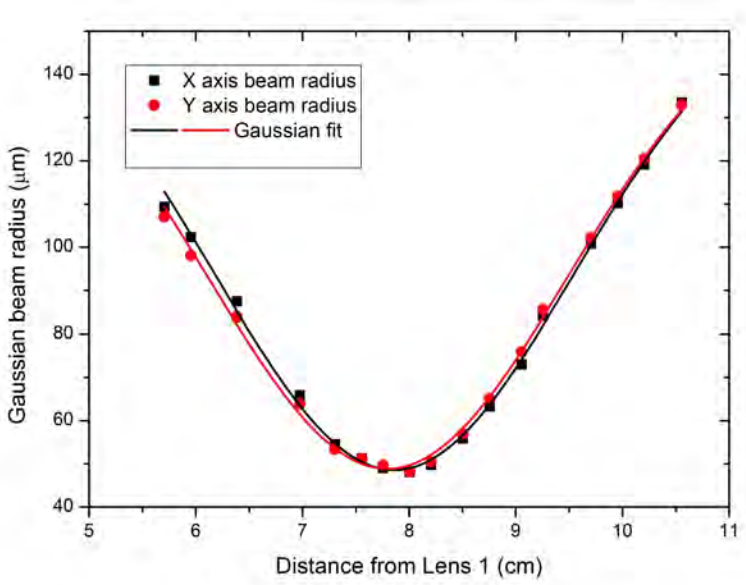

Figure 3.21: Beam profile of the lattice laser measured after the first aspheric lens. The beam waist radius is 48.7 μm.

are anti-reflection (AR) coated. AR coating on the diodes helps to avoid mode hopping and it increases the mode-hop free tuning range from a few MHz to several GHz. The diode outputs are collimated using mounted aspheric lens with focal length 2.75 mm. The collimated diode output is incident upon a PZT controlled diffraction grating with 1800 lines/mm. The diodes are mounted on temperature stabilised mounts which also holds a the collimation lens (see section 3.2 for more details on ECDL design). The ECDLs are shielded using two separate aluminium housings for an appropriate control of temperature and air fluctuations. After each ECDL, an optical isolator provides 35 dB of isolation. The laser beams passing through their respective isolators are split into three different parts using the PBS and half wave plates.

Both lasers have three outputs each. One for locking the laser to a reference cavity, the second for monitoring the wavelength, and the third output for creating MOT in the chamber. The beams to the chamber are combined inside the laser system using a PBS and sent through a single fibre to the MOT chamber. Therefore, the laser system is fitted with five output ports. In the 707 nm laser, out of the 28 mW of laser power measured after the diffraction grating, 9.7 mW, 1.0 mW, and 10.4 mW of power are going to the cavity, wavemeter, and chamber ports, respectively. Measurements are performed at 81 mA of diode drive current. A coupling efficiency of 50% is obtained in each fibre for both lasers. For the 679 nm laser, at 77.7 mA diode drive current, 27-28 mW of power is measured after the diffraction grating and the beam power is split similar to the 707 nm laser. Hence, both the 679 nm and 707 nm laser provide a similar amount of laser power for locking and repumping. These lasers can be locked to the 30 mm optical reference cavity

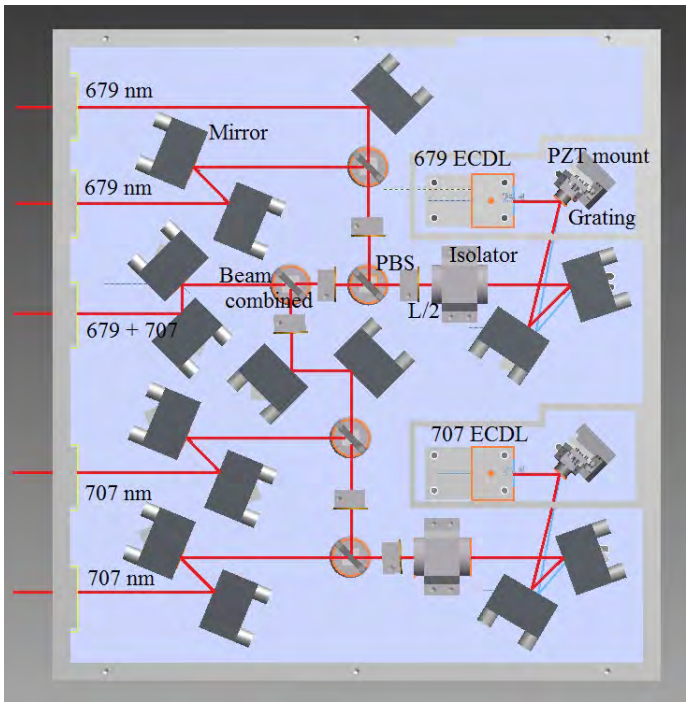

Figure 3.22: CAD design of the portable repumper laser module.

described in section 4.7.

In this chapter we have discussed the details of the MOPA system and its application in obtaining the very first broadband red MOT in the miniclock chamber. We have also discussed the results obtained from characterisation of the MOPA system. Now we are in a position to characterise the red MOT, realise a narrowband red MOT and load atoms in optical lattice. For the lattice trap, we have already tested the lattice optics. Once atoms are trapped, the next step in this project is clock transition interrogation and clock laser stabilisation to the atoms. In the next chapter we will go on to discuss the 30 mm optical reference cavity that have been employed to frequency stabilise the laser systems used for our strontium optical clock.

Chapter 4

Development of frequency stabilisation units

In the previous chapters we have discussed the frequency stability requirements of the various lasers used for cooling and trapping strontium atoms. In this chapter we discuss the design of a compact optical reference cavity, and the development of frequency stabilisation systems including a multiple frequency stabilisation unit (FSU) using the optical reference cavity for locking the lasers required to realise a strontium optical lattice clock. The lasers we wish to lock are 689 nm, 813 nm, 679 nm, 707 nm, and 461 nm. So far we have locked 689 nm, 813 nm, and 679 nm. The 707 nm laser was not ready to use while we performed multiple frequency stabilisation, and 461 nm laser was then locked to the strontium spectroscopy cell. The following sections will cover details about the Fabry-Perot (FP) cavity, vacuum system, frequency stabilisation unit for multiple laser locking, and characterisation of the cavity and lasers.

4.1 Optical reference cavity

The optical reference cavity is a horizontally mounted, 30 mm long, cylindrical, 1 inch diameter FP cavity. This is the cavity that is being employed in the multiple frequency stabilisation unit described in section 4.7. Photographs showing the size of the cavity against a one pound coin is depicted in Figure 4.1. The cavity is very compact in order to make the whole FSU system portable. This cavity is modelled by Dariusz Świerad during his PhD [118]. Earlier versions of compact reference cavities can be found in references [119, 120]. The spacer is made of ultra-low expansion glass (ULE) and the mirrors are made of fused silica. Two types of spacers were built: one without vent hole and one with vent hole (3 mm diameter). We used cavities with vent holes in the experiments conducted under vacuum. One of the two mirrors is planar whereas the other

is curved with a radius of curvature of 500 mm. The mirrors are AR (anti-reflection) coated at the back facet and HR (high reflectance) coated at the inner facet at different wavelengths in accordance with the strontium transitions: 461 nm, 679 nm, 689 nm, 698 nm, 707 nm, 813 nm, and 922 nm. A company called Layertec manufactured the mirrors with customised coatings. The mirrors are optically contacted to the spacer to avoid any third party such as adhesives, solder in between so that the surface flatness and coefficient of thermal expansion are well maintained.

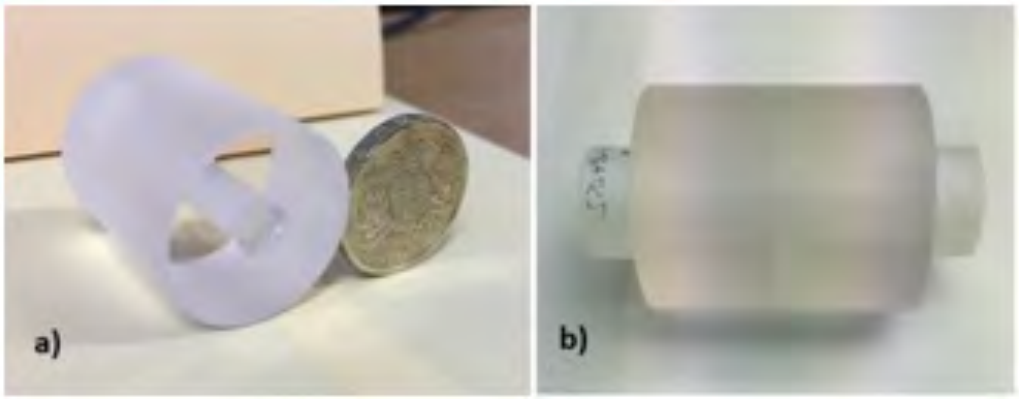

Figure 4.1: a) ULE spacer with a one pound coin for comparison. b) FP cavity. Fused silica mirrors are optically contacted onto the 30 mm long ULE spacer.

Ultra-low expansion materials are ideal for building reference cavities as they have a very low coefficient of thermal expansion (CTE), i.e., a very low expansion in the material length due to temperature fluctuations. Reference cavities are always affected by the length change of the material they are build of, due to temperature and air pressure fluctuations [121]. Fractional length variations in the reference cavity lead to fractional variations in the resonance frequency of the cavity according to the equations:

$$\frac{\Delta L}{L} = \alpha \Delta T, \tag{4.1}$$

and

$$\frac{\Delta L}{L} = \frac{\Delta \nu}{\nu}, \tag{4.2}$$

where L is the length of the cavity, ΔL is the change in cavity length, α is the coefficient of thermal expansion of the material, ΔT is the change in temperature, ν is the resonance frequency, and $\Delta \nu$ is the change in the resonance frequency of the cavity. For example, a length change of 1 pm or 1 fm of the 30 mm cavity leads to a frequency change of 14 kHz or 14 Hz, respectively. There are several groups around the world who have achieved this length stability and hence, sub-hertz laser linewidth at 1 s interrogation time [122, 100]. In our case, we need to achieve a frequency stability of 7.5 kHz or less for the 689 nm laser. That means, the length change of the cavity should be less than 0.5 pm to achieve the required frequency stability.

4.1.1 Cavity stability criteria

If a reference cavity is stable it means that a beam propagating through the cavity is converging to a region on the axis of the cavity and still continues to converge rather than to diverge after multiple passes through the cavity. Ray transfer matrix (otherwise known as ABCD matrix) is used to study many successive round trip propagation of a beam through a cavity (between mirrors) and determine the conditions during which the beam converges within the cavity. ABCD matrix is otherwise a mathematical formulation (matrix representation) of the round-trip propagation of a beam within a cavity [113, 123]. The propagation of a beam from point x_1 to x_2 can be expressed using ABCD matrix in the form:

$$\begin{bmatrix} x_2 \\ \theta_2 \end{bmatrix} = \begin{bmatrix} A & B \\ C & D \end{bmatrix} \begin{bmatrix} x_1 \\ \theta_1 \end{bmatrix}, \tag{4.3}$$

where θ_1 and θ_2 are the angular direction of propagation of the beam with respect to axis. If $x_1 > x_2$ and $\theta_1 > \theta_2$ then the beam is converging leading to a stable cavity. A, B, C, and D are the elements derived by combining and simplifying the matrices for the round-trip propagation of a beam within the cavity.

The matrices required to create a ray transfer matrix for the cavity considered in this project are:

Matrix for a planar mirror $M_p = \begin{bmatrix} 1 & 0 \\ 0 & 1 \end{bmatrix}$, matrix for translation distance d in the optical cavity $M_d = \begin{bmatrix} 1 & d \\ 0 & 1 \end{bmatrix}$, and matrix for a curved mirror $M_c = \begin{bmatrix} 1 & 0 \\ \frac{-2}{R} & 1 \end{bmatrix}$, where R is the radius of curvature of the mirror. For a Fabry-Perot cavity formed of a planar and curved mirror, the ray transfer matrix is represented as:

$$M = M_p M_d M_c M_d. \tag{4.4}$$

Let's define M as,

$$M = \begin{bmatrix} A & B \\ C & D \end{bmatrix}. \tag{4.5}$$

For a beam propagating within a cavity to satisfy the stability criteria, the condition to be satisfied is $-1 < (A + D)/2 < +1$ [112]. The condition can also be written in terms of radii of curvature of mirrors (R_1, R_2) and the translational distance, d, as the following:

$$0 < \left(1 - \frac{d}{R_1}\right)\left(1 - \frac{d}{R_2}\right) < 1, \tag{4.6}$$

or

$$0 < g_1 g_2 < 1, \tag{4.7}$$

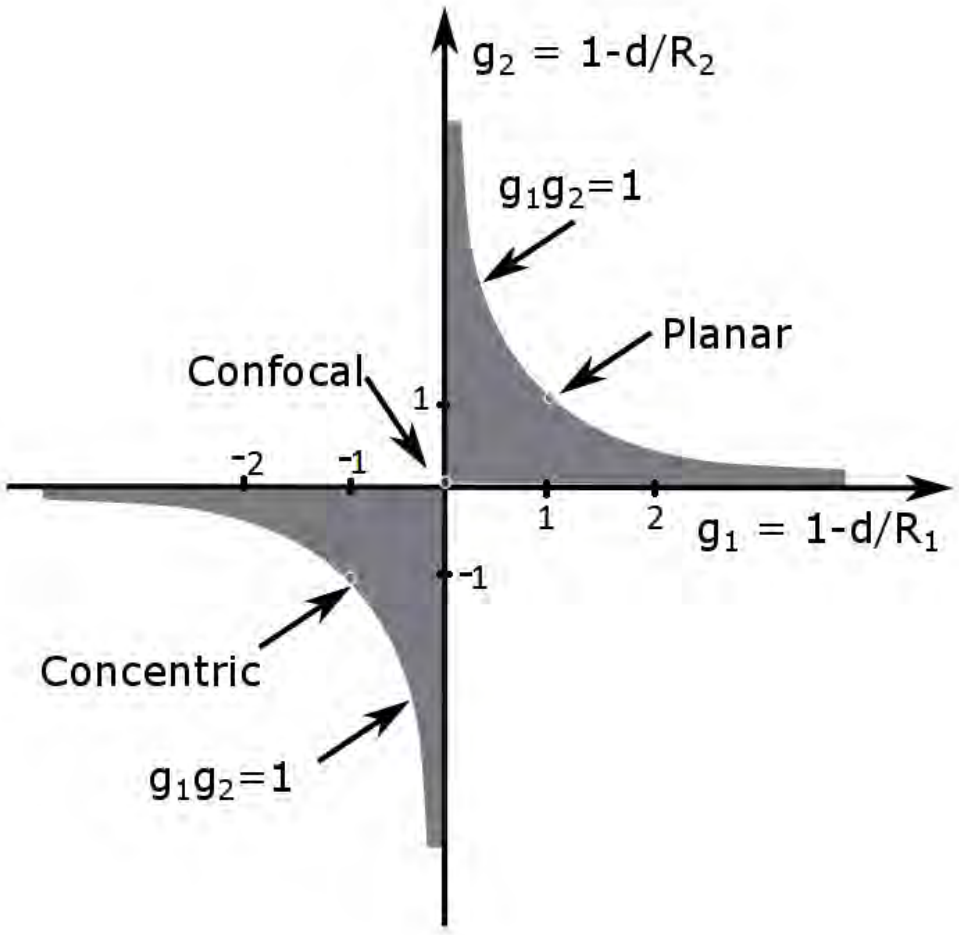

Figure 4.2: Stability diagram for two mirror cavities.

where g_1=1-$\frac{d}{R_1}$ and g_2=1-$\frac{d}{R_2}$. Figure 4.2 is the stability diagram for two mirror cavities. The shaded area represents stable systems and unshaded region portrays unstable systems.

The ray transfer matrix for the 30 mm FSU cavity with a planar mirror, and a curved mirror with radius of curvature 500 mm is calculated as follows:

$$\begin{bmatrix} A & B \\ C & D \end{bmatrix} = \begin{bmatrix} 1 & 0 \\ 0 & 1 \end{bmatrix} \begin{bmatrix} 1 & 30 \\ 0 & 1 \end{bmatrix} \begin{bmatrix} 1 & 0 \\ \frac{-2}{500} & 1 \end{bmatrix} \begin{bmatrix} 1 & 30 \\ 0 & 1 \end{bmatrix}, \tag{4.8}$$

$$M = \begin{bmatrix} A & B \\ C & D \end{bmatrix} = \begin{bmatrix} 0.8800 & 56.4000 \\ -0.0040 & 0.8800 \end{bmatrix}, \tag{4.9}$$

and $(A+D)/2$ is 0.88 meaning that the beam propagating through the cavity is tending to stability by converging to the optical axis of the cavity.

4.2 Assembling the cavity

A cavity is formed when the mirrors and the spacer are assembled together. There are several ways to realise a cavity. We have chosen optical contacting technique to form the cavity [124, 125]. It is a technique where the mirrors are contacted to a cavity using intermolecular forces. However, intermolecular forces are often not sufficient to hold two bodies together as any irregularity in the surface leads to a very weak bonding. Therefore, a high degree of surface flatness is necessary for the intermolecular forces to be strong enough to bond the materials together. The spacer and mirrors are machined in such a way that ensures a surface flatness of $\lambda/10$, so as to be compatible for optical contacting. Figure 4.3 describes the process for optical contacting technique. The process has to be carried out in a clean room. First, contacting surfaces are examined under a microscope to check for any contaminations. If any are found, the surfaces are cleaned by rubbing ultra-pure (99.9%) acetone using a well folded cleansing tissue paper. The cleaning process is very important as any dust particle will reduce the surface smoothness and thereby weaken the bonding between the surfaces. Once the surfaces are clean enough, one is placed on top of the other. During this process, interference fringes developed between the contacted surfaces indicate the presence of air. The fringes are formed by the reflection of light from the contacted surfaces through air. When two flat surfaces are placed on top of each other, straight and parallel fringes are formed. Subsequently, the surfaces are pressed with finger very hard for a duration of few seconds to minutes. When the surfaces are well bonded, the interference fringes disappear. The separation between the bonded bodies ranges between 0 to 200 angstrom [126].

The main feature of optical contacting is that no auxiliary materials such as adhesives or solder are used in the bonding process. The advantages of the technique are that the overall dimensions are

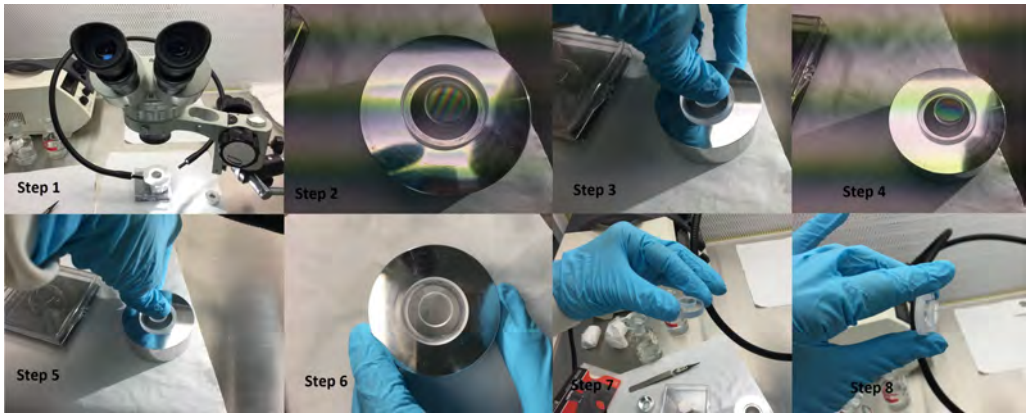

Figure 4.3: Steps describing the optical contacting process. Step 1: Ensure that the optics are very clean by visual examination through a microscope. Step 2: Once the optics are cleaned, they are placed one on top of each other. This arrangement leads to the formation of interference fringes between them due to the presence of air. Step 3: Pressing hard to increase the intermolecular bonding between the optics. When the distance between the two inner surfaces is reduced, air is expelled. Step 4: After pressing (i.e, applying force), distance between the interference fringes is increased stating that the distance between the two inner surfaces are reduced. Step 5: Repeated application of force. Step 6: The interference fringes are completely gone indicating that the intermolecular forces between the surfaces are strong enough to hold the optics tightly together. Step 7 and 8: Moving, shaking and tilting of the bonded optics to ensure that the bonding is sufficiently strong.

kept unchanged, the optical system is transparent as there is no third party bonding layer, no outgassing at higher temperatures, no additional drifts due to another material, and no internal stress [125]. These properties are very relevant in the field of precision measurements and technology where ultra-stable lasers, optical cavities, and optics, play major roles.

4.3 Mounting the cavity

Now that we have made the cavity, we need to consider how it will be mounted. The cavity needs to be rigidly supported within the housing, while keeping the external forces to a minimum. This will reduce any vibrations affecting the cavity. It also needs to be temperature stabilised to minimise any effect on the material which leads to frequency instability.

The cavity is mounted in a two layer aluminium housing. Aluminium is chosen due to its good thermal conductivity of 205 W/m.K at 25°C. Viton balls are used to support the cavity within the housing. If it is not mounted properly, the material will bend leading to frequency drift over time. The housing acts as both cavity housing as well as thermal shielding. The cavity is isolated from the environment using the aluminium shielding.

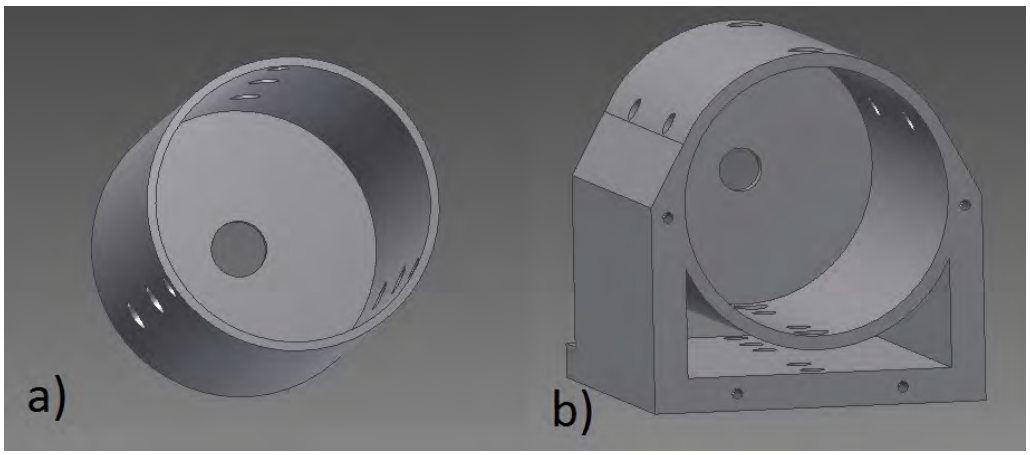

Figure 4.4: a) Inner housing (first housing). Cavity is kept in the inner housing using the support of six viton balls. b) Outer housing (second housing) where the first housing is placed within.

The cavity is first placed in the inner house as depicted in Figure 4.4(a) by using viton balls to support it. Viton balls with 4 mm diameter are chosen for this purpose as they can be pressed to insert the cavity to the housing. They are rigid enough to keep the cavity in place, without affecting the optical axis. There are six viton balls between the cavity and inner housing. They are arranged in three columns at an angle of 120° with two balls in each column. Holes in the housing ensure that the balls stay between the cavity and the housing. The inner housing is placed in a

second housing which is shown in Figure 4.4(b). There is another set of six viton balls to hold the inner housing within the outer housing. All together, there are twelve viton balls used to mount the cavity inside the aluminium housings. The whole assembly is shown in Figure 4.5.

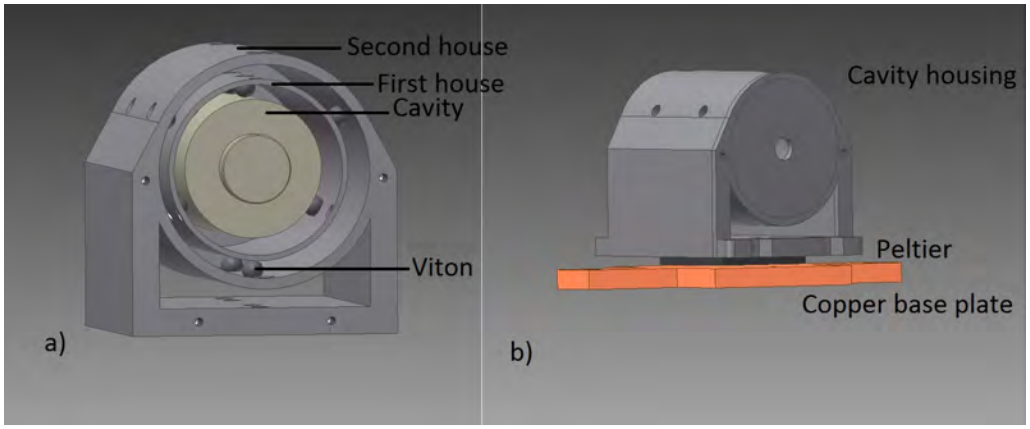

Figure 4.5: a) Description on how the cavity is mounted in each housing. b) Shows the complete assembly.

A peltier element is employed between the cavity housing and a copper base plate to stabilise the temperature of the cavity. A 10 kΩ thermistor is used to monitor the temperature value. The temperature of the cavity housing is measured using a Tinytag ultra 2 temperature logger. It has an external sensor which can be placed on a test system. The data is logged on a computer using a dedicated software. The measurements shown in Figure 4.6 were taken every 10 seconds continuously for 60 hours. Notably, the temperature is relatively stable during the night, and it fluctuates significantly while there are more people in the lab, and during frequent opening and closing of the lab doors. There is no sensor placed right on the cavity to measure the exact cavity temperature.

4.4 Vacuum system

The cavity is under vacuum for a better thermal stability and a lower frequency drift rate. The non-vacuum cavity characterisation results described in section 4.8 revealed larger drifts which led to the idea of putting the cavity under vacuum. Vacuum is necessary to reduce any refractive index fluctuations due to pressure and humidity changes. It also improves the temperature stability of the cavity by ceasing convection currents in the system. The vacuum level of the cavity is 2×10^{-7} mbar before closing the valve.

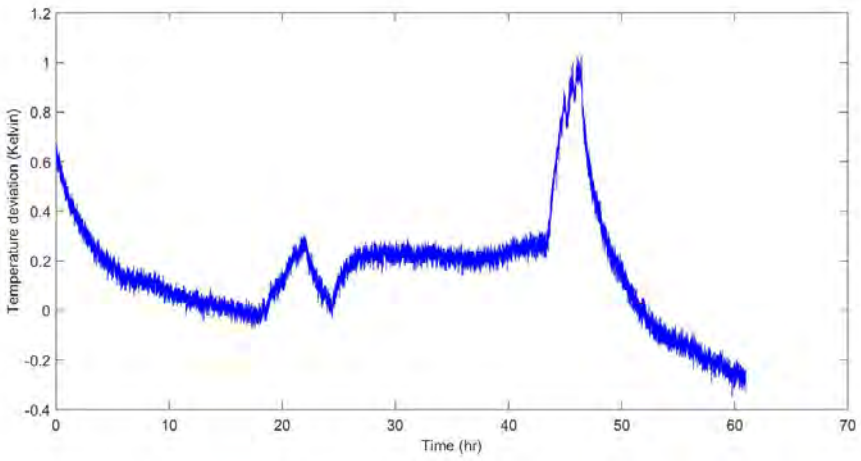

Figure 4.6: Temperature measured outside the chamber showing passive temperature stability. The two peaks in the graph show temperature fluctuations when people were moving in and out of the lab.

4.4.1 Vacuum chamber

The vacuum chamber shown in Figure 4.9(h) is made of titanium which has a thermal conductivity of 19-23 W/m.K. There are two aluminium layers, which are described in section 4.3, inside the titanium vacuum chamber. Titanium was chosen as outer layer instead of aluminium as it is harder than aluminium. The chamber has got two DN16CF (ConFlat flange vacuum joint) ports with knife edges, which are usually difficult to build using aluminium due to its softness. Knife edge on aluminium tend to make a system fragile over time. Titanium is harder than aluminium and thus, it can be used for gasket sealing which requires knife edges. Another choice would be space-qualified aluminium, which is harder than normal aluminium. However, our time constraints, cost effectiveness, and the easy availability of titanium led us to choose this material. A peltier element between the second housing of the cavity and the titanium layer controls the temperature of the cavity. The temperature of the cavity is mostly determined by the conduction mechanism from the first (inner) housing layer of the cavity, but still it is affected by the vacuum chamber layer and the outside environment. The peltier element used in the system is a 30 mm $\times$ 30 mm $\times$ 4.7 mm with a maximum current of 4 A. There are two 10 kΩ thermistors in the vacuum system. One for completing the feedback loop and the other for monitoring temperature inside the vacuum chamber. The two end surfaces of the chamber have a 30 arcmin wedge angle to avoid any parasitic etalon effect which arises between optics mounted in parallel leading to frequency fluctuations. Fused silica windows (WW41050, Thorlabs) with 30 arcmin wedge angle are sealed to the end surfaces of the chamber employing indium sealing method. Laser beams are coupled to the cavity through these windows. In order to make the system compact, the outer

dimensions of the vacuum chamber are kept as 9.8 cm × 8.4 cm × 7.2 cm and inner dimensions as 7 cm × 6 cm × 6.13 cm. The cavity housing is clamped to the vacuum chamber using 'PEEK' (polyether ether ketone) screws as they are thermally and electrically insulating plastic screws compatible with ultra-high vacuum.

Vacuum chamber components

In the vacuum chamber, there are additional components to complete the system. To connect the peltier element and the two 10 kΩ thermistors to the temperature controller outside the chamber, a DN16CF vacuum electrical feedthrough (FHM-M7-16CF, LewVac) with 7 pins and a maximum current of 15 A is used. It is sealed to the vacuum chamber through one of the two DN16CF ports using a DN16CF copper gasket. The temperature components are connected to the feedthrough using vacuum compatible connectors.

CapaciTorr pump

A CapaciTorr pump (CF16 MK2, SAES) is a vacuum pump which can absorb active gases, see Figure 4.7. This does not pump any noble gases. Instead of the usual ion pump, we use CapaciTorr

Figure 4.7: CapaciTorr pump (Image taken from CapaciTorr pump user manual).

pump mainly to reduce the size of the system. Pump activation has to be done carefully. Once the pump head is connected through a DN16CF port to the vacuum chamber, it is connected to a current source. Before activating the pump, the vacuum system is pumped down to lower than 1×10^{-4} Torr. The activation process took around 150 minutes. Electric current is increased from 0 A to 5 A step by step in 150 minutes, and the temperature reached up to 435°C. The maximum operating temperature is 600°C. Once the pump is heated to a suitable temperature, the getter material activates and it initiates the pumping action. After activation process, the current source is turned off and the pump is used at room temperature.

Valve and Tee

A DN16CF tee is used to connect the CapaciTorr pump and the vacuum valve to the chamber. The DN16 angle valve (28424-GE01, Kurt. J. Lesker) is made of stainless steel, see Figure 4.8. The leak rate of the valve is 5×10^{-10} mbar/ls and it can support reaching a minimum pressure range of 1×10^{-10} mbar. It is mainly used to isolate the vacuum chamber from the turbo pump. The tee is also made of stainless steel. It has knife-edge flanges.

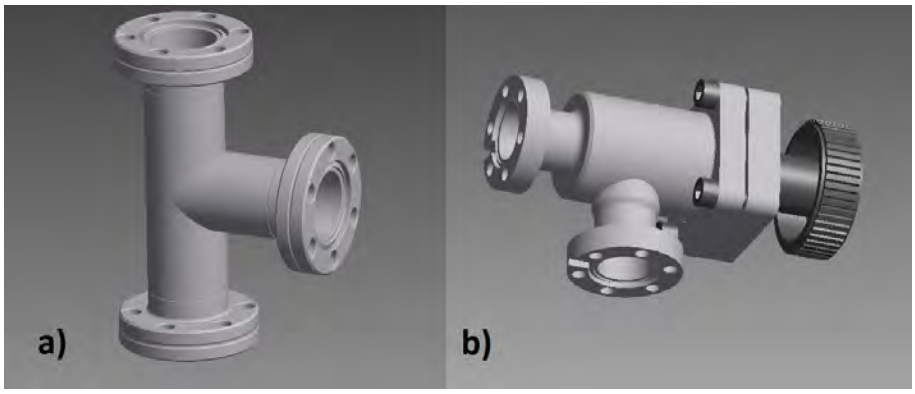

Figure 4.8: a) DN16CF tee with one fixed and two movable flanges. b) DN16 angle valve for ultra-high vacuum.

4.4.2 Indium sealing

A soft material indium is used as a vacuum sealant. The technique is developed by Adam et al [127]. Different types of materials such as ULE, quartz, germanium, pyrex, oxygen free copper, invar, and titanium can be sealed using indium [128]. Indium is flexible enough to be used in any configuration needed for the system. It also requires very low force compared to copper gasket sealing [129]. The seal is long lasting, while being removable using acetone.

We used indium with 1 mm thickness to seal the lid of the titanium vacuum chamber, and the fused silica windows onto the chamber. It is highly important to have a flat, smooth and clean surface for indium sealing. The vacuum chamber is machined and the surfaces are polished in the workshop. The vacuum chamber and related components are cleaned using soap solution, followed by water, propanol, and acetone in an ultra-sonic bath. The indium wire is cleaned using propanol. Care must be taken not to apply force while cleaning it. Any force can change the shape of indium wire and this causes a weak sealing.

The chamber-fused silica window indium seal has a teflon spacer above the window. This configuration is designed to avoid any scratch on the window due to the copper compression flange. Indium sealing process is described in Figure 4.9.

The sealing process is as follows: Indium is cut to the required length. The two ends of the wire

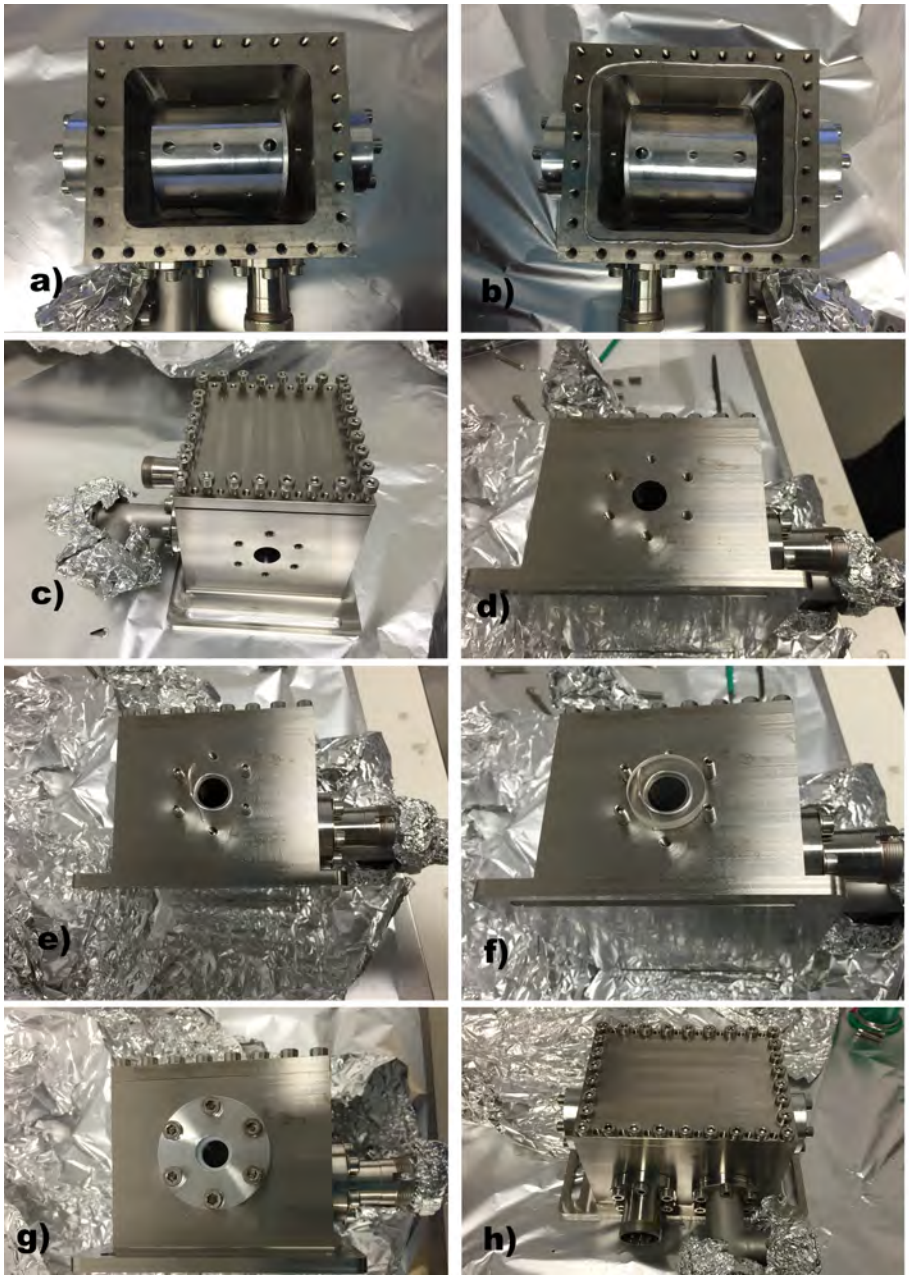

Figure 4.9: Different stages of indium sealing. a) Titanium chamber containing the cavity housing cleaned with propanol and acetone. b) 1 mm diameter indium wire is placed on the chamber in a rectangular shape. c) Titanium lid is placed over the indium wire and the screws are tightened evenly. d) Surface for indium sealing with fused silica window. e) Indium wire is placed on the surface in a circular shape. f) Place the window over the indium carefully. g) Put teflon spacer, fused silica window and aluminium compression flange on top of each other, tighten carefully. h) Sealed vacuum chamber.

are placed on top of each other and it is cut at an angle using a sharp knife. The newly cut ends are pressed together until there is no air gap between them. Once the chamber and indium are cleaned properly, the indium wire is placed on the chamber. The lid is put on top of the indium wire and tighten it evenly using M4 screws. Fused silica mirrors are sealed to the two wedged surfaces using indium. For sealing, a teflon spacer and an aluminium compression flange are used on top of each of the fused silica windows.

4.5 Cavity finesse

The finesse of a cavity is defined as the number of bounces a propagating beam experiences inside the cavity before it is transmitted or absorbed. This is dependent on the reflectivity of the mirrors. Any loss, scattering, micro/macro roughness, or non uniform coating on the mirrors are factors affecting the finesse of a cavity. The finesse is given by:

$$\mathcal{F} = \frac{\pi}{2\arcsin\frac{1-R}{2\sqrt{R}}}. \tag{4.10}$$

When $R{\approx}1$, by using Maclaurin series expansion, above equation can be simplified to the form:

$$\mathcal{F} \approx \pi\frac{\sqrt{R}}{1-R}, \tag{4.11}$$

where R is the mirror reflectivity. In the equation, only mirror reflectivity is taken into account assuming that other contributing factors are negligible.

Figure 4.10 shows the variation in cavity finesse with respect to mirror reflectivity. Table 4.1 summarizes the parameters such as reflectivity, finesse, decay time (τ), and linewidth for the 30 mm cavity at different wavelengths. The reflectivity values are obtained from the technical datasheet of the mirror. The rest of the parameters are calculated from the mirror reflectivity employing the equations 4.11 and 4.13.

4.5.1 Cavity ring-down spectroscopy

Cavity finesse measurement is usually performed by cavity ring-down spectroscopy. This method is mainly used to measure the finesse of high-finesse cavities, because for low-finesse cavities the decay time is too fast to easily measure on a photodiode. With high-finesse cavities the linewidth of the lasers are likely to be larger than that of the cavity modes, so it is difficult to measure the linewidth, and hence the finesse, directly by measuring the transmission because there will be a lot of fluctuations. In these cases, ring-down spectroscopy is employed as a suitable alternative.

The laser beam on resonance with the TEM_{00} mode of the cavity interferes constructively between the mirrors. This interference leads to the build-up of intra-cavity power when the laser

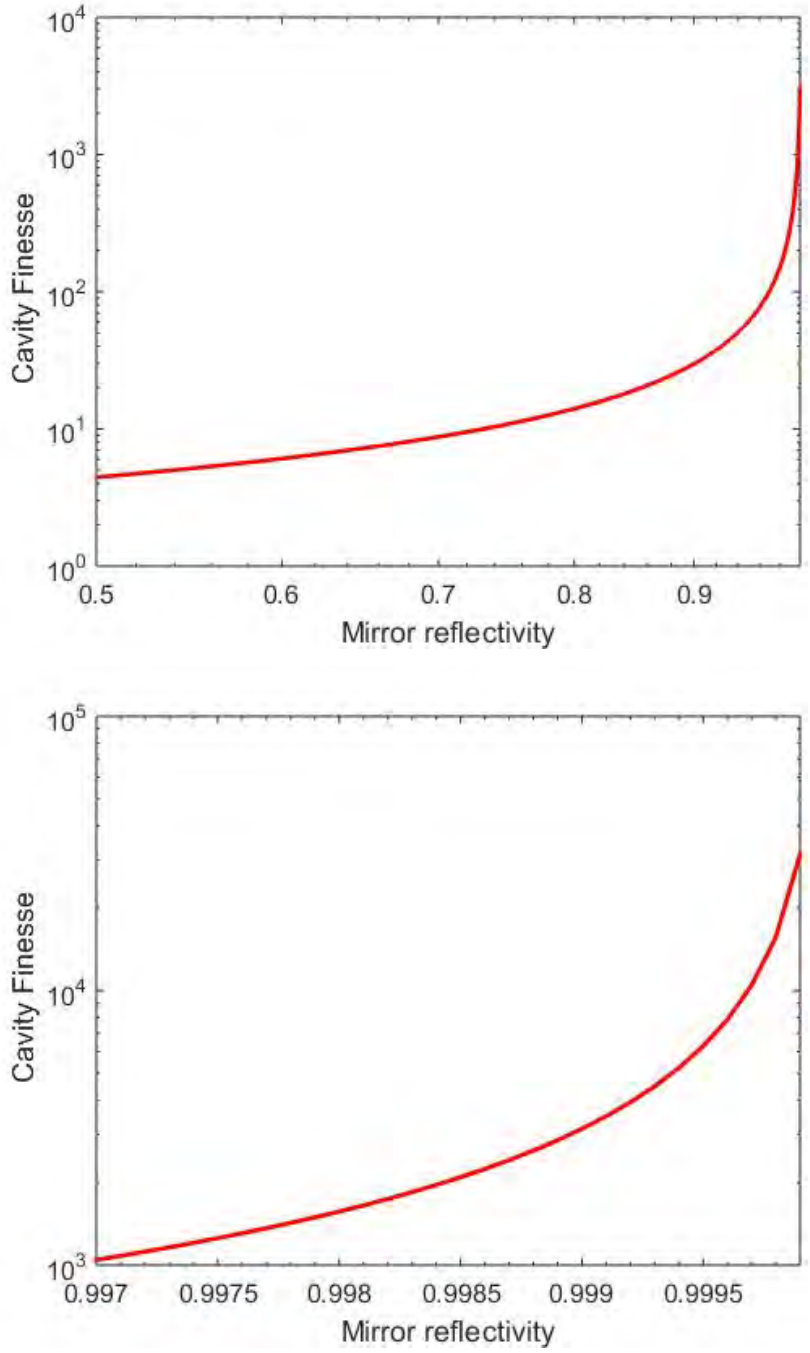

Figure 4.10: Cavity finesse as a function of the reflectivity of the mirrors.

Wavelength (nm)	Mirror reflectivity	finesse	τ (μs)	linewidth (kHz)
461	0.997	1050	0.03	4800
679	0.99968	9800	0.3	510
689	0.99968	9800	0.3	510
698	0.99977	13650	0.5	300
707	0.99978	14270	0.56	286
813	0.9968	980	0.03	5100
922	0.9974	1200	0.04	4200

Table 4.1: Summary of parameters for the FP cavity. The mirror reflectivity is obtained from the datasheet. Finesse, power decay time τ, and linewidth for each wavelength are calculated from the reflectivity values employing the equations 4.11 and 4.13.

is locked on resonance. Usually, several μW of incident beam power leads to an intra-cavity power of the order of a Watt. The build-up power decays when the incoming laser beam to the cavity is blocked or its frequency is changed. This decaying power is monitored and measured using a fast photodiode. Cavity decay time can be deduced which can then be employed to calculate cavity finesse using equation 4.13.

In our system, we used an AOM (acousto-optic modulator) with 32 ns rise and fall time to block the beam going to the cavity. For that, the beam is initially sent to an AOM which operates at 80 MHz frequency. It is then coupled to an optical fibre which is connected to a fibre coupled EOM. The beam is then aligned to the cavity. As we use an AOM, any change in frequency of the AOM blocks the laser beam off from resonating inside the cavity. This technique is used to perform the ring-down spectroscopy. The transmitted output is detected using a 150 MHz bandwidth photodetector. The output of the photodetector is connected to an oscilloscope.

The cavity linewidth $\delta\nu$ is related to the decay time of the intra-cavity power by the following relation:

$$\delta\nu = \frac{\delta\omega}{2\pi} = \frac{1}{2\pi\tau}, \tag{4.12}$$

where $\delta\omega$ is the angular frequency.

From this equation, the finesse is obtained as:

$$\mathcal{F} = \frac{FSR}{\delta\nu} = \frac{c}{2L}2\pi\tau. \tag{4.13}$$

Figure 4.11 shows the ring-down spectroscopy transmission curve for 689 nm wavelength. The

data is fitted using an exponential decay function. The decay constant, τ, measured from the data is 0.302±0.003 μs and the finesse is 9476±95. There is 3% discrepancy from the calculated value shown in Table 4.1.

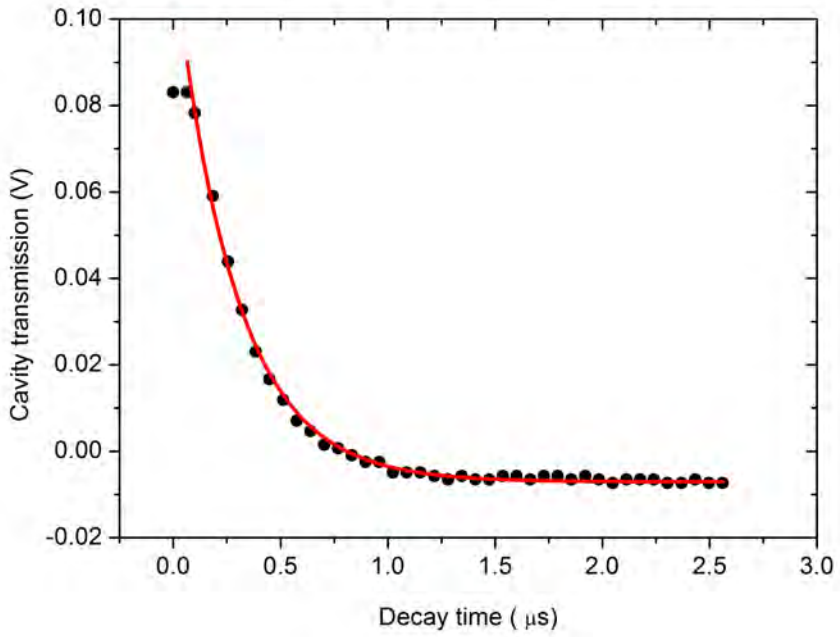

Figure 4.11: Vacuum cavity ring-down measurement at a wavelength of 689 nm. The data points are fitted with an exponential decay function. The decay time obtained is 0.302±0.003 μs. The respective finesse is calculated as 9476±95.

The decay time is the time taken by the intra-cavity laser beam power at a decay of $1/e$ of its initial power. The experiment is performed with the cavity in the vacuum chamber. Along with the high reflectivity, a very clean, dust free environment is highly important to achieve a high finesse for the reference cavity. The spacer and mirrors are properly cleaned using acetone and propanol before putting in vacuum. This helped in achieving a higher finesse compared to what we measured when the cavity was kept in air.

Figure 4.12 shows the ring-down spectroscopy performed while the cavity is outside vacuum. The decay time is 0.102±0.001 μs and the finesse is 3200±31 which is lower than the expected value. This deviation could be due to the exposure of the cavity to outer environment causing dust particles sticking onto the mirror. Such a contamination can lead to scattering and irregular surfaces which reduce the number of times the beam bounces back and forth within the cavity.

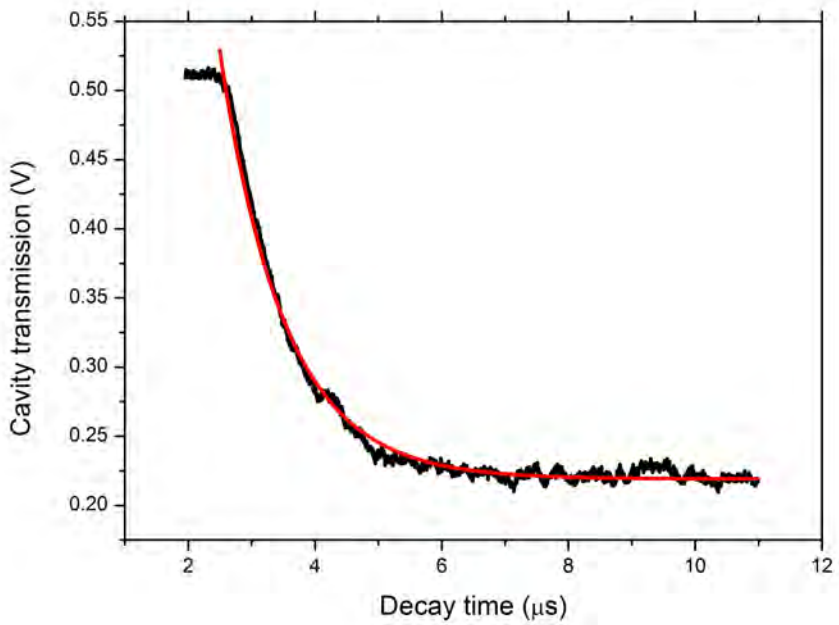

Figure 4.12: Non vacuum cavity ring-down measurement at a wavelength of 689 nm. The data points are fitted with exponential decay function. The decay time obtained is 0.102±0.001 μs. The finesse is calculated as 3200±31.

4.5.2 Cavity finesse measurement using an ultra-narrow linewidth laser

A second way to measure the linewidth of a cavity is to scan across the cavity modes using a highly-stable and ultra-narrow linewidth laser. We used a 698 nm clock laser less than 1 Hz linewidth [118] to scan through the cavity modes, its linewidth is very narrow compared to the cavity linewidth of 300 kHz at 698 nm, see Table 4.1. The clock laser is stabilised to a 10 cm ultra-stable cavity by locking to the TEM_{00} mode. Another output of the clock laser is sent through an EOM and coupled to the cavity which is inside the vacuum. A modulation frequency is applied to the EOM so that it could generate sidebands on the laser frequency. The modulation frequency of the EOM is tuned to scan the laser across the cavity resonance. When the laser is on resonance with the TEM_{00} mode of the cavity, the transmission peak is detected using a photodetector. A Lorenztian fit to the transmitted peak gives the cavity linewidth.

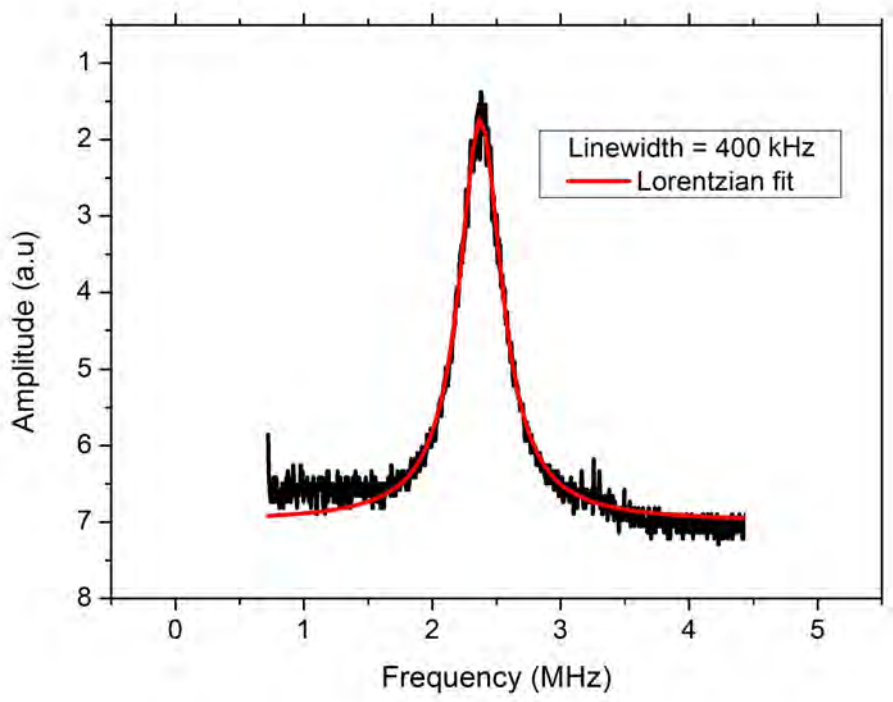

Figure 4.13: Linewidth of the reference cavity at 698 nm. The data is fitted with Lorenztian function.

Figure 4.13 displays one of the transmission spectra obtained by scanning the clock laser across the cavity. The cavity linewidth obtained through this method is 400±4 kHz. The measurement is repeated many times to obtain an accurate and precise measurement. The resulting cavity finesse at 698 nm is 12455±125. There is 8% difference between the measured and the calculated finesse values.

4.5.3 Free spectral range of the cavity

The free spectral range (FSR) of a cavity is the distance in frequency between two TEM_{00} modes. It is also defined as the difference in frequency that causes a 2π phase shift between two successive round-trips of the laser beam inside the reference cavity [94]. For a FP cavity, it can be written as

$$FSR = \frac{c}{2L}, \tag{4.14}$$

where L is the cavity length and c is the velocity of light in vacuum. Finesse and free spectral range combined determine the cavity linewidth as illustrated in Figure 4.14. The cavity linewidth becomes narrower when the mirror reflectance increases. It is written as,

$$\delta\nu = \frac{FSR}{\mathcal{F}}. \tag{4.15}$$

From equations 4.14 and 4.15, it is understood that the cavity length also plays a major role in determining the cavity linewidth. Therefore, longer cavities are often preferred for ultra-stable frequency reference systems [130, 131, 132, 133].

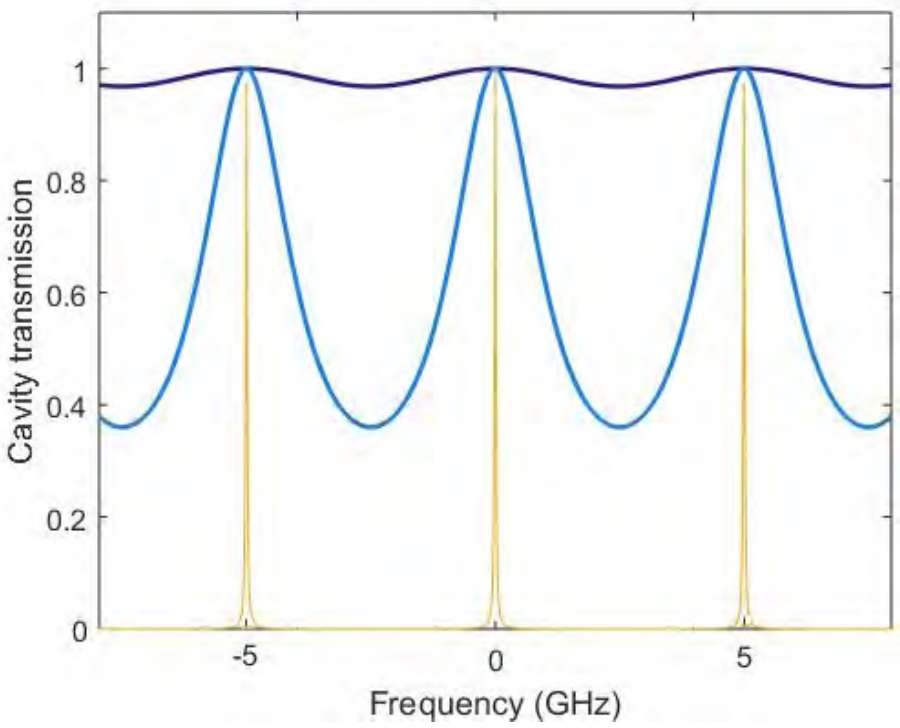

Figure 4.14: Theoretical plot showing transmission peaks through a 5GHz free spectral range cavity. Peaks occur every 5 GHz. The linewidth becomes narrower when the mirror reflectivity increases. The peaks are plotted at three different reflectivity values: 0.99 (yellow), 0.5 (blue) and 0.09 (dark blue).

The FSR of the cavity is measured by a laser at 689 nm which is stabilised to the cavity. One of the outputs of the laser is connected to a wavemeter with a resolution of the order of 10 MHz. The TEM_{00} mode of the cavity is measured at a certain frequency. The frequency is then changed by scanning the PZT until the next TEM_{00} mode is obtained. The frequency of the new mode is also noted. The difference between these two frequencies results in the FSR of the cavity. This measurement is repeated couple of times on several days. From the data obtained, the free spectral range of the cavity is 4.995±0.010 GHz. This is very close to the expected FSR of 5.000 GHz.

4.6 Zero coefficient of thermal expansion

The zero coefficient of thermal expansion (zero CTE) is measured using a stabilised clock laser and the cavity to be tested. The test cavity has a single layer temperature stabilisation using a peltier element as described in section 4.4.1. The clock laser which is locked to an ultra-stable cavity is coupled to the test cavity through a wideband tunable EOM. The EOM is driven using a function generator (HM8135, Hameg) which is referenced to a rubidium frequency standard, which also serves as a reference for all the frequencies related to the clock laser and the ultra-stable cavity. The function generator and the oscilloscope to monitor the transmission are triggered using another function generator (3380, Keithley) which is also referenced to the rubidium frequency standard. The modulation frequency is changed with a 10 MHz step to see the TEM_{00} mode of the cavity to which the clock laser is on resonance with. The measurement is repeated several times, each time at different temperatures. As the cavity temperature changes, the frequency of the TEM_{00} modes also changes, which leads to a different modulation frequency for the scanning laser beam to become resonant with the cavity mode. A curve is obtained by plotting the modulation frequency against corresponding temperature. The data obtained follows a quadratic behaviour. This is shown by fitting the data using a quadratic function.

Figure 4.15 shows the plot used to find the zero CTE of the FSU cavity. The fitting shows that the zero crossing temperature for the cavity is at 23.3°C. This result is important as it decides at which temperature should we keep our cavity. Now the temperature controller set point is tuned to 23.3°C for getting the best performance out of the cavity.

4.7 Multiple frequency stabilisation unit for strontium lattice clock

The development of a multiple frequency stabilisation unit (FSU) is one of the major parts of the miniclock project. The FSU is a compact stabilisation unit for all the lasers which are required to

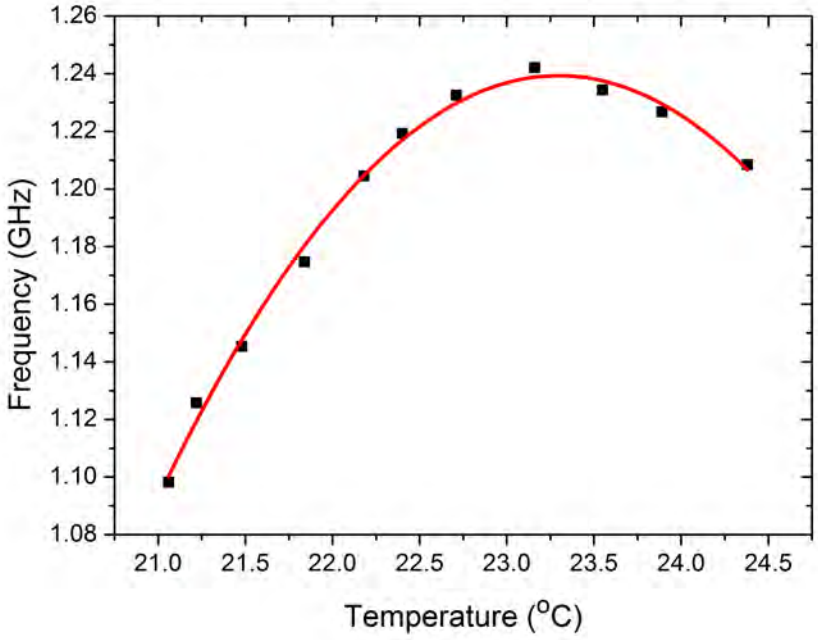

Figure 4.15: Plot for zero CTE of the FSU cavity. The zero CTE for the cavity is at 23.3°C. This is obtained from the quadratic fit (red) to the data points (black) shown in the plot. The measurements are taken at different cavity temperatures.

obtain a clock transition using strontium atoms. Essentially, the FSU is for the locking of 689 nm, 679 nm, 707 nm, 813 nm, and 461 nm lasers. The clock laser is always locked to a very high finesse, ultra-stable cavity. The highlight of the system is that it works on a single reference cavity. This is a cost effective, low power, robust, and reliable system. In the FSU scheme, the most important aspect is the coupling of all laser beams into a cavity, and how the reflected beams coming out of the cavity are split. We have chosen an efficient way to distinguish between different laser beams reflected from the cavity, so that each laser could have dedicated servo loop for stabilisation. Total power consumption is also lowered to 5 W by the use of a passive getter pump and one peltier.

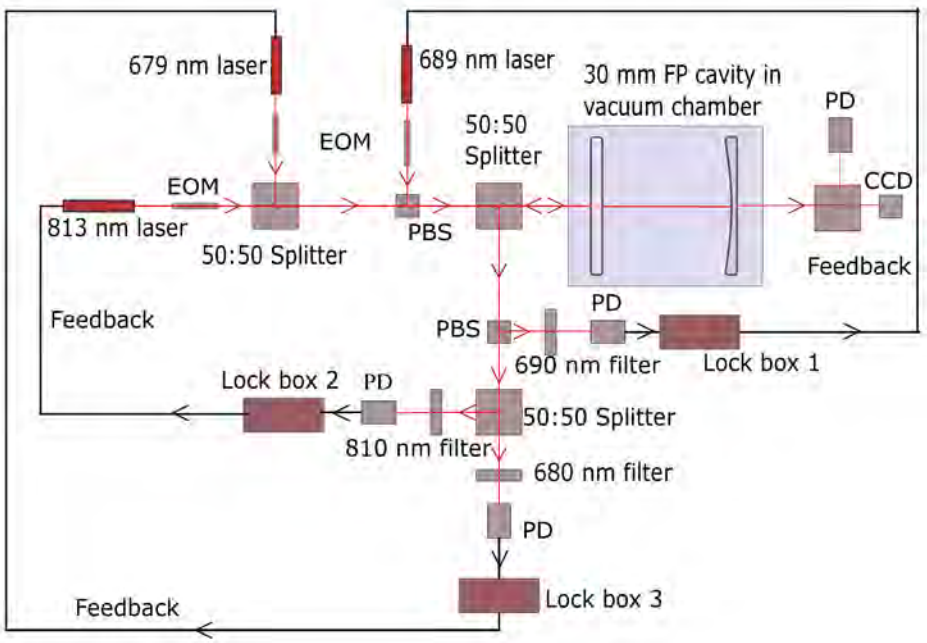

Figure 4.16: Schematic design of the multiple frequency stabilisation unit (FSU) for stabilising the wavelengths 689 nm, 679 nm, and 813 nm.

The FSU scheme we have implemented is shown in Figure 4.16. We did not try locking the first stage cooling laser at 461 nm to the cavity due to two reasons: One is, we could not obtain an EOM with a bandwidth of minimum 2.5 GHz. As the free spectral range of the cavity is 5 GHz, it is very likely that the laser beams require a large dual sideband modulation frequency to match with the resonance frequency of the reference cavity. The second reason is that we are using a spectroscopy-based locking system for the 461 nm laser. Therefore, it is not necessary to have a cavity-based locking for the laser. The 707 nm laser is also not locked, as the laser was not ready during the time of lock implementation. However, the scheme can be extended to any number of lasers by adding more optics for coupling the beam into the cavity and splitting the reflected beam

coming out of the cavity.

The nearest wavelengths 679 nm and 689 nm are chosen to be of two different polarisations to allow selecting the light reflected from the cavity depending on the polarisation of the beams. Each laser beam is sent through its respective fibre-integrated EOMs (Jenoptik PM 705 for 689 nm and 679 nm lasers, PM 830 for 813 nm laser). The 813 nm and 679 nm lasers are coupled using a 50-50 beam splitter (BS). These beams are coupled with the vertically-polarised part of the 689 nm laser on another 50-50 BS before entering the cavity. The combination of a half wave plate and a polarising beam splitter sets the right polarisation. The second beam splitter acts as a combiner as well as a splitter. After multiple passes inside the cavity, one part of the beam is reflected and one part of it is transmitted. The 50-50 BS in front of the cavity splits the reflected beam into different wavelengths using a scheme similar to the one described above. The initial splitting is based on the polarisation of the beams. After that, beams are again split using a 50-50 BS. A wavelength line-filter can be used to distinguish between different wavelengths, and to ensure that no other wavelength will interfere while performing the stabilisation of lasers. There are three photodiodes (PDA10A, Thorlabs) to detect the reflected beams at 689 nm, 679 nm, and 813 nm, respectively. The photodiode (PD) outputs are sent to phase detectors (ZRPD-1+, mini-circuits) where the frequency is mixed with the frequency from a local oscillator. The demodulated output of the phase detector is sent to the respective PID controller unit of the lock box. The output of the PID controller is fedback to the current and piezo controller of the laser. A separate servo loop for each laser allows independent stabilisation of each laser. Approximately 70 μW of the power of the 689 nm laser goes into the cavity, whereas the 679 nm laser sent 150 μW, and the 813 nm laser sent 100 μW of power into the cavity. The power in each sideband (ω_2) is kept below 25% of the total power in the carrier. In our FSU scheme, we are using a dual sideband locking scheme as mentioned in section 3.7. The power in the dual sideband (ω_1) is maximised to obtain a large error signal. The FSU is designed and implemented with a cavity inside the vacuum chamber. The characterisation of the system is performed using 689 nm laser which requires the most stable frequency among all the lasers locked to the cavity, and the clock laser. The results are described in section 4.9.

4.8 Characterisation of the cavity outside vacuum

The 689 nm homebuilt laser (UoB laser) described in section 3.4 is first locked to the 30 mm cavity, which is kept outside vacuum. The cavity was kept at 20.7°C as the zero CTE of the cavity was unknown during these measurements. The whole laser stabilisation unit is transported to NPL in a van as part of a collaborative project. Even after the transportation, the laser and the cavity

remained aligned, only optimisations were required to obtain the stabilised laser system back in working mode. The system is characterised using a very stable 689 nm laser with sub-10 kHz linewidth (NPL laser) situated in National Physical Laboratory (NPL), London [49]. The UoB laser is locked to the test cavity. A beat note of the UoB laser with the NPL laser is detected for all measurements described in this section.

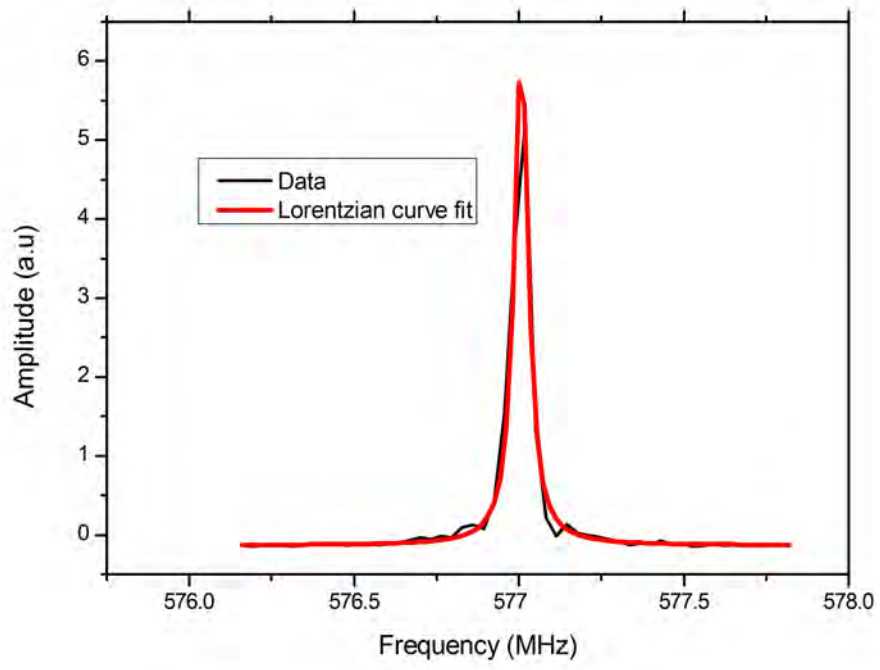

Figure 4.17: Linewidth of 98.9±0.3 kHz for 689 nm UoB laser obtained by measuring beat note between the UoB laser and the NPL laser.

A beat note set-up is made using 50-50 beam splitter, coupling mirrors, focussing lens, photodiode and spectrum analyser. The beat note between the UoB laser and NPL laser is detected using an avalanche photodiode with 2 GHz bandwidth. The frequency of the NPL laser is 434.829406 THz and that of UoB laser is 434.828829 THz. The beat note frequency is obtained at 577 MHz which is the difference between the two frequencies. The output of the photodiode is connected to a spectrum analyser to obtain the frequency output. The linewidth of the beat note is dominated by the linewidth of the UoB laser, since we know the NPL laser is much narrower. UoB laser linewidth is measured to be 98.9±0.3 kHz over a 1 s measurement time. The graph is plotted in Figure 4.17. This is much higher than the <7.5 kHz linewidth that we require for 689 nm laser.

The cavity drift is measured by monitoring the frequency drift of the beat note over time. For that, the beat note is connected to a frequency counter. As our counter takes only frequencies up

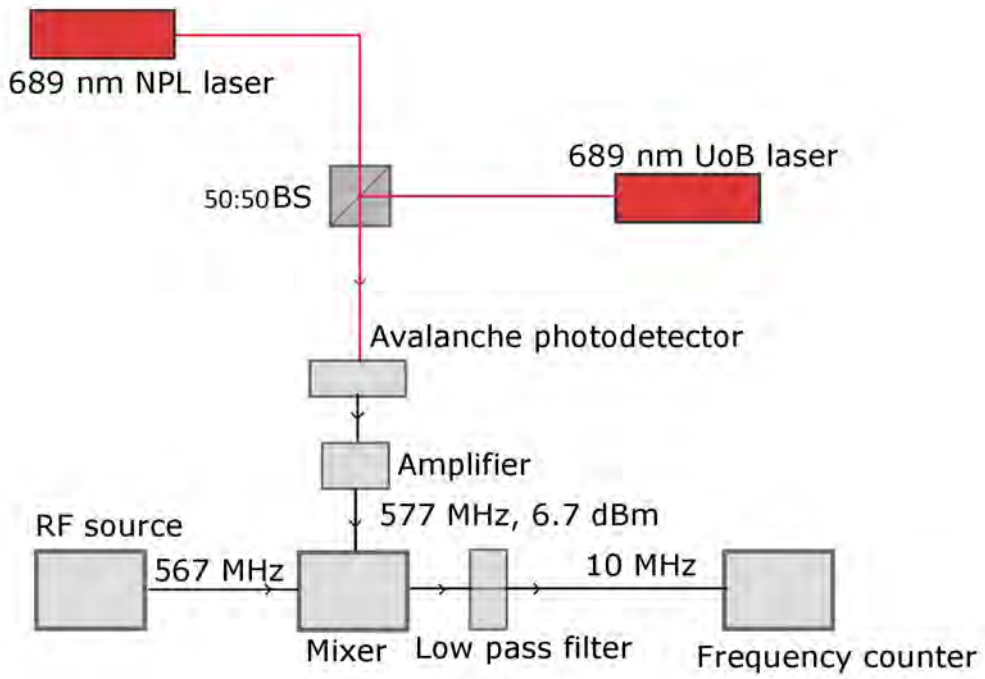

Figure 4.18: Schematic of the set-up used for frequency down-conversion.

to 40 MHz, we have down-converted the 577 MHz to 10 MHz frequency using a combination of photodetector, signal amplifier, mixer, filter, and RF source. The scheme is shown in Figure 4.18. A 6.7 dBm signal is sent to the frequency counter and the data is measured. Fractional frequency deviation of the data is plotted to understand the drift of the reference cavity which is kept outside vacuum. The graph is shown in Figure 4.19. At 1 s, the fractional frequency instability is 2.2×10^{-10}. The cavity is stable for several seconds initially, after that it is drifting. It has drifted 377 kHz in 1000 s. This drift rate is not ideal for a second stage cooling laser. The reasons for the large drift could be that the optical reference cavity is in air instead of being in vacuum, and it is not kept at the zero CTE which led to material expansion resulting from temperature fluctuations. Therefore, in order to improve the results, we decided to set up a cavity inside a vacuum chamber as the vacuum will significantly reduce the changes in temperature and refractive index.

4.9 Characterisation of the cavity inside vacuum

A second cavity is housed inside a vacuum chamber. The cavity is kept in a vacuum level of 2×10^{-7} mbar. The experiments are performed using homebuilt 689 nm laser (the same as described in section 3.2), a commercial 689 nm laser, NPL's 689 nm laser, and the 698 nm clock laser. The first part here is describing the characterisation of the cavity using the homebuilt

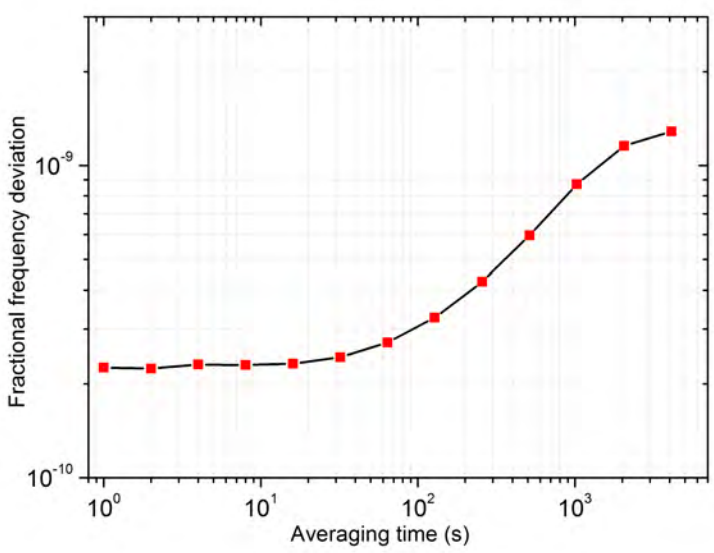

Figure 4.19: Fractional frequency deviation of the FP cavity outside vacuum. It is measured by monitoring the change in beat note frequency.

689 nm laser and NPL 689 nm laser. When we took measurements with homebuilt laser and NPL laser, the cavity was still kept at 20.7°C. The laser is locked to the cavity inside vacuum using a PDH lock on the dual modulation sideband. The beat note between the test laser and the NPL 689 nm laser is obtained and monitored using a frequency counter as described in section 4.8. With the cavity inside the vacuum chamber, the results improved across all time scales. At 1 s time scale, the fractional frequency instability is 1.7×10^{-10}. The short term drift rate also shows an improvement, as the cavity remains stable for initial 20 seconds and then starts drifting. We also see a reduction in the drift rate, at 1000 s the frequency instability is 2.4×10^{-10}. Fractional frequency deviation of the cavity drift measurement is shown in Figure 4.20.

The frequency stabilisation unit (FSU) consists of another (third) optical reference cavity that has been assembled. The FSU characterisation is performed mainly with a commercial diode laser at 689 nm (TA Pro, Toptica) and a homebuilt ultra-stable clock laser. The cavity is placed under vacuum, and at zero CTE for the measurements described from here onwards. First, we'll discuss the drift measurement for the cavity using a clock laser, and then using the commercial diode laser. The clock laser with a linewidth less than 1 Hz [118] is locked to an ultra-stable cavity. A second output is sent through an EOM, which is driven by a function generator, and is coupled to the cavity being tested. The modulation frequency of the EOM is tuned so as to adjust the sideband frequency to match with the cavity reference frequency (TEM_{00} mode). The cavity transmission peak is monitored on the oscilloscope and the data are recorded for 15-20 minutes to study the

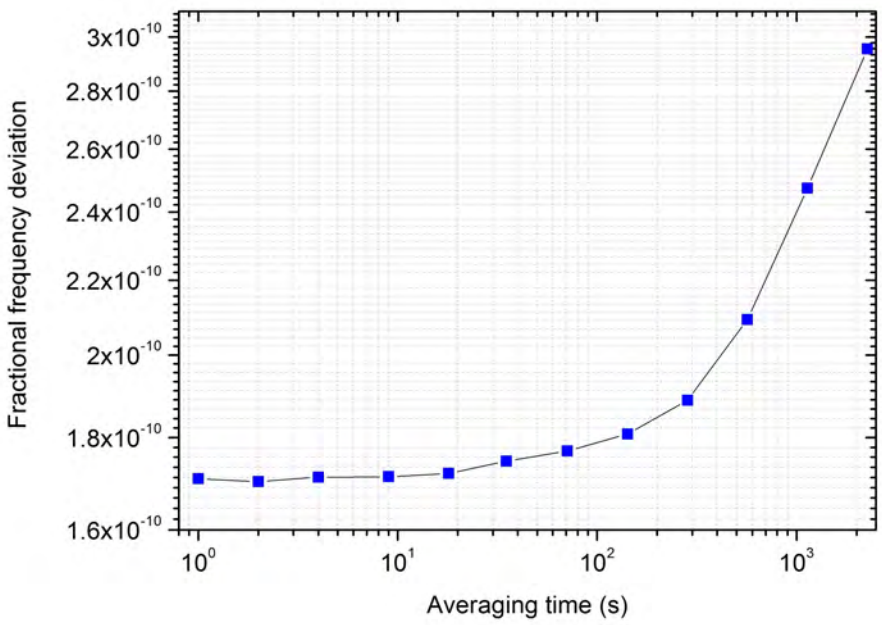

Figure 4.20: Stability plot for the cavity inside vacuum. The homebuilt 689 nm laser is used for obtaining the measurement.

cavity drift. The data is plotted to find the cavity drift using the stabilised clock laser as shown in Figure 4.21. A linear fit to the data gives a drift rate of 60 Hz/s. This is a lower drift rate compared to what is shown in Figures 4.19 and 4.20.

Next, the characterisation is performed using a commercial laser at 689 nm. Here, we also employ an optical frequency comb for the measurements. The scheme is shown in Figure 4.22. The comb is locked to the ultra-stable clock laser and attains a linewidth of 1 Hz. Section 1.6 describes how an optical frequency comb works. A beat note is obtained between the 689 nm laser module of the comb and the commercial 689 nm laser which is locked to the FP cavity. The linewidth is obtained using a spectrum analyser. Based on the linewidth observed, the PID gains of the 689 nm laser are adjusted to obtain as low a beat linewidth as possible. The laser linewidth is reduced to 1.15 kHz at a measurement time of 1 s, see Figure 4.23. The fractional frequency instability of the laser at 1 s is 2.5×10^{-12}. The cavity drift is obtained by measuring the beat note frequency between the comb, and the 689 nm laser employing a K+K FXE frequency counter. For couple of seconds initially, the cavity is stable and after that it has linear drift, see Figure 4.24. We measured a drift rate of 70 Hz/s, which is close to the drift rate measured by scanning the clock laser across the FP cavity. At a measurement time of 1000 s, the fractional frequency instability is 1×10^{-9}. In the FSU system, the 689 nm commercial laser has a lock bandwidth of 600 kHz, whereas, 813 nm laser has 550 kHz, and 679 nm laser has 489 kHz lock

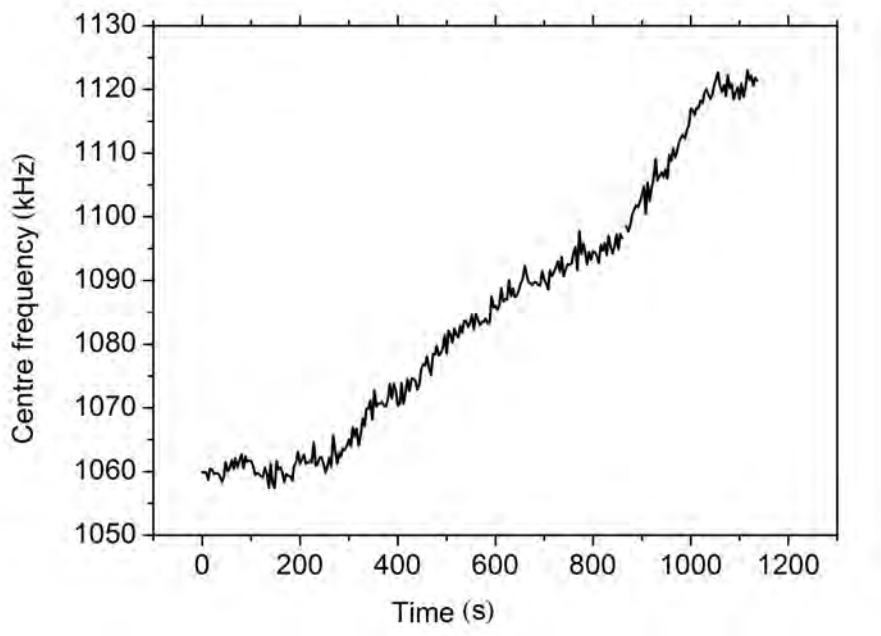

Figure 4.21: Frequency drift of the reference cavity used in FSU measured by scanning the 698 nm clock laser through the cavity.

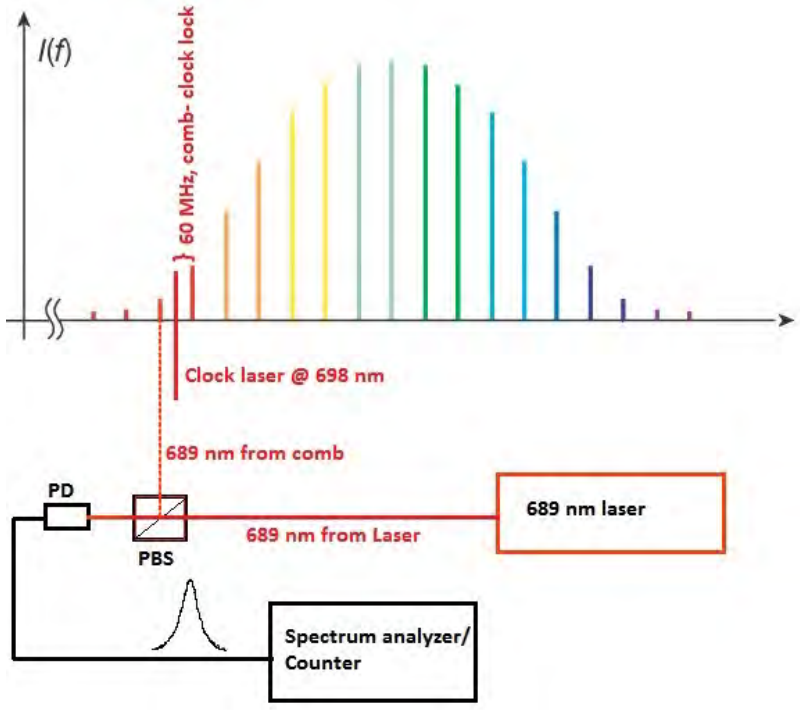

Figure 4.22: Schematic diagram describing the frequency comb-689nm laser beat note set-up.

bandwidth. These bandwidths are determined by the locking parameters and the feedback servo loops.

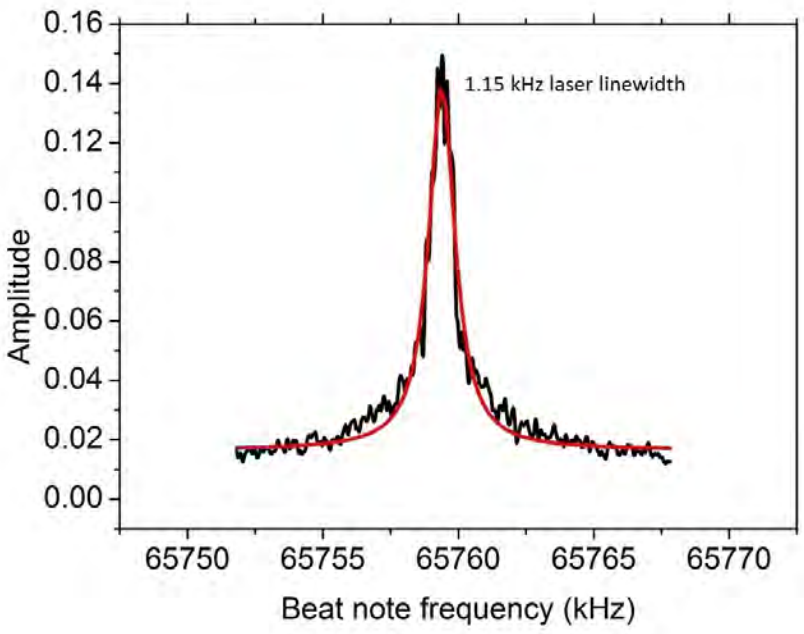

Figure 4.23: Linewidth of cavity stabilised 689 nm commercial diode laser.

We have studied the frequency stability of the 30 mm optical reference cavity under three different environments: outside vacuum and not at zero CTE, inside vacuum and not at zero CTE, and inside vacuum and at zero CTE. From all the three cases, it comes out that the cavity which is inside vacuum and placed at zero CTE (which is used in the FSU) gives the best results. It has a frequency stability of 1.15 kHz at 1 s measurement time. Temperature stability of our optical reference cavity is one of the reasons for the linear drift experienced by the cavity. We will discuss the temperature measurements in the next section. In our FSU system, the results obtained by characterisation with clock laser and commercial 689 nm diode laser locked to a frequency comb are almost similar and consistent, considering that we are using the cavity to lock 689 nm, 813 nm, and 679 nm lasers. FSU is good enough to obtain a broadband red MOT with its current short term stability. In order for it to be used effectively for a narrowband red MOT, we need to improve the long term stability. A more effective temperature stabilisation is the first task to minimise the linear drift. We have not yet tried to achieve a red MOT with the FSU.

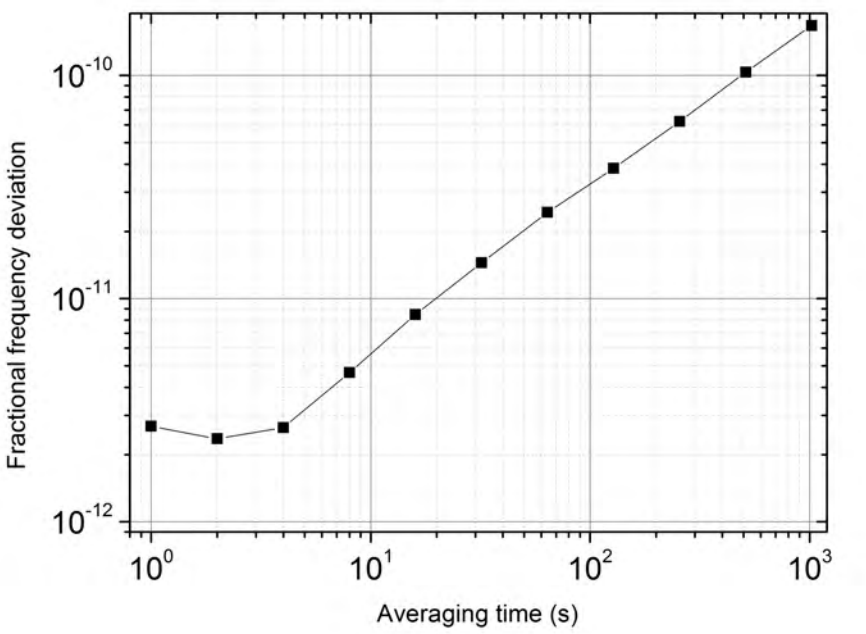

Figure 4.24: Frequency drift of the reference cavity used in FSU obtained by monitoring the beat note between the 689 nm diode laser locked to the cavity and the comb stabilised to the clock laser.

4.10 Cavity temperature drift measurements

Temperature stabilisation plays a major role in controlling the frequency drift of a reference cavity. A single layer of temperature stabilisation is installed on the cavity inside the vacuum chamber. A peltier element is used to heat or cool the cavity housing to the desired temperature. The 689 nm laser should have a thermal stability that can keep its frequency instability to below a few kHz per day. Ideally, it is the best to have a reference cavity with a thermal stability of the order of 1 mK per hour as per the calculations performed based on the frequency stability measurements shown in Figures 4.21 and 4.24.

The data plotted in Figure 4.25 is measured when a Thorlabs temperature controller (TTC001) is used for the temperature stabilisation of the cavity inside the vacuum chamber. It is understood from the graph that there is a temperature fluctuation of approximately 5.8 mK/hour. Combining this with the zero CTE measurement data described in section 4.6, corresponding frequency drift is calculated as 1.88 kHz/hour.

We also used a temperature controller from Toptica (DTC 110) to stabilise the cavity temperature inside the vacuum chamber. The result is plotted in Figure 4.26. The maximum peak to peak temperature fluctuation we obtained after using this controller is approximately 5 mK/hour

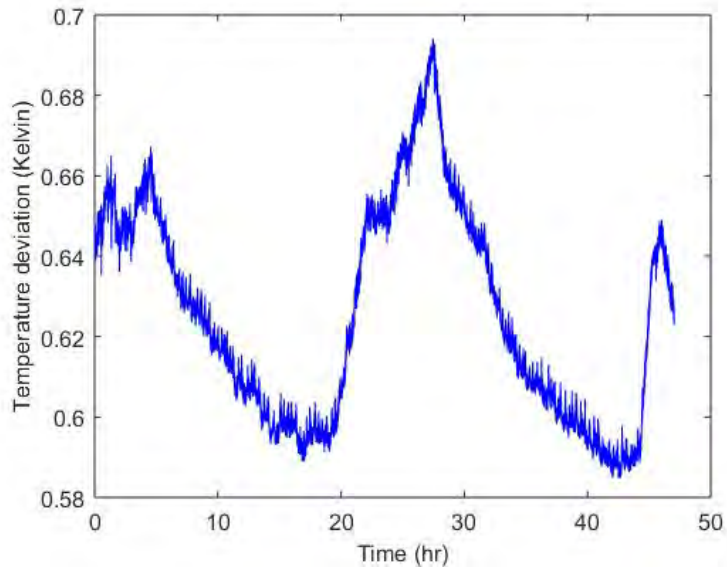

Figure 4.25: Temperature fluctuation measured close to the cavity inside the vacuum chamber. The measurement shows the fluctuations when Thorlabs temperature controller is used to stabilise the temperature inside the cavity.

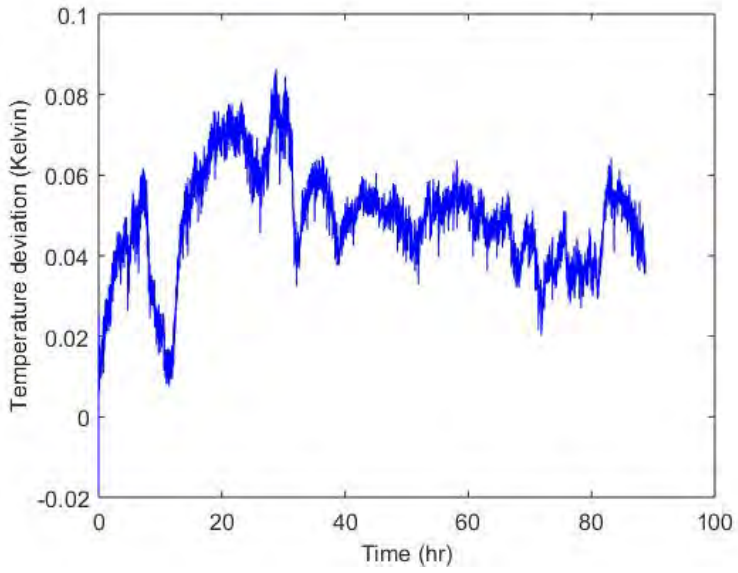

Figure 4.26: Temperature fluctuation measured close to the cavity inside vacuum chamber. The measurement shows the fluctuations when Toptica temperature controller is used to stabilise the temperature inside the cavity.

with a maximum deviation of 70 mK over the 90 hour period. It introduces a frequency drift of 1.6 kHz/hour. Due to the difference between the measurements using Thorlabs and Toptica temperature controllers, we decided to use Toptica temperature controller for the cavity. However, these results are not ideal for obtaining an ultra-stable laser with a long term stability of 1 kHz/day. Instead of single layer thermal stabilisation, a double or multilayer thermal stabilisation is better to obtain an ultra-stable temperature inside the cavity. Therefore, a new chamber is designed as described, in section 4.11.

4.11 A modified vacuum chamber for the cavity

A new vacuum chamber is designed to improve the thermal stability of the cavity. Unlike the previous vacuum chamber, this one has dual layer thermal stabilisation. In order to implement the dual thermal stabilisation system, the design of the chamber is slightly modified. There are two aluminium layers and one titanium layer around the cavity as shown in Figure 4.27. There are peltiers between the first and the second aluminium layer, and between the second aluminium layer and the titanium layer. Each peltier is accompanied by a 10 kΩ thermistor for the PID servo loop and two extra thermistors for logging the thermal stability over time.

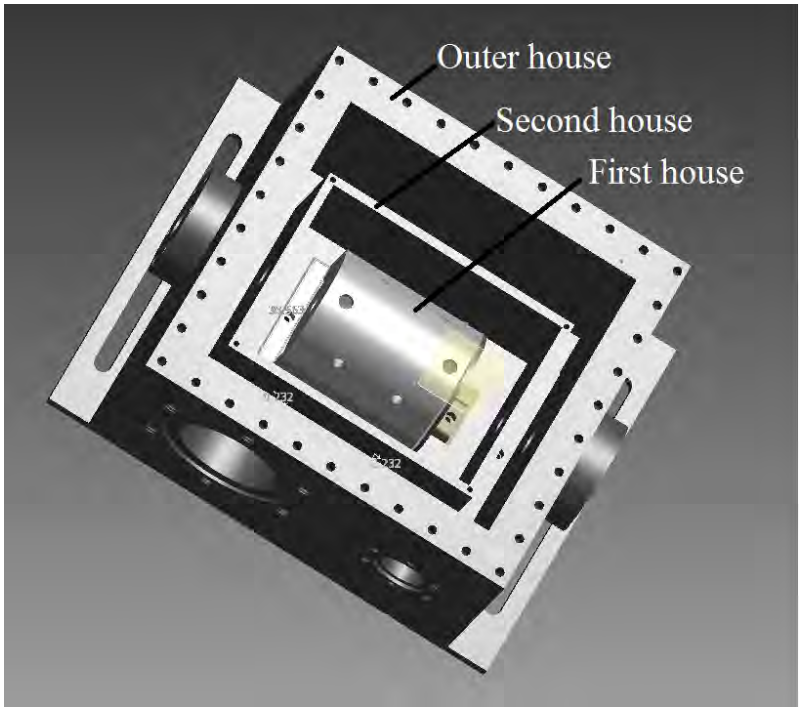

Figure 4.27: Modified vacuum chamber design with dual layer thermal stabilisation of the reference cavity.

The two inner houses are sealed using screws while the outer one is sealed using indium. The

windows are also sealed to the chamber using indium. The DN16CF and DN35CF ports use copper gasket for sealing. We use a DN35CF port for the vacuum feedthrough instead of a DN16CF port due to the larger number of pins we required for the two peltier elements and the four 10 kΩ thermistors. Even though there is a mismatch in thermal conductivity between aluminium and titanium, the later one is chosen as the outer layer as it is harder than aluminium and as it allows to implement gasket sealing. We employ a 3 l/s ion pump on the new chamber because a shot to shot pressure monitoring is possible with this ion pump whereas with the CapaciTorr pump it is not possible.

We have locked a laser with the cavity inside the new vacuum chamber. However, we have not performed any frequency stability measurements so far.

4.12 A lab-based frequency reference cavity

The FP cavity shown in Figure 4.28 is designed by adopting idea from S. A. Webster and team [104]. We have a similar cavity which is being employed to stabilise one of the clock lasers in our lab [134]. The new cavity discussed here is intended for stabilising the 689 nm laser for the second stage cooling of strontium. The spacer is manufactured from ULE and the mirrors are made from fused silica. There is one planar mirror and one concave mirror with a radius of curvature of 1000 mm, both have a diameter of 25 mm. We have chosen a 1000 mm radius of curvature to increase the spot size of the beam. This configuration will minimise the average power per unit area, which in turn will reduce the random noise (Brownian thermal noise), which can be described using an equation [135]:

$$S(f) = \frac{2k_B T}{\pi f} \frac{1-\sigma^2}{\sqrt{2\pi} E \omega_0} \Phi_{sub}(f), \tag{4.16}$$

where *S(f)* is the spectral density of the random noise, $\Phi_{sub}(f)$ is the mechanical loss of the mirror substrate, ω_0 is the beam waist of the laser at the point where the intensity is $1/e$ times the maximum intensity, and σ and E are the Poison's ratio and Young's modulus, respectively, for the material used as mirror substrate.

The mirror reflectivity of 99.994% at 689 nm results in a finesse of 52,385. The cavity free spectral range is 1.499 GHz and its linewidth at 689 nm is 28.63 kHz. The spacer has a diameter of 50 mm and a length of 100 mm. This cavity is meant to achieve vibration insensitivity which usually arises due to the change in distance between the mirror centres. This goal is achieved by mounting the cavity symmetrically so that no deformations occur between the separation of the mirrors. For that, support points are designed between the cavity and the inner layer of the chamber. The position of the support point is determined from the simulations performed by Steven Johnson in his PhD thesis [134]. When the cavity rests on these four support points, the

distance between the mirrors remains unchanged.

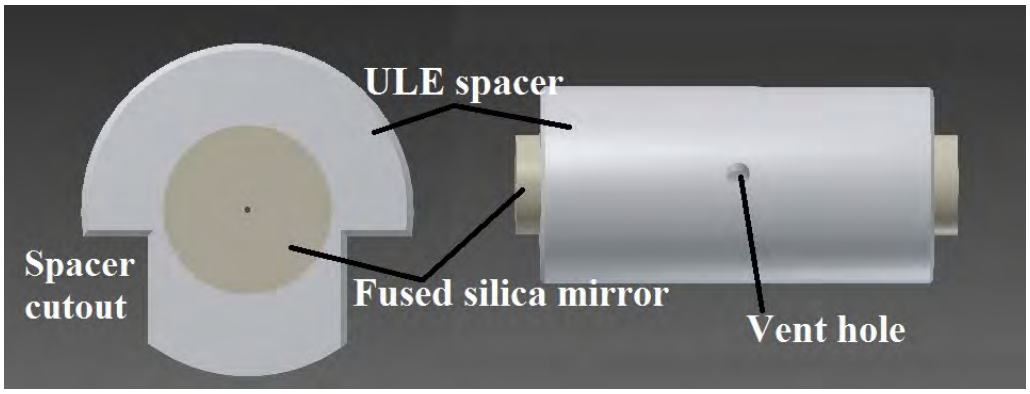

Figure 4.28: 10 cm optical reference cavity for stabilising 689 nm laser.

Acceleration sensitivity of a cavity leads to frequency instability during 0.1 to 10 seconds of averaging time [104]. One way to reduce the sensitivity is to align the cavity axis parallel to gravity. Another way is to align the cavity horizontally on specific support points as mentioned before. It has been observed that by using 'spacer cutouts' cavity configuration, the acceleration sensitivity can be further reduced to 0.1 kHz/ms^{-2} [104]. In this configuration, a portion of spacer material is removed from the bottom part of the cavity. Vertical forces are compensated by the spacer cutouts whereas the support points determine the vibration sensitivity in the horizontal axis.

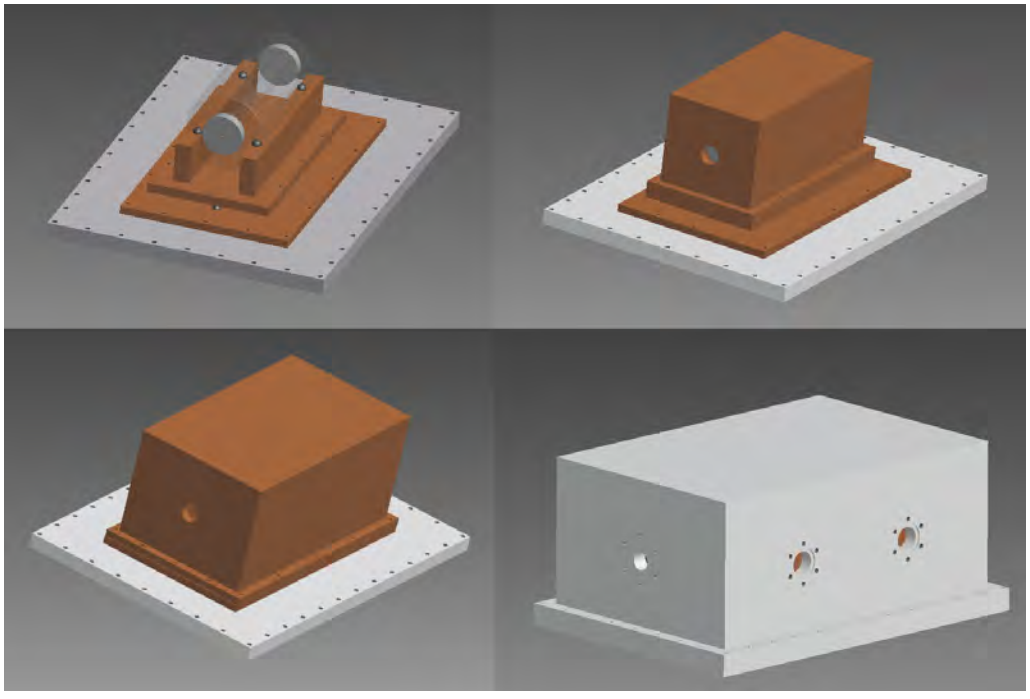

Figure 4.29: CAD design of the vacuum chamber for the cavity.

Figure 4.29 shows the CAD diagrams of the cavity housing. It has a three layer housing.

The inner and middle layer will be made of gold plated copper. The outer layer will be made of space qualified aluminium. Copper has higher thermal conductivity compared to aluminium, thus ensuring a uniform heating and better thermal shielding of the cavity. The thermal control will be realised by a peltier element and 10 kΩ thermistor placed between the middle layer and outer layer.

The inner copper layer has two rectangular blocks with a hemisphere hollow space where the cavity support points can rest. The inner and middle copper layers are also separated by support points. Glass balls with 6 mm diameter are going to be used as support points. The chamber design follows an upside down configuration as seen in Figure 4.29. The cavity rests on the base platforms and is closed from the top using box lids. This design ensures that there is no unwanted movement of the cavity on the support points while setting up the apparatus. Anti-reflection coated wedged windows are being planned to seal the vacuum chamber using indium sealing. The box lid will also be indium sealed for maintaining vacuum. The two DN16CF ports on the side of the outer layer are for a feedthrough for temperature control, and for a valve and 3 l/s ion pump.

In this chapter, first we discussed the details of 30 mm optical reference cavity and its characterisation results. Experiments and measurements using the cavities were carried out at UoB lab and NPL lab. The frequency stabilisation unit (FSU) was developed and tested in UoB, whereas a second cavity which is kept under vacuum is set-up to lock the homebuilt 689 nm laser at NPL. A third cavity, which is kept in air, is developed and used to obtain the first broadband red MOT at UoB, and then transported to NPL for its characterisation with NPL's narrow linewidth 689 nm laser.

The FSU cavity resulted in a frequency stability of 1.15 kHz at 1 s measurement time, making it as the best among the other cavities to be used for second stage cooling of strontium. In FSU, we have currently locked three different laser wavelengths which are required for the cooling and trapping of strontium. The temperature stability of the cavity has to be improved to get a better long term frequency stability. This can be achieved by improving the thermal stabilisation by implementing multi-layer thermal stabilisation. We also discussed the details of a new 10 cm cavity which will be used for stabilising a 689 nm laser which is to be used for a lab based experiment. In the next chapter, we will discuss the progress of SOC2 project.

Chapter 5

Clock transition spectroscopy in 1D optical lattices

This chapter contains a section of work that I performed related to Space Optical lattice Clock (SOC2), which is a European project (Project number: 263500) with universities, research laboratories, and industries for building a space optical lattice clock prototype. The goals of the project are to test and study fundamental physics, geodesy applications, establish clock comparisons etc... Atomics package development and system assembling were provided by the University of Birmingham, later, the developed set-up was transported to Physikalisch-Technische Bundesanstalt (PTB), Germany for further experiments. PTB, University of Birmingham, and Heinrich-Heine University of Düsseldorf (HHUD) were involved in the clock transition spectroscopy in the SOC2 system, and I joined the project at PTB as a representative of University of Birmingham and was involved in the clock spectroscopy measurements and characterisation of the SOC2 system. It is also the project undertaken as a secondment within the EU ITN Project- FACT (id: 607493) in which I was involved.

5.1 The Space Optical lattice Clock (SOC2) system

The SOC2 is a transportable strontium optical lattice clock system which consists of a vacuum chamber, modular laser systems, a frequency stabilisation system which contains three optical reference cavities, a Zeeman slower, and electronic components. It aims at an accuracy better than 1×10^{-17}, and a fractional frequency instability of less than 1×10^{-15} measured at 1 s. Prior to the SOC2 project, the SOC1 project developed an optical lattice clock with an accuracy of 7×10^{-15} [48]. SOC2 system is more compact and aiming at improved results.

Figure 5.1 shows a CAD drawing of the SOC2 advanced atomics package. It consists of an

oven which is the strontium source. As the vapour pressure of strontium is low, the oven is heated up to 350-400°C so that the strontium atoms gain a sufficient velocity (400-450 m/s) to reach the science chamber. The system operates under vacuum in order to avoid any background gas collisions affecting the MOT and the clock transition signals. There is a 25 l/s ion pump installed after the oven which maintains a vacuum level of 2×10^{-9} mbar. A combination of a linearly polarised, counter-propagating laser beam, and a permanent magnet Zeeman slower which is built by a research team at NPL [115] are used to slow down the velocity of the atoms by the generation of a tapered magnetic field, from reaching the science chamber. The atomic beam reaching the science chamber after travelling through the Zeeman slower region is further cooled down by the MOT laser beams aligned with the centre of the chamber from three directions. The 461 nm laser for first stage cooling and the 689 nm laser for second stage cooling (both laser beams have a diameter of 10 mm) are overlapped using dichroic mirrors which are mounted on the cage system outside the science chamber. Both lasers are circularly polarised after passing through the quarter wave plates mounted between the fibre output and the dichroic mirror.

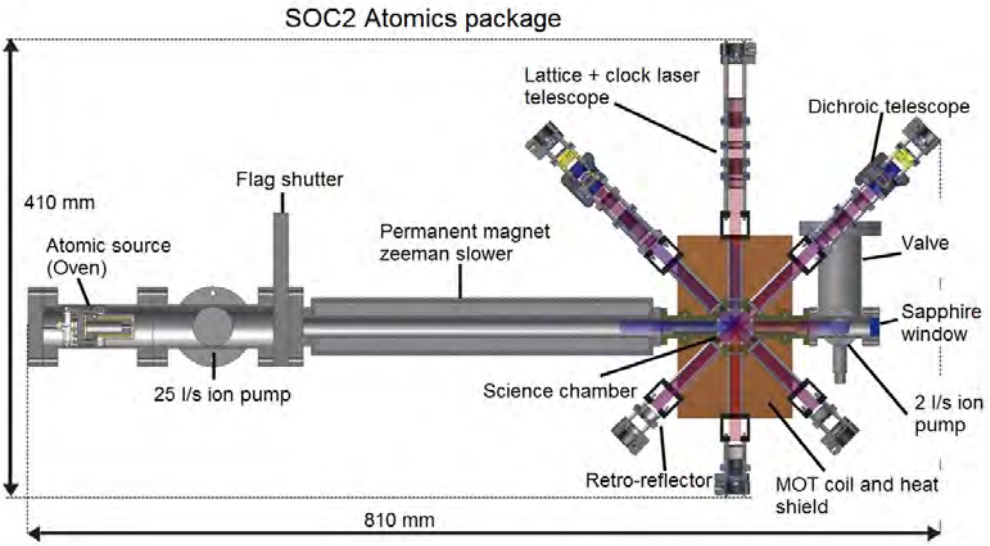

Figure 5.1: CAD design of the SOC2 atomics package [7].

The three axes for the MOT beams are: one perpendicular to the plane of the image and the other two are shown as two diagonal cage systems. All the three axes are at an angle of 90° with respect to each other. In order to form a six-way MOT beam configuration, each beam is retro-reflected from the far end of the cage system. The science chamber contains viewports to accept the atomic and laser beams into the chamber, detect the MOT using a camera and a photomultiplier tube, and allow the Zeeman slowing beam to reach the chamber. The viewport through which the Zeeman slower beam propagates is heated up to 150°C to eject any strontium that has been

deposited on the window, otherwise the transmitted Zeeman slower laser beam power reaching the MOT is reduced. Anti-Helmholtz magnetic field coils are mounted on both sides of the science chamber. These coils are used to generate a position dependent force to cool the atoms. The coils generate a large amount of heat due to the high currents passing through them. Therefore, in order to remove the heat out of the system, heat sinks are mounted over the magnetic field generation coils. There is another ion pump (3 l/s) mounted after the science chamber which maintains the vacuum level at the order of 1×10^{-10} mbar, which is an order less than that at the oven region. A detailed description and discussion of the atomics package for SOC2 can be found in Lyndsie Smith's PhD thesis [114]. The author also explains elaborately the results obtained after characterising the blue and red MOTs which are the steps before achieving the clock transition in a strontium optical lattice clock.

5.1.1 Laser systems

Most of the laser systems employed in the SOC2 project are commercially available. For the first stage cooling, a frequency doubled SHG-pro laser from Toptica is employed. The 922 nm laser, which is locked to a frequency doubling cavity, generates 461 nm laser beam. A fibre coupled output of 400 mW from the 461 nm laser is sent and divided into different branches in a laser beam distribution module which is composed of mirrors, wave plates, polarising beam splitters, and AOMs. From this module, three MOT beams, a probe beam, and a Zeeman slower beam are employed for operating the strontium optical lattice clock system.

Repumper lasers at 707 nm and 679 nm are based on DL-pro Toptica laser heads. They are not locked to any frequency reference due to their passive stability. They have a free running linewidth 1 MHz, which is sufficient for repumping strontium atoms.

The second stage cooling utilises a master-slave diode laser at 689 nm wavelength. The master laser is a diode laser from Toptica which gives an output power of 15 mW and a laser linewidth of 800 kHz. The linewidth is further narrowed by locking this laser to an optical reference cavity. An output of 1 mW from the master laser is used to inject a slave diode which has an output power of 30 mW and a 1 MHz free running linewidth. After injection locking the slave laser with the master laser, the linewidth of the slave laser is narrowed down to 1 kHz. The output of the slave laser is coupled to a 1×3 fibre splitter (Evanescent optics) and sent to the 3D MOT chamber. The 689 nm and 461 nm laser beams are combined using dichroic mirrors on the cage system to send to the 3D MOT chamber.

The 813 nm lattice laser head is a TA-pro also from Toptica. The laser gives 2 W output power after the tapered amplifier (TA). Due to its passive linewidth of 1 MHz, it is not locked to any reference frequency. However, if required, it can be locked to an optical reference cavity in the

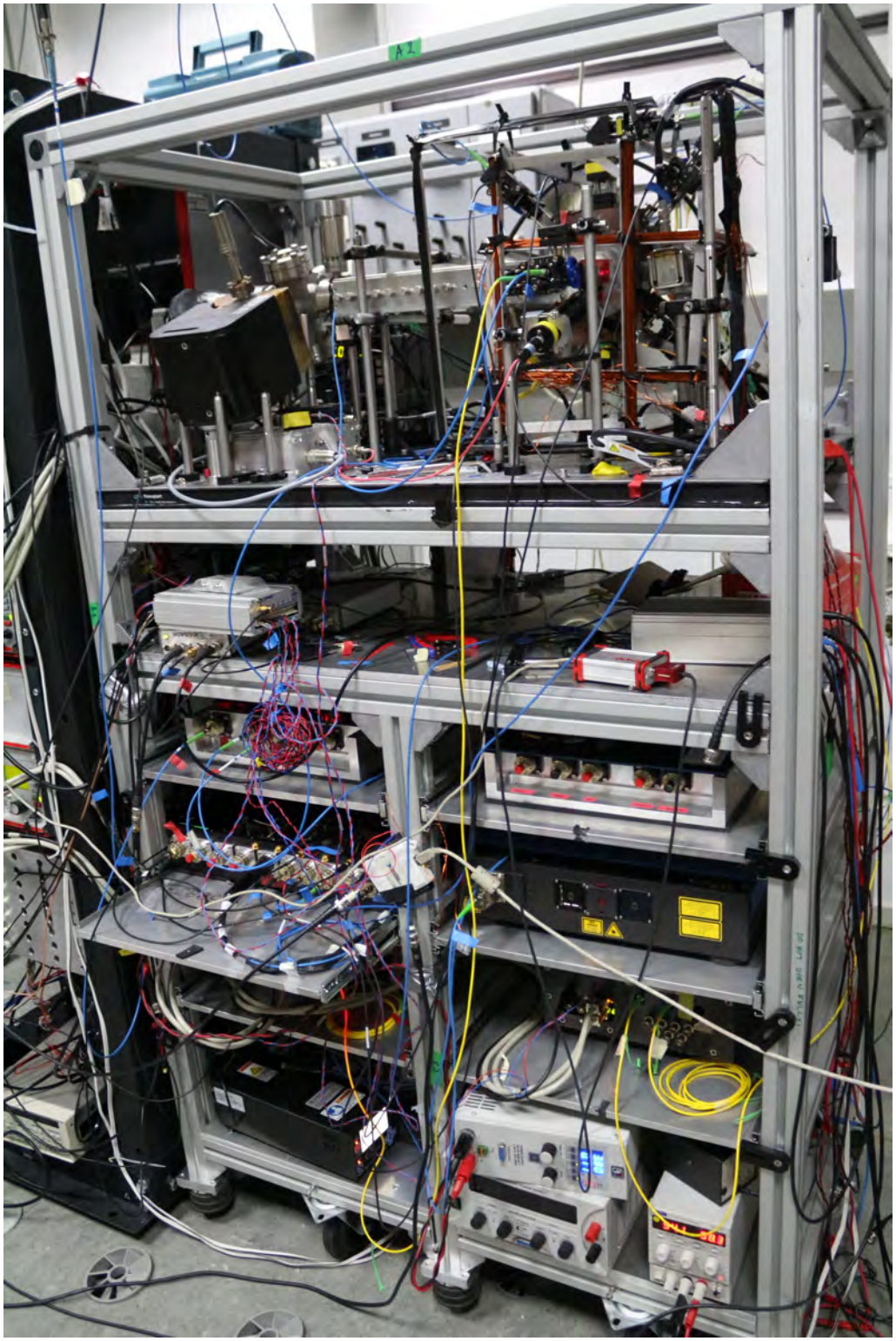

Figure 5.2: SOC2 system mounted on the rack.

frequency stabilisation system. When compiling the uncertainty budget, it will be required to lock the lattice laser for a better frequency stability.

A frequency stabilisation system (FSS) developed by S. Schiller and team at Heinrich Heine University Düsseldorf (HHUD) is used to stabilise the lasers for the SOC2 system. It contains three 10 cm ULE cavities kept under vacuum. The cavity can be used to lock the 922 nm, 689 nm, and 813 nm lasers. For the 922 nm laser, a Digilock from Toptica is employed as a PID controller for locking to the cavity. The 689 nm laser has got homebuilt PID controller electronics from the University of Hannover. A PDH locking scheme is used for laser frequency stabilisation. More information about the cavity, locking, and laser characterisations can be found in [98]. The atomic package and laser systems (except the clock laser and its cavity) are mounted on a rack as can be seen from Figure 5.2.

The clock laser at 698 nm is another important laser for strontium optical lattice clocks. The laser, built at the Leibniz Universität Hannover (LUH), is stabilised to an ultra-stable optical reference cavity built by SYRTE. The final integration of the laser and the cavity is accomplished at PTB. Section 5.2 explains the clock laser and the cavity in detail.

5.2 The clock laser for spectroscopy

The clock laser is an ECDL stabilised by interference filter. The laser head contains a laser diode, an aspheric lens to collimate the beam from the diode, another aspheric lens to focus the beam on the mirror that is glued onto the PZT, and an interference filter mounted on a rotation mount for wavelength selection. The output of the laser from the ECDL is coupled into a fibre and distributed into different branches in the clock laser distribution module. The distribution module has four outputs. The first output goes through an AOM to the atomics package for the clock transition interrogation; the second output beam after double passing through an AOM and then an EOM, goes to the reference cavity for frequency stabilisation; the third output goes to an ultra-stable clock laser which is locked to the 'beast' cavity at PTB for beat note comparisons, and the fourth one goes to the wavemeter for monitoring the frequency of the laser. Figure 5.3 shows a photograph of the clock laser and its distribution module.

Out of the total 15 mW of output power, a maximum 1 mW of power is available to interrogate the atoms, 20 μW is used to lock the laser to the cavity, and 1 mW for beat note measurements. The laser has a free running linewidth of 10 kHz. It is temperature stabilised using a peltier element.

The laser is locked to an ultra-stable cavity called 'SOC2 cavity'. The cavity spacer with 100 mm length and 110 mm diameter is made of ULE and mirrors are composed of fused silica

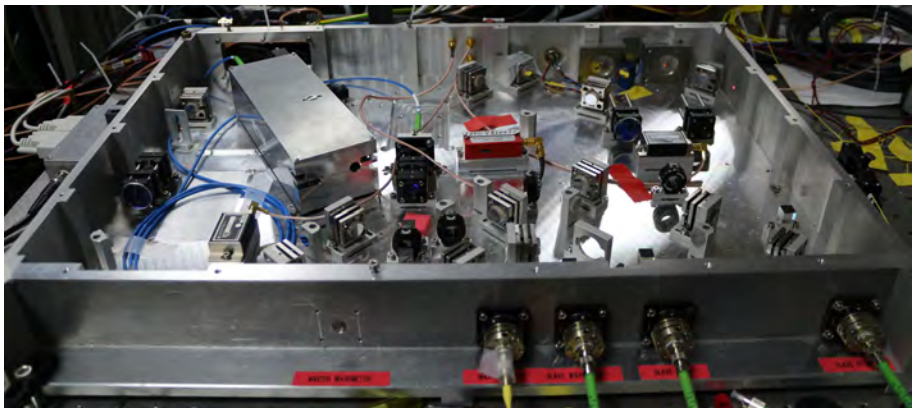

Figure 5.3: Photograph of the clock laser and its distribution module.

substrate. One of the mirrors is flat and the other one is curved with a radius of curvature of 1m. The coefficient of thermal expansion (CTE) of fused silica is higher than ULE, and therefore to compensate for the CTE mismatch, ULE annulus ring is optically bonded to the rear of each mirror [121]. The cavity is embedded in three layers of gold plated aluminium shielding to avoid temperature fluctuation. The gold plating reduces emissivity of the metal surface. The chamber is kept under a vacuum of 1×10^{-7} mbar using a 3 l/s ion pump. The cavity is mounted vertically to effectively reduce its sensitivity to seismic noise [120]. More information about the clock laser and the optical reference cavity can be found in [8]. Figure 5.4 is a photograph of the vacuum chamber in which the cavity is mounted.

The laser is locked to the TEM_{00} mode of the cavity using Pound-Drever-Hall locking technique. Figure 5.5 shows the schematic diagram of clock laser frequency stabilisation. The laser is locked to the SOC2 cavity, then phase locked to the 'beast', and to the strontium atoms. Any drift in the laser frequency occurring due to the SOC2 cavity is compensated by the feedback (drift correction) given to AOM 1 from the atoms and the ultra-stable laser.

5.3 Towards measuring the clock transition

There are a series of steps before interrogating the clock transition. There was an air conditioning drop when I joined PTB for the SOC2 project. Therefore we had to re-establish the system in working condition. The laser systems and atomics package are realigned completely. Then, the first step we had to do towards reaching a clock interrogation stage was to obtain the blue MOT.

5.3.1 Cooling the atoms

A blue MOT with 1×10^7 atoms is obtained by using 18 mW of the total MOT beam power in the three beams, 60 mW power in the Zeeman slower beam, 3 mW and 2 mW in the 707 nm and

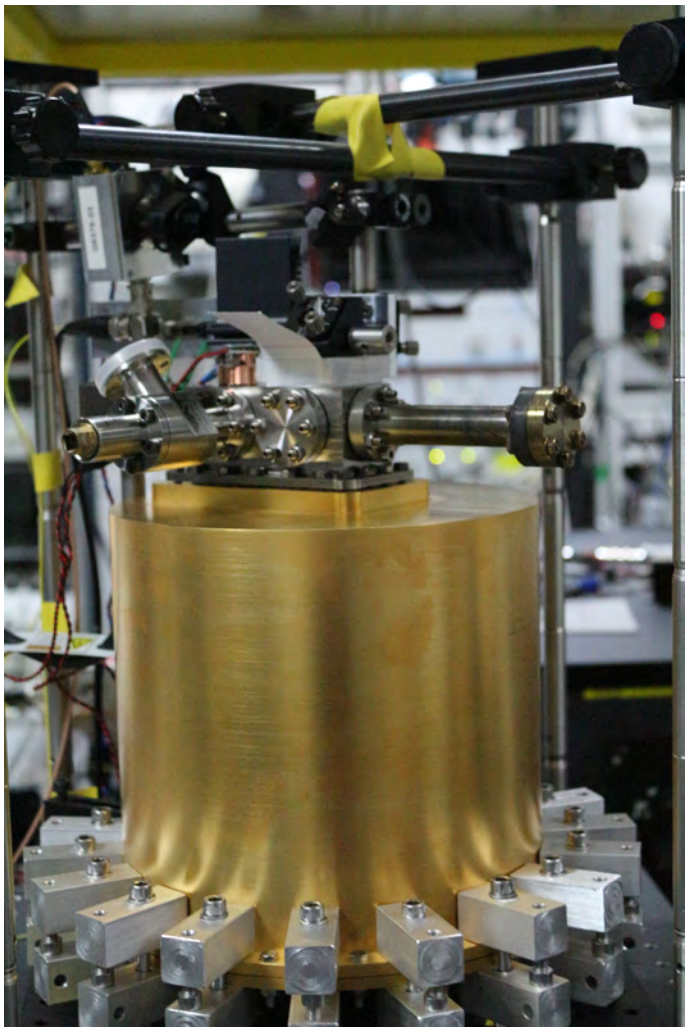

Figure 5.4: Photograph of the SOC2 clock cavity vacuum chamber. Cavity is designed and built by SYRTE, Paris [8].

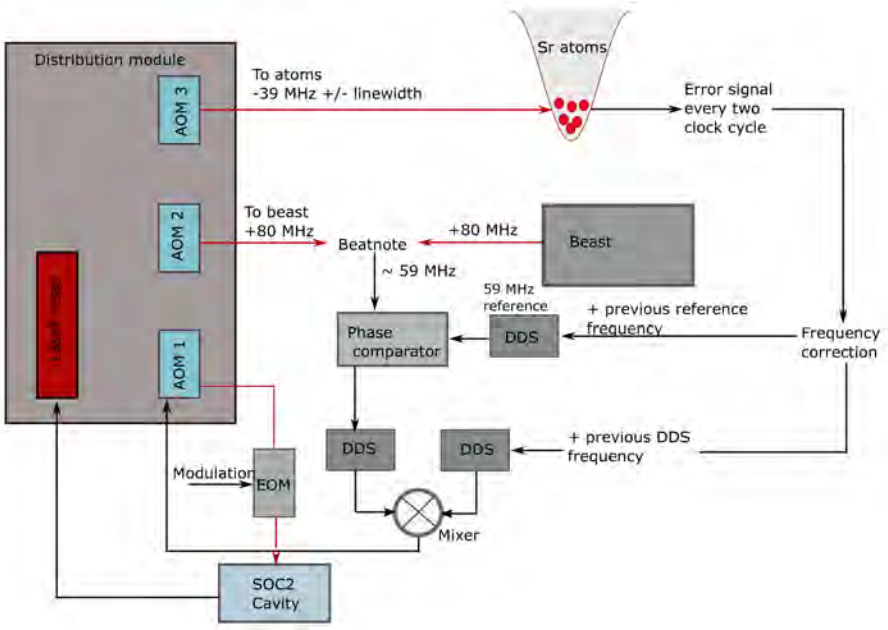

Figure 5.5: Clock laser stabilisation scheme. The laser is locked to SOC2 cavity, 'beast', and strontium atoms.

679 nm repumper lasers, respectively. The MOT beams and slower beam are detuned by -24 MHz and -167 MHz, respectively, and the magnetic field gradient is 45 G/cm. The atoms are loaded into the blue MOT for 300 ms. A detection beam at 461 nm is used to detect the atoms in MOT. The obtained MOT has a diameter of 1.2 mm. Temperature of the atoms in the blue MOT is 3 mK. It is measured employing time of flight measurements. This method involves switching off the beams for a certain amount of time and MOT images are captured. This process is repeated for a couple of times with different switching off times. The temperature of the cold atoms can be obtained by plotting the size of the MOT and corresponding laser beam switching off times. The blue MOT is optimised by tuning the frequencies of the MOT beams, slower beams, and repumper beams. While varying the frequencies, the variation in the atom number is monitored and the frequencies are fixed to the configuration which gives the maximum number of atoms in the MOT. After 300 ms loading time, the blue laser power and the magnetic field is ramped down to 0.14 mW in 30 ms and 35.2 G/cm, respectively. The blue MOT laser beam power is reduced to minimise the temperature of the atoms in the MOT and the reduction in magnetic field leads to a higher trap volume.

Second stage cooling, otherwise known as Red MOT, is the next stage. The red MOT laser beams with 800 kHz detuning, which are overlapped with the blue MOT laser beams are also activated during the blue MOT stage. Blue beams are switched off during the red MOT stage. The magnetic field is turned down to 2 G/cm during the first 15 ms of red MOT stage to ensure

a higher capture volume. A total of 9 mW of 689 nm laser beam is used during the initial stage which is otherwise known as broadband cooling. About 20% of the atoms from the blue MOT is transferred to the red broadband MOT. A narrowband red MOT is then obtained by lowering the power (intensity) of the 689 nm laser beams to 30 μW step by step and gradually increasing the magnetic field to 13 G/cm. Increase in the magnetic field caused reduction in the trap volume, but the trap becomes tighter and hold more atoms with lower temperature. We have measured a temperature of 8 μK in broadband MOT and 5 μK in the narrow band red MOT. Different combinations of power and magnetic field gradient are evaluated to obtain a maximum number of captured atoms at a minimum temperature in the narrow band MOT. 30 μW of power is used for 55 ms to achieve the narrow band MOT which could capture 2×10^5 atoms. The narrow band MOT is obtained by detuning the laser 400 kHz away from the transition. The cooling and clock spectroscopy sequences used in the SOC2 system are illustrated in Figure 5.6.

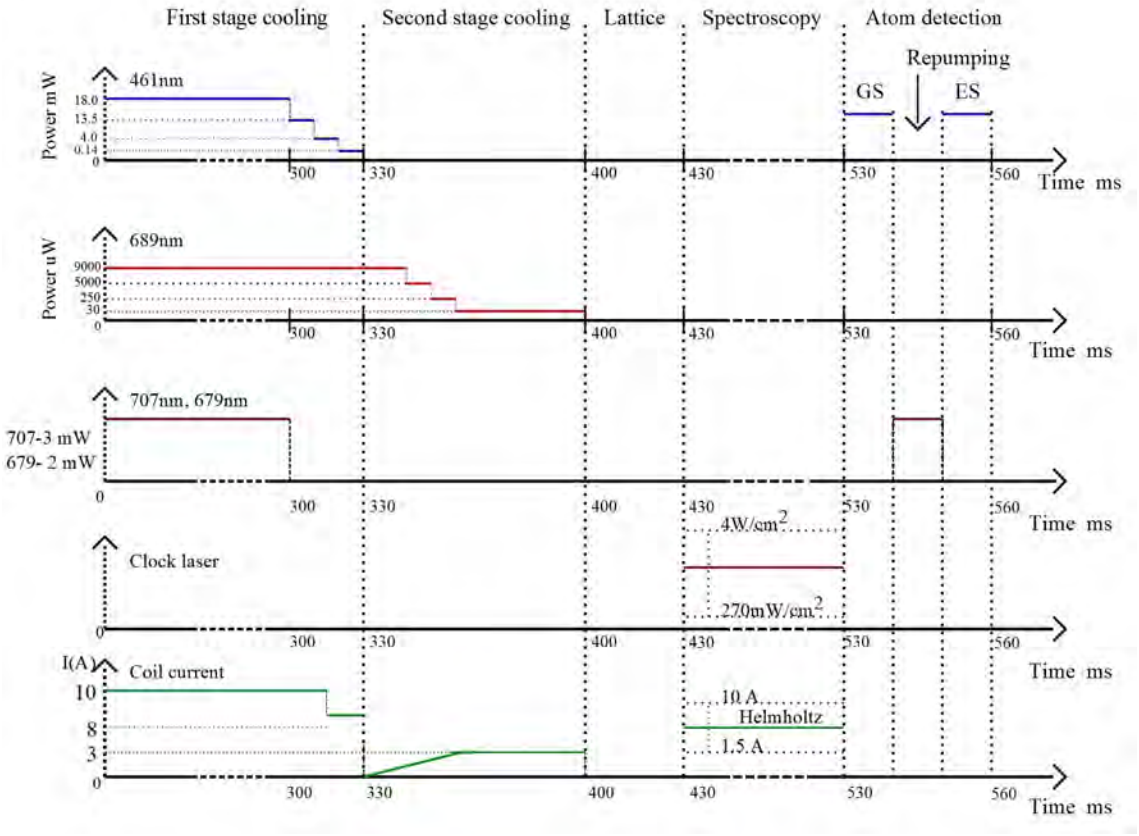

Figure 5.6: Timing sequence for cooling, trapping, and clock transition interrogation in ^{88}Sr.

5.3.2 Trapping the atoms

After the second cooling stage, cold atoms are trapped in an optical lattice formed of retro-reflecting 813 nm laser. The laser is aligned with respect to the vertical direction of the atomic chamber. In order to align the lattice beam, we first used a blue detection beam from the bottom of the chamber onto the red MOT. The beam is aligned using retro-reflective mirrors on the top side of the atomic chamber until the red MOT atom cloud is destroyed due to the detection beam. This effect is typically observed when the detection beam is well aligned with the red MOT. Second, we unplugged the blue beam fibre and connected the lattice beam fibre. The measured lattice beam waist at the centre of the trap is 49±2 μm. A beam profiler (CinCam CMOS-1201-Pico, Cinogy Technologies) is used for the beam waist measurement. The device is placed just outside the vacuum chamber, and measurements are performed at different positions. The dimensions of the chamber and components such as viewport are already known, and with the help of these, the beam waist is estimated at the centre of the trap by fitting the data points obtained. A maximum of 600 mW laser beam power is available for the lattice trap. The lattice laser power is altered by changing the current sent to the tapered amplifier. Less than 10% of atoms from the red narrow band MOT are trapped in the lattice. There are nearly 500 lattice sites and an average of 20 atoms per site. The temperature of the atoms trapped in the optical lattice is 1.3 μK. It is measured using the sideband spectroscopy method which is described in section 5.4.1.

5.3.3 Lattice characterisation

The lifetime of the atoms trapped in an optical lattice can be limited by collisions of the atoms with background gas [56]. Lifetime of the trapped atoms in a lattice needs to be higher (of the order of seconds) to increase the duration of clock transition interrogation.

Lattice lifetime is measured by loading atoms in the optical lattice for different durations of time and detecting the corresponding atom numbers. We have measured a lattice lifetime of 559±27 ms by fitting the data using an exponential decay function. The plot is given in Figure 5.7. The lifetime is highly dependent on the pressure level of the vacuum system and it reduces linearly when the pressure increases. It is mainly due to the background collisions. A shutter between the atomic oven and the science chamber would have reduced the collisions, during this stage of the experiment, there wasn't one. The lifetime measurements obtained at different pressure values are plotted in Figure 5.8. The measurements were performed at a lattice trap depth of $150E_R$.

Later on, further modifications such as installing a shutter, replacing the getter ion pump with a new one are implemented and a lower level of vacuum at 1×10^{-10} mbar is achieved leading to an improved lifetime of 5 s. See [93] for more details.

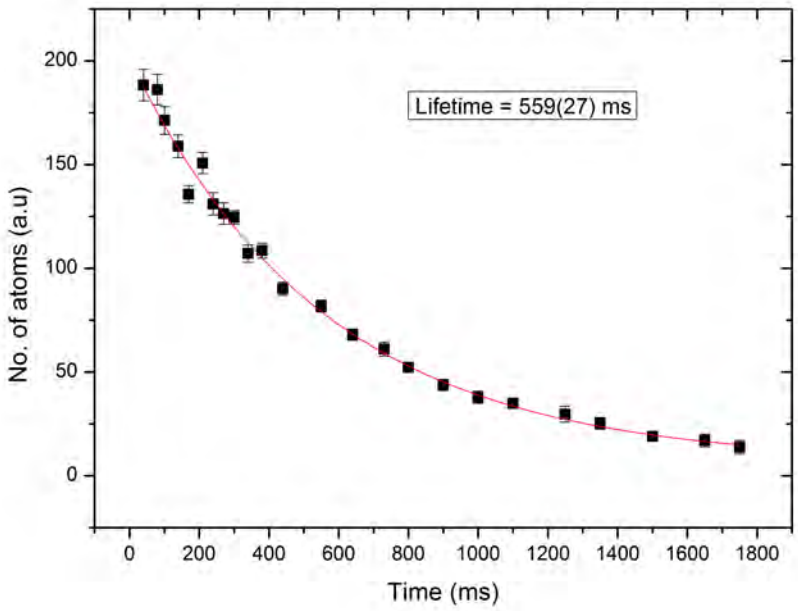

Figure 5.7: Lifetime of atoms trapped in the lattice formed by the 813 nm laser.

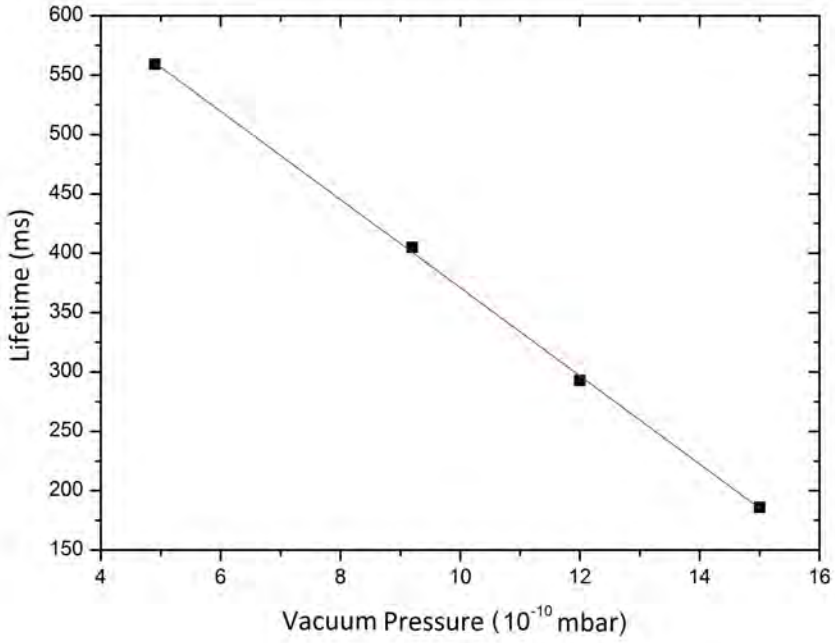

Figure 5.8: Lifetime of atoms trapped in the lattice observed at different vacuum pressure values.

5.3.4 Overlapping clock and lattice laser beams in the science chamber

A vertical lattice trap is sufficient to reduce the laser intensity required to trap the atoms against any gravitational effects [90]. In the SOC2 system, the lattice laser and the clock laser are incorporated into the chamber from the vertical direction. The input of the lattice laser comes from the bottom of the set-up, whereas the clock laser enters from the top of the chamber. Both lasers are overlapped throughout the beam path. A small amount of the 813 nm beam power is transmitted through the 698 nm clock laser fibre. The alignment of the clock laser onto the lattice is optimised by increasing the transmitted 813 nm power by tuning the fibre coupler and mirror at the clock laser input side. Figure 5.9 explains the overlapping between the clock and the lattice laser.

The lattice laser beam exiting the fibre is collimated using a 6.2 mm collimating lens. The beam is then focussed at the centre of the science chamber by a 75 mm lens and another 75 mm lens placed on the other side of the science chamber collimates the laser beam. The beam is then retro-reflected by a dichroic mirror which is 99% reflective at 813 nm and 91% transmissive at 698 nm. The beam waist of the lattice laser is 49 μm. The clock laser beam exiting the fibre is collimated by a lens of 4.5 mm. A 2.6:1 telescope (f=50 mm, f=19 mm) is employed to increase the size of clock laser beam compared to the lattice beam size. Then the beam, after passing through a half wave plate, is redirected by a mirror to overlap with the lattice laser beam. A beam waist of 64 μm, which is larger than the lattice, is measured for the clock laser.

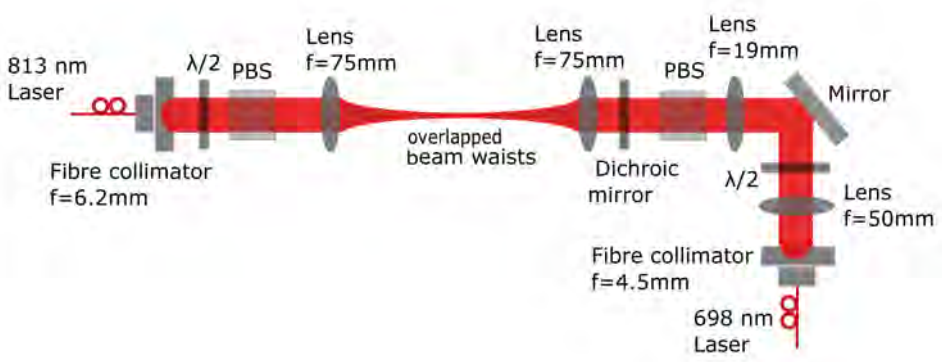

Figure 5.9: Schematic design of the clock spectroscopy laser and lattice laser overlap.

5.3.5 Magnetically induced clock transition

As described in section 2.4.1, to induce the doubly forbidden clock transition in ^{88}Sr, a homogeneous magnetic field is required. It is generated by driving the MOT coils in Helmholtz configuration

which results in the admixture of the energy levels $^3P_1$ and $^3P_0$. The MOT coils consist of

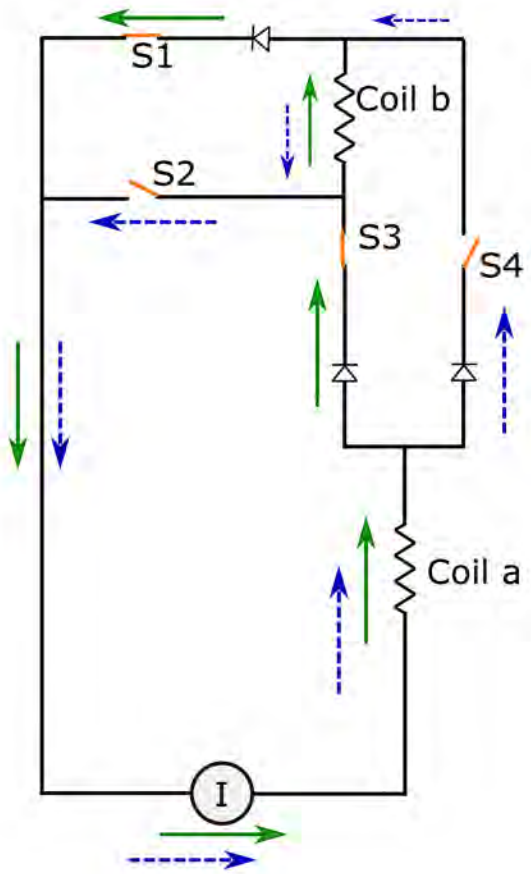

Figure 5.10: Circuit diagram of the switch for the anti-Helmholtz and Helmholtz coil configuration to generate magnetic fields in the atomic clock. The green arrows show the current flow through the Helmholtz configuration (clock interrogation) and the dashed blue arrows show the current flow through the anti-Helmholtz configuration (MOT).

rectangular copper wires with dimensions of 14 mm × 0.25 mm. There are 48 windings which yield a magnetic field of 45 G/cm when a current of 10.4 A is applied in anti-Helmholtz configuration. The same MOT coils are employed to generate a homogeneous magnetic field otherwise called the 'bias field'. For that, the polarity of the current (direction of current flow) through one of the magnetic coils is switched using 60A MOSFET (model: SKM111AR, Semikron) based switching system. This switch is built based on an idea from Joseph Sundar's PhD thesis [136]. Figure 5.10 shows the circuit diagram for switching the direction of current flow through the coils to work in Helmholtz and anti-Helmholtz configuration. The polarity of the current through coil 'a' is kept the same in both configurations, while the polarity is changed for coil 'b'. The switching is carried out by means of the switches S1, S2, S3, and S4. In Helmholtz configuration, switches S1 and S3

are closed. Hence, both coils carry electric currents with same sign. This generates the bias field. The direction of the current flow is represented by green arrows. To run the same set of coils in anti-Helmholtz configuration during the MOT stage, the switches S2 and S4 are closed and the other two are open. Therefore, the current flows through the coils with opposite polarity. This generates a quadrupole magnetic field. The dashed blue arrows show the direction of the current flow. The switches are turned on and off by sending signals from the FPGA, which also controls the magnitude of the current flowing through the coils.

5.4 Clock transition spectroscopy

The interrogation of the clock transition is established with the clock laser mentioned in section 5.2. The clock laser output is sent to the atomics package via an optical fibre and overlapped with the lattice laser beam. Once the atoms are trapped in the lattice, the Helmholtz magnetic field is set and the clock laser interrogation starts after 30 ms. The waiting time is introduced to ensure that all untrapped atoms are expelled from the lattice. The sequence is shown in Figure 5.6. The clock laser frequency is detuned and scanned across the atoms step by step to search for the clock transition. As can be seen from Figure 5.6, the clock signal detection is performed in two stages: ground state atoms detection (GS) and excited state atoms detection (ES). For the detections a 2 mW, resonant 461 nm laser beam is used. The signal from the atoms is monitored using a PMT. When the clock laser interacts with the atoms trapped in the lattice, the transition from $^1S_0$ to $^3P_0$ takes place. The transition is detected by measuring the fluorescence using a 461 nm laser. In detail, 461 nm laser beam used to detect the atoms excites the transition from $^1S_0$ to $^1P_1$ which then is detected by the PMT. After 10 ms of the GS detection, the detection laser is turned off and the repumper lasers are turned on for 10 ms. This process repumps the atoms left in the $^3P_0$ state to $^3S_1$ and decays to the ground state via $^3P_1$ state. The detection laser is then turned on to detect the atoms now in the ground state. This constitutes ES detection. The scheme of clock transition detection is described in Figure 5.11. The PMT signal detected is plotted in Figure 5.12. The excitation probability (P_e) can be estimated from the GS and ES values as:

$$P_e = \frac{ES}{ES + GS}. \tag{5.1}$$

In order to extract the GS and ES values, the area under the background corrected curve depicted in Figure 5.12 (bottom) is integrated using a Matlab code. The excitation probability is at maximum value when the clock laser frequency is in resonance with the clock transition of the atoms. After obtaining the P_e values at various frequency detunings, they are plotted to obtain the clock transition linewidth.

The very first clock transition with the SOC2 system resulted in a linewidth of 760 Hz. This

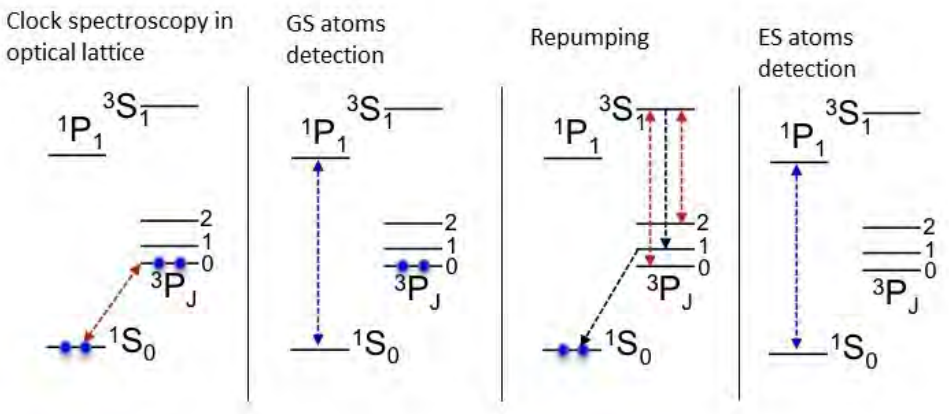

Figure 5.11: Schematic diagram showing the stages of clock transition detection using a resonant 461 nm laser beam.

broader linewidth compared to later linewidth measurements such as resulting 7 Hz was mainly due to the fluctuations in the vacuum level of the clock cavity. After minimising the vacuum fluctuations, a linewidth of 44±0.3 Hz is obtained at 5.9 mT bias field, 266 mW/cm^2 clock laser intensity, and 100 ms interrogation time. Figure 5.13 shows the linewidth of the clock transition obtained by fitting the obtained data with Lorentzian function. The smallest clock transition linewidth measured using the laser locked to only the SOC2 cavity is 32 Hz.

The stability of the clock laser is one of the factors that limit us from obtaining a narrower clock transition. This led us to phase lock the SOC2 laser with PTB's clock laser which is locked to an ultra-stable reference called 'beast' cavity. More details about the cavity can be found in reference [137]. After the phase lock, the atoms are again interrogated with the clock laser and the linewidth could be reduced further. With a clock laser intensity of 270 mW/cm^2, bias field of 3.9 mT, lattice power of 210 mW, and interrogation time of 150 ms, we have obtained a linewidth of 7±0.2 Hz. The excitation probability obtained is 0.46. A further narrower linewidth of the order of sub-Hz is reported in [93]. This is obtained by stabilising the reference laser (PTB's clock laser) to a cryogenic silicon cavity which is operating at 124 K [138] and to ^{87}Sr atoms. This reduced the SOC2 clock transition linewidth to 220 mHz. We have performed experiments to understand the relation between the clock transition linewidth, bias field, and the lattice power. The linewidth reduces linearly when the bias field is reduced. The data obtained with a constant clock laser intensity of 750 mW/cm^2 and lattice power of 121 mW is plotted in Figure 5.14.

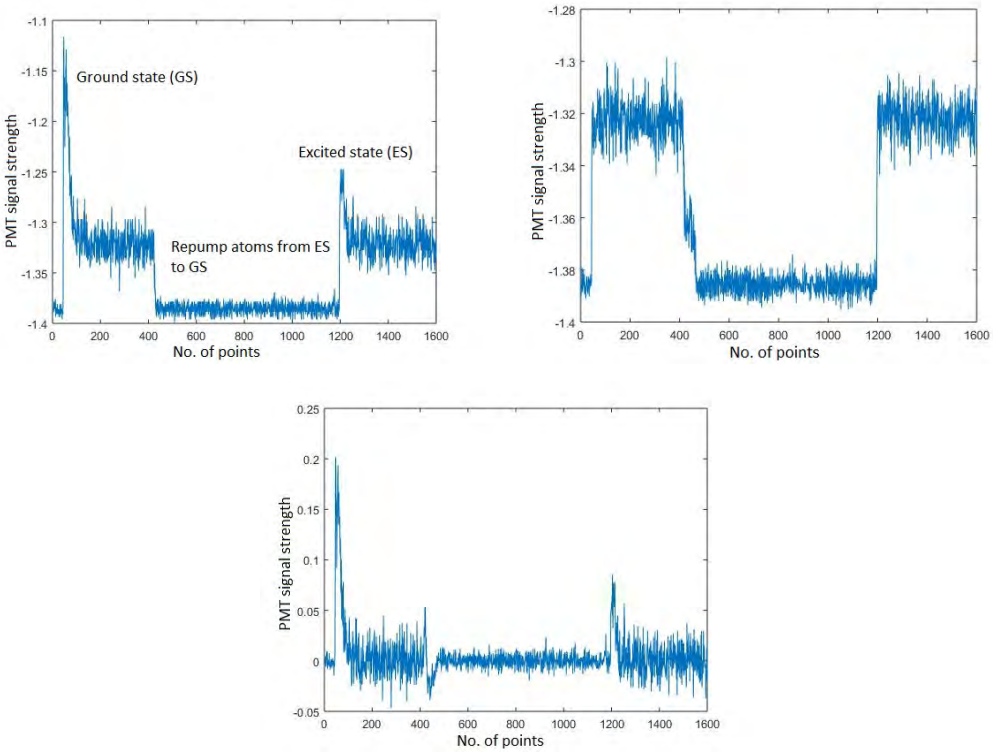

Figure 5.12: Left: Signal detected by the PMT during the clock laser interrogation. Right: Background noise detected before measuring the clock transition. Bottom: Background corrected spectrum.

5.4.1 Sideband spectroscopy

Temperature of the atoms trapped in the lattice and the trap frequencies can be evaluated using sideband spectroscopy technique. The clock laser frequency is detuned and scanned in a wide range to see the sidebands of the clock transition. The sidebands are generated due to the motion of the trapped atoms in the lattice potential, as shown in Figure 2.8. The frequency at which the atoms move in the potential well and occupy the vibrational energy state is known as sideband frequency [139]. The transition $n_z \rightarrow n_z$-1 is the red sideband and $n_z \rightarrow n_z+1$ is the blue sideband. The suppression of red sideband compared to the blue sideband indicates the temperature of the atoms along the strong confinement axis. The plot represented in Figure 5.15 shows the sideband spectroscopy results. It can be seen that the sidebands are smeared out towards the carrier. This skewing occurs due to the coupling between the transverse and longitudinal degrees of freedom making the longitudinal transition frequency dependent on the transverse motional state. The spectrum obtained is taken with 122 mW of lattice laser power, clock laser power of 0.530 mW which corresponds to an intensity of 16.4 W/cm^2, and a bias field of 19.6 mT. The temperature T_z of the atoms trapped in the lattice can be determined as the ratio of the integral of red and

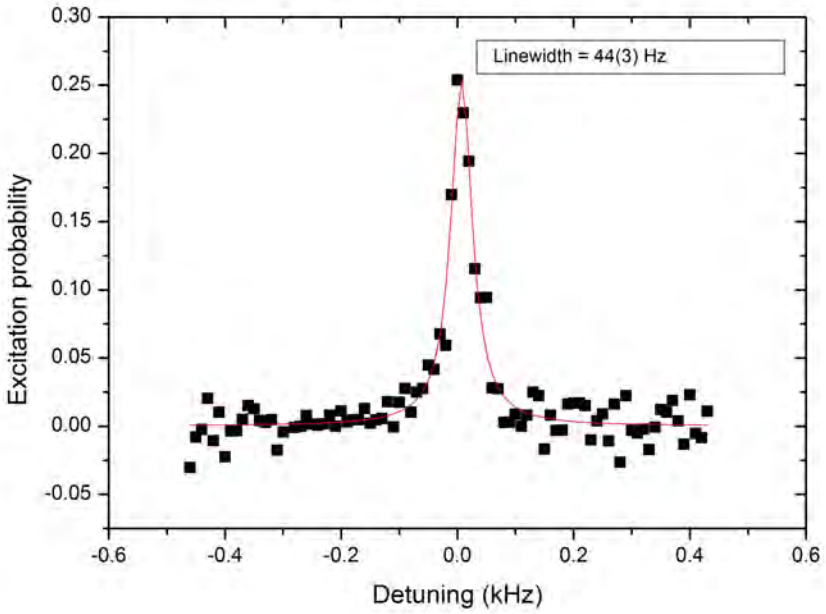

Figure 5.13: Clock transition linewidth obtained by interrogating the SOC2 clock laser.

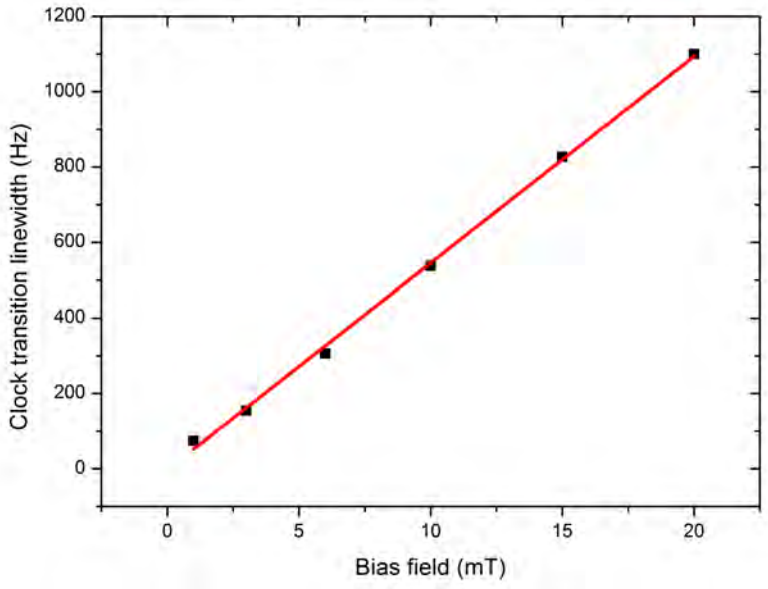

Figure 5.14: Linear dependence of the transition linewidth on the bias field.

blue sidebands [139]:

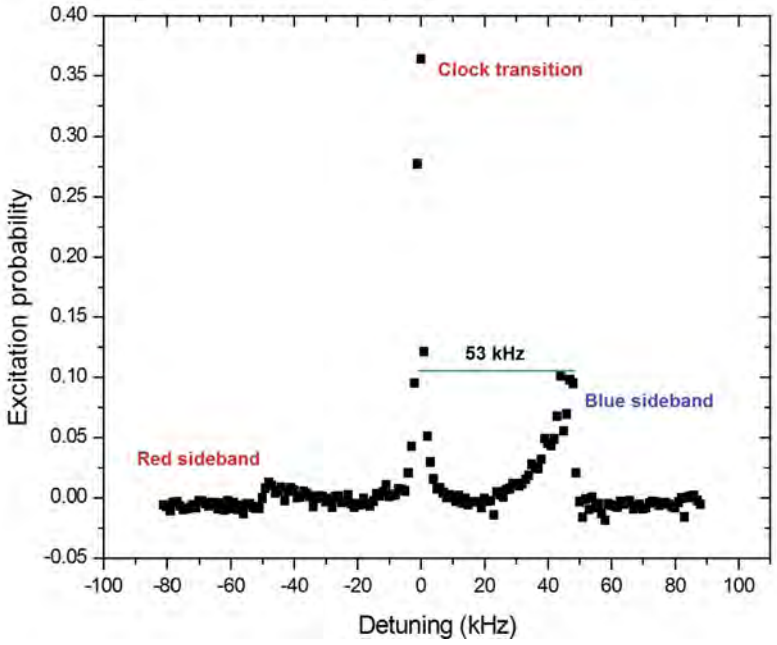

Figure 5.15: Sideband spectrum obtained by scanning the clock laser across the trapped atoms in the lattice. The measured trap frequency is 53 kHz.

$$\frac{\sigma_{red}}{\sigma_{blue}} = \frac{\sum_{n_z=1}^{N_z} e^{-E_{n_z}/k_B T_z}}{\sum_{n_z=0}^{N_z} e^{-E_{n_z}/k_B T_z}} = 1 - \frac{e^{-E_0/k_B T_z}}{\sum_{n_z=0}^{N_z} e^{-E_{n_z}/k_B T_z}}, \tag{5.2}$$

where E_{n_z} is the energy of the longitudinal state n_z. Therefore, the temperature is:

$$T_z = \frac{h\nu_z}{k_B \ln(\frac{\sigma_{blue}}{\sigma_{red}})}, \tag{5.3}$$

where ν_z is the longitudinal trap frequency (see [139] for derivation of the above equations). With this method, the trap frequency is measured as 53 kHz and the longitudinal temperature as 1.3 μK.

Figure 5.16 shows the calculated and measured trap frequencies. The trap potential can be estimated from the lattice laser intensity at the trap region and it is linearly dependent on the beam power (or intensity) as plotted in Figure 5.17. The measured and calculated trap frequencies are in agreement at lower trap depths and discrepancy arises as trap depth increases. It could be that when trap depth is deeper (higher trap volume), atoms are trapped away from lattice waist and the potential experienced by the atom might be low.

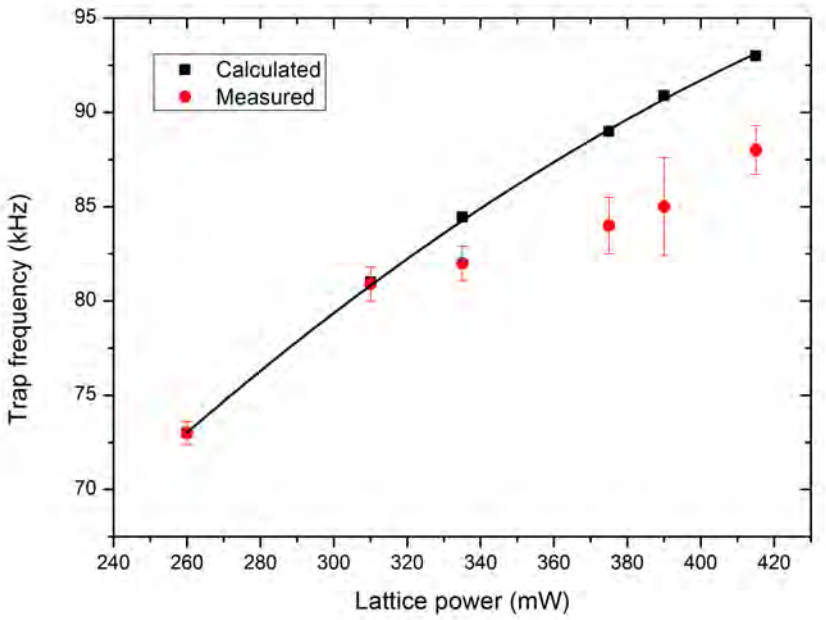

Figure 5.16: Measured and calculated trap frequencies at different trap potentials.

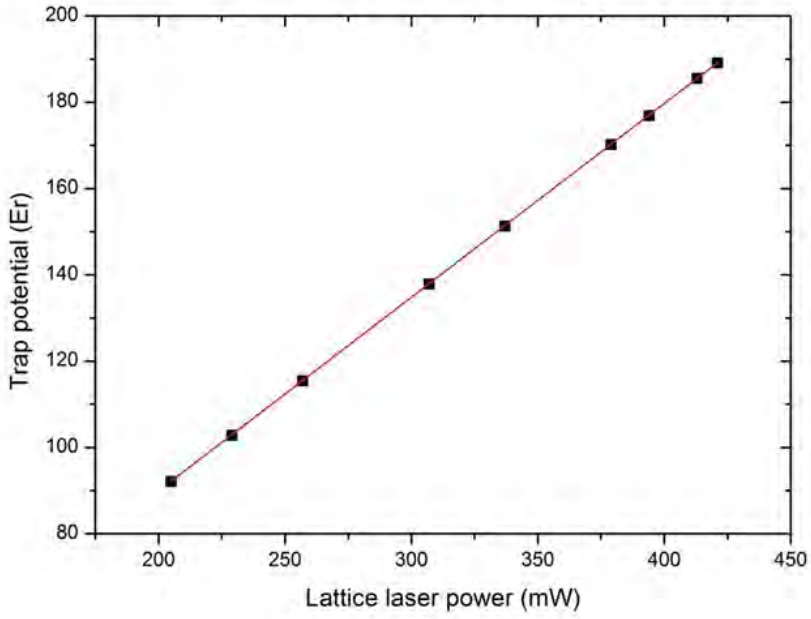

Figure 5.17: Dependence of trap potential on the lattice laser power (calculated).

5.4.2 Rabi oscillation

Rabi oscillation is employed to study the collisional effects on the atoms' coherence time and density dependant frequency shifts [139]. As described in section 2.4.1, the clock laser light field introduces an AC Stark shift and applied magnetic field introduces a second order Zeeman shift, it is important to find a lower laser intensity as well as magnetic field for clock transition interrogation. Equation 2.34, $\Omega=\alpha\sqrt{I}|B|=1/2T_\pi$, implies that longer coherence time (T_π), lower Rabi frequency due to minimal laser intensity and magnetic field are required for clock transition interrogation in bosonic strontium. We measured the Rabi oscillation frequency of the clock transition by setting the clock laser frequency at the maximum excitation probability and interrogating the transition for several milliseconds. The data of the excitation probability at different interrogation times are obtained and plotted to find the Rabi frequency of the oscillation. Figure 5.18 represents a Rabi oscillation measurement. The Rabi frequency and decay time values are obtained after fitting the data obtained using the function $a + \exp\frac{(-x)}{c}\sin(2\pi\frac{(x-d)}{e})b$ where a,b,c,d and e are offset, amplitude, decay constant, phase shift, and period of the oscillation, respectively. The Rabi frequency, Ω, is $1/e$. The laser intensity, magnetic field and interrogation time used during the measurement were 459 mW/cm^2, 4.5 mT and 100 ms respectively and it resulted in a Rabi frequency of 10 Hz. The associated Zeeman shift $\Delta_B=\beta B^2$ is -160.8 Hz and AC stark shift $\Delta_L=\kappa I$ is -7.9 Hz, see section 2.4.1 for equations. Later, during the course of the SOC2 project, much smaller shifts are obtained (not included in this thesis, see [93] for details).

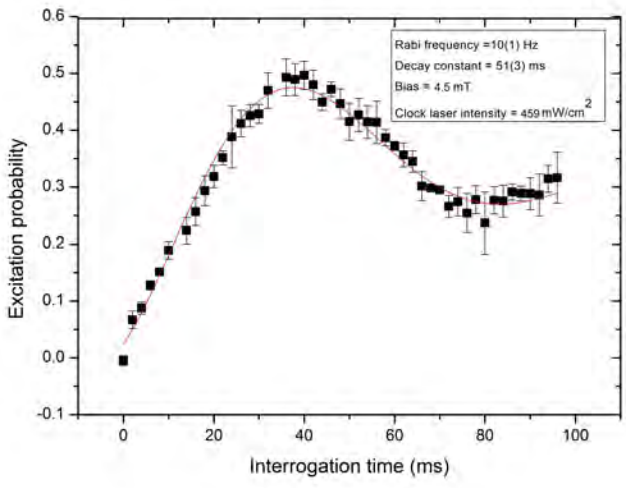

Figure 5.18: Rabi oscillation of the probability of the excited state measured with a clock laser intensity of 459 mW/cm^2 and a 4.5 mT bias field. The resulting Rabi frequency is 10 Hz and the decay constant is 51 ms.

5.5 Stability measurements

The clock laser stability is measured before and after locking the laser to the clock transition. For that, the beat frequency of the SOC2 clock laser with PTB's ultra-stable clock laser with stability 1×10^{-16} at 1 s [137] is measured using a frequency counter and subsequently, the Allan deviation is calculated to understand the stability of the clock laser. The resulting graph is shown in Figure 5.19. At 1 s, the stability is 1.59×10^{-14}. This high instability was due to the fluctuating vacuum level of the SOC2 cavity to which the clock laser is locked. It's decided to send the clock cavity to SYRTE, who originally manufactured it, for upgrade and further testing. Due to the vacuum fluctuation in the SOC2 cavity, the SOC2 clock laser is then stabilised, alongside with SOC2 cavity, to PTB's ultra-stable clock laser.

Later on, a transition linewidth of 3 Hz is obtained. This time, the SOC2 clock laser is phase locked to PTB's ultra-stable clock laser and then locked to ^{88}Sr atoms, see Figure 5.5 for clock laser stabilisation scheme. The total cycle time during this measurement is 1.07 s. The temperature of the science chamber is monitored using a 10 kΩ thermistor. It is 28.8°C with a fluctuation of 0.2°C. The locking of a laser to the clock transition is described in section 2.5. PTB's ultra-stable clock laser is locked to the 'beast' cavity and then further referenced to ^{87}Sr atoms. The beat frequency detected by beating the SOC2 clock laser and PTB's clock laser is fed to a frequency counter to count and store the frequency. The resulting Allan deviation is plotted in Figure 5.20. During this measurement, the power fluctuation of the clock laser, which was mainly due to the varying polarisation is minimised to a large extend. This helped in improving the stability.

In this chapter we discussed the progress in the development of SOC2 system. Characterisation of atoms trapped in the optical lattice, preparation of atoms for clock laser interrogation, alignment of clock laser over the optical lattice, magnetically induced clock transition spectroscopy, and characterisation of the clock transition are covered. We have measured a stability of 1.9×10^{-16} at 2 s for the SOC2 system. In the next chapter, we have conclusions and outlook of the works that have been discussed in the previous chapters.

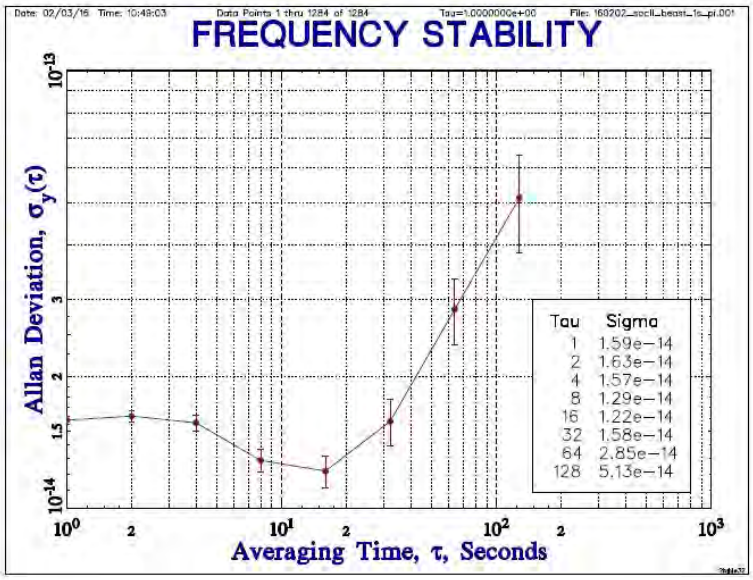

Figure 5.19: Stability measurement of the SOC2 clock laser. Allan deviation is obtained by measuring the beat note between the SOC2 clock laser and PTB's utra-stable clock laser (locked to the 'beast' cavity)

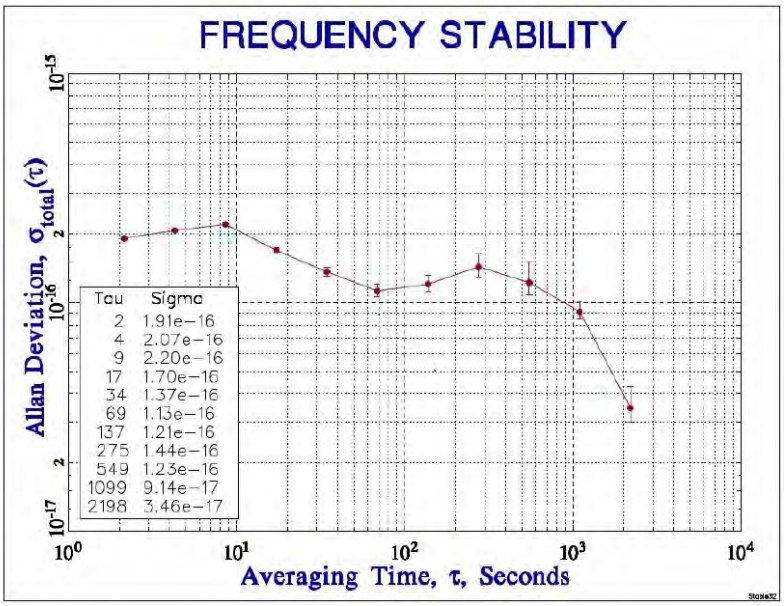

Figure 5.20: Allan deviation of the beat note measurement between ^{87}Sr and ^{88}Sr clocks.

Chapter 6

Conclusions and Outlook

This thesis presents the research work undertaken by the author for the development of strontium optical lattice clocks. The main research focus was towards two clock systems, namely, the miniclock and the Space Optical lattice Clock (SOC2) systems. The 689 nm master oscillator power amplifier (MOPA), the 30 mm cavity, and the multiple frequency stabilisation unit (FSU) were built for the miniclock. In SOC2, research works were undertaken on clock transition spectroscopy with ^{88}Sr atoms. Along with these main activities, a considerable amount of time was spent on design and construction of laser systems, electronic circuits, vacuum chambers, setting up several optical reference cavities for laser frequency stabilisation, improving the performance of the clock laser, and stability transfer between the clock laser and the frequency comb.

6.1 Conclusions

The first milestone during this PhD was to establish a master oscillator power amplifier (MOPA) system at 689 nm as a second stage cooling laser for strontium. The aim of this laser is to be used in the miniclock project to obtain a red MOT. It gives an output of 330 mW after the tapered amplifier which is employed for power amplification. The details of these achievements and further characterisation results can be found in chapter 3. The frequency of the laser is then stabilised to a 30 mm long optical reference cavity using a Pound-Drever-Hall lock on the dual sideband due to the cavity's large free spectral range of 5 GHz. The cavity is constructed by optically contacting fused silica mirrors onto an ultra-low expansion glass (ULE) spacer. The cavity is then placed inside two aluminium housings for temperature stabilisation, each supported by viton balls for rigid mounting as described in section 4.3. The aim of using a smaller cavity is to reduce the size of the locking system, as the miniclock is a project which is moving towards achieving a compact atomic clock package. More details of the optical reference cavity can be found in section 4.1. A

red MOT transition with 25,000 atoms is obtained using the MOPA. Initially, a transfer efficiency of 5% from the blue MOT to red MOT has been achieved. During the second stage interrogation, the laser linewidth was 98.9±0.3 kHz. Due to the large linewidth and frequency drift rate, the optical reference cavity is redesigned to be housed under vacuum in order to reduce the cavity drift rate. See chapter 4 for more details.

The design of the vacuum chamber for the optical reference cavity is described in detail in section 4.4. The outer chamber is made of titanium and inner housings are made of aluminium. Two sets of vacuum chambers have been made: one is at NPL and the second one is at Birmingham. Therefore, two sets of characterisations are performed with cavities under vacuum. The one of the NPL cavity is performed using the homebuilt MOPA at 689 nm and comparing to an ultra-stable 689 nm laser at NPL. For studying the performance of the cavity at Birmingham, a commercial laser at 689 nm and an ultra-stable clock laser at 698 nm are compared via an optical frequency comb. The cavity which is outside vacuum has a fractional frequency instability of 2.2×10^{-10} at 1 s, whereas the cavity inside vacuum has a fractional frequency instability of 1.7×10^{-10} at 1 s. Both measurements were conducted using the home-built MOPA. Even though the stability during the first few seconds is not much different in both cases, the drift is more pronounced for the cavity outside vacuum. At 10^3 s, the vacuum cavity has a fractional frequency instability of 2.35×10^{-10} while the non vacuum one results in a fractional frequency instability of 8×10^{-10}. The vacuum cavity results in 74.3 kHz linewidth for the laser. The cavity set up in Birmingham is characterised using a TA Pro TOPTICA laser. After locking the laser, and measuring a beat note frequency between the locked laser and the frequency comb which is stabilised to a clock laser, a linewidth of 1.15 kHz is measured. It has a fractional frequency instability of 2.5×10^{-12} at 1 s. Even though the cavity at Birmingham results the best linewidth and stability at 1 s, the cavity drifts away very quickly after the first few seconds. The drift rate is 70 Hz/s, which is mainly due to the cavity temperature, and lab conditions. The fractional frequency instability at 10^3 s is 9×10^{-9}. Sections from 4.8 to 4.10 give more details on the different measurements carried out with different optical reference cavities.

Another milestone achieved during this PhD is the implementation of a multiple frequency stabilisation unit (FSU) for the strontium optical lattice clock. In this set-up, the 689 nm, 679 nm, and 813 nm lasers are locked. This scheme is easily extendable to any number of lasers. One drawback of the multiple laser locking is the requirement for a relatively larger amount of power from each laser, as most of the power is lost due to the number of coupling optics like a 50-50 beam splitter. Regardless of the power loss, this system is good for cost effectiveness, compactness and lower power consumption when combined with a clock package. For details of FSU, see section 4.7.

Another major work that was accomplished during this PhD is the characterisation of the clock transition in the space optical lattice clock (SOC2) using ^{88}Sr atoms. As a first step towards achieving a clock transition, a thorough characterisation of the lattice trap is performed. These measurements are described in section 5.3.3. After optimising the lifetime of atoms in the optical lattice, the first clock transition spectroscopy is performed with the SOC2 clock laser and reference cavity by employing the magnetically induced spectroscopy technique as described in section 5.3.5. As the clock transition linewidth obtained with the SOC2 clock laser system was very broad, another technique is implemented to narrow down the transition linewidth. The SOC2 clock laser system is phase-locked to a laser which is locked to an ultra-stable cavity, known as the 'beast cavity', prior to clock transition interrogation. This has helped to significantly reduce the clock transition linewidth. After obtaining a very narrow transition linewidth of the order of Hz level, the SOC2 clock laser is locked to the atomic transition. An Allan deviation obtained from the beat note measurement of the SOC2 bosonic clock and a Sr fermionic clock resulted in a fractional frequency instability of 1.9×10^{-16} at 1 s averaging time. Information on the SOC2 atomic package, SOC2 clock laser and optical reference cavity, clock transition spectroscopy, and characterisation results are included in sections 5.1, 5.2, 5.4, and 5.5, respectively .

6.2 Outlook

The University of Birmingham is working on transportable and portable atomic optical clocks. The first transportable system was built with a 2D MOT - 3D MOT configuration. The second one, which is the SOC2, became more compact with smaller chamber dimensions and cage systems for integrating optical fibres with the atomics package. The third and the current one in progress is the miniclock. It is a portable system with single beam configuration for realising MOTs and has a significantly smaller footprint than the previous versions.

Realising a clock transition with the miniclock atomics package is the next target. A single frequency red MOT has to be obtained next and trap atoms in the lattice afterwards. A portable lattice trap set-up is already built and tested, see section 3.7 for details. Once atoms are loaded into this trap, atoms can be interrogated using our clock laser. After achieving spectroscopy and initial characterisation of the clock transition, the atomics package will be moved to NPL to integrate with NPL's clock laser and with other lasers built by Birmingham at the NPL site. The system is expected to be deliverable by the end of 2019.

In order to reduce the size of the whole package, compact laser systems are being developed by employing laser diodes from Sacher Lasertechnik and homebuilt laser driving electronics. All lasers except NPL's clock laser will be locked to the 30 mm cavity discussed in section 4.1 for

frequency stabilisation. All the components of the miniclock system will be assembled on a portable rack mount which is now under design. The drift of the 30 mm cavity will be compensated by transferring the stability of the ultra-stable clock laser to the cavity by comparing the clock frequency and the 30 mm cavity locked laser frequency using a frequency comb and feeding forward the frequency correction to the cavity. With all these implementations, we are expecting to achieve a fractional frequency instability of the order of 10^{-15} or less with this compact miniclock system which is known for its single beam MOT configuration and will be a great achievement in the field of strontium optical lattice clocks. This will announce the usability of strontium optical lattice clocks in space technology, defence and navigation systems.

Bibliography

[1] JE Sansonetti and G Nave. Wavelengths, transition probabilities, and energy levels for the spectrum of neutral strontium (Sr I). *Journal of Physical and Chemical Reference Data*, 39(3):033103, 2010. vi, 18, 19

[2] AV Taichenachev, VI Yudin, CW Oates, CW Hoyt, ZW Barber, and L Hollberg. Magnetic field-induced spectroscopy of forbidden optical transitions with application to lattice-based optical atomic clocks. *Physical Review Letters*, 96(8):083001, 2006. vi, vii, 20, 25, 27

[3] S Bilicki. *Strontium optical lattice clocks: clock comparisons for timescales and fundamental physics applications*. PhD thesis, Observatoire de Paris-SYRTE, 2017. vii, 5

[4] O Kock. *Magneto-optical trapping of strontium for use as a mobile frequency reference*. PhD thesis, University of Birmingham, 2013. vii, ix, 5, 47

[5] Y Huang, H Guan, M Zeng, L Tang, and K Gao. $40Ca^{+}$ ion optical clock with micromotion-induced shifts below 1×10^{-18}. *Physical Review A*, 99(1):011401, 2019. vii, 5

[6] SM Brewer, J-S Chen, AM Hankin, ER Clements, CW Chou, DJ Wineland, DB Hume, and DR Leibrandt. An $^{27}Al^{+}$ quantum-logic clock with systematic uncertainty below 10^{-18}. *arXiv preprint arXiv:1902.07694*, 2019. vii, 5

[7] S Origlia, S Schiller, MS Pramod, L Smith, Y Singh, W He, S Viswam, D Świerad, J Hughes, K Bongs, et al. Development of a strontium optical lattice clock for the SOC mission on the ISS. In *SPIE Photonics Europe*, pages 990003–990003. International Society for Optics and Photonics, 2016. xi, 13, 94

[8] D Świerad, S Häfner, S Vogt, B Venon, D Holleville, S Bize, A Kulosa, S Bode, Y Singh, K Bongs, et al. Ultra-stable clock laser system development towards space applications. *Scientific Reports*, 6:33973, 2016. xi, 98, 99

[9] M Bennett, MF Schatz, H Rockwood, and K Wiesenfeld. Huygens's clocks. *Proceedings: Mathematics, Physical and Engineering Sciences*, pages 563–579, 2002. 2

[10] DB Sullivan. Time and frequency measurement at NIST: The first 100 years. In *Frequency Control Symposium and PDA Exhibition, 2001. Proceedings of the 2001 IEEE International*, pages 4–17. IEEE, 2001. 2

[11] J Jespersen and J Fitz-Randolph. *From sundials to atomic clocks: understanding time and frequency*. Dover Publications, ISBN: 978-0486409139, 2011. 3

[12] M Lombardi. The accuracy & stability of quartz watches. *Horological Journal*, 150(2):57, 2008. 3

[13] MA Lombardi, TP Heavner, and SR Jefferts. NIST primary frequency standards and the realization of the SI second. *NCSLI Measure*, 2(4):74–89, 2007. 3

[14] H Lyons. The atomic clock: a universal standard of frequency and time. *The American Scholar*, 19(2):159–168, 1950. 3

[15] H Lyons. Spectral lines as frequency standards. *Annals of the New York Academy of Sciences*, 55(1):831–871, 1952. 3

[16] W Markowitz, RG Hall, L Essen, and JVL Parry. Frequency of cesium in terms of ephemeris time. *Physical Review Letters*, 1(3):105, 1958. 4

[17] BN Taylor and PJ Mohr. The role of fundamental constants in the international system of units (SI): present and future. *IEEE Transactions on Instrumentation and Measurement*, 50(2):563–567, 2001. 4

[18] R Wynands and S Weyers. Atomic fountain clocks. *Metrologia*, 42(3):S64, 2005. 4

[19] V Gerginov, N Nemitz, D Griebsch, M Kazda, R Li, K Gibble, R Wynands, and S Weyers. Recent improvements and current uncertainty budget of PTB fountain clock CSF2. In *EFTF-2010 24th European Frequency and Time Forum*, pages 1–7. IEEE, 2010. 4

[20] T Zelevinsky, MM Boyd, AD Ludlow, SM Foreman, S Blatt, T Ido, and J Ye. Optical clock and ultracold collisions with trapped strontium atoms. *Hyperfine Interactions, Springer*, 174(1-3):55–64, 2007. 4

[21] CW Hoyt, ZW Barber, Christopher W Oates, TM Fortier, SA Diddams, and L Hollberg. Observation and absolute frequency measurements of the $^1S_0$-$^3P_0$ optical clock transition in neutral ytterbium. *Physical Review Letters*, 95(8):083003, 2005. 4

[22] J Friebe, A Pape, M Riedmann, K Moldenhauer, T Mehlstäubler, N Rehbein, C Lisdat, EM Rasel, W Ertmer, H Schnatz, et al. Absolute frequency measurement of the magnesium intercombination transition $^1S_0$-$^3P_1$. *Physical Review A*, 78(3):033830, 2008. 4

[23] L De Sarlo, M Favier, R Tyumenev, and S Bize. A mercury optical lattice clock at LNE-SYRTE. In *Journal of Physics: Conference Series*, volume 723, page 012017. Institute of Physics Publishing, 2016. 4

[24] CW Oates. Calcium thermal beam optical clock. *NIST*, 2013. `https://www.nist.gov/programs-projects/calcium-thermal-beam-optical-clock`. 4

[25] Gibble lab. *Cadmium optical lattice clock and ultracold collisions*, 2017(accessed September,04,2017). `https://sites.psu.edu/gibble/`. 4

[26] T Rosenband, PO Schmidt, DB Hume, WM Itano, TM Fortier, JE Stalnaker, K Kim, Scott A Diddams, JCJ Koelemeij, JC Bergquist, et al. Observation of the $^1S_0$ - $^3P_0$ clock transition in Al^{27+}. *Physical Review Letters*, 98(22):220801, 2007. 4

[27] N Poli, CW Oates, P Gill, and GM Tino. Optical atomic clocks. *arXiv preprint arXiv:1401.2378*, 2014. 4

[28] H Schnatz, B Lipphardt, J Helmcke, F Riehle, and G Zinner. First phase-coherent frequency measurement of visible radiation. *Physical Review Letters*, 76(1):18, 1996. 7

[29] T Udem, J Reichert, R Holzwarth, and TW Hänsch. Absolute optical frequency measurement of the cesium d1 line with a mode-locked laser. *Physical Review Letters*, 82(18):3568, 1999. 7

[30] SA Diddams, DJ Jones, J Ye, ST Cundiff, JL Hall, JK Ranka, RS Windeler, R Holzwarth, T Udem, and TW Hänsch. Direct link between microwave and optical frequencies with a 300 THz femtosecond laser comb. *Physical Review Letters*, 84(22):5102, 2000. 7

[31] CJ Foot. *Atomic physics*, volume 7. Oxford University Press, ISBN: 9780198506966, 2005. 8, 17, 20

[32] B Hofmann-Wellenhof, H Lichtenegger, and E Wasle. *GNSS–global navigation satellite systems: GPS, GLONASS, Galileo, and more.* Springer Science & Business Media, ISBN: 9783211730171, 2007. 9

[33] S Feltham, G Gianfiglio, and F Reina. ACES: a time and frequency mission for the international space station. *The Institute of Engineering and Technology - IET Digital Library*, pages 389–394, 2004. 9

[34] P Wolf, C Salomon, and S Reynaud. Space clocks to test relativiy: ACES and SAGAS. *Proceedings of the International Astronomical Union*, 5(S261):377–389, 2009. 9

[35] P Wolf, Ch J Bordé, A Clairon, L Duchayne, A Landragin, P Lemonde, G Santarelli, W Ertmer, E Rasel, FS Cataliotti, et al. Quantum physics exploring gravity in the outer solar system: the SAGAS project. *Experimental Astronomy*, 23(2):651–687, 2009. 9

[36] NK Pavlis and MA Weiss. The relativistic redshift with 3×10^{-17} uncertainty at NIST, Boulder, Colorado, USA. *Metrologia*, 40(2):66, 2003. 9

[37] R Bondarescu, M Bondarescu, G Hetényi, L Boschi, P Jetzer, and J Balakrishna. Geophysical applicability of atomic clocks: direct continental geoid mapping. *Geophysical Journal International*, 191(1):78–82, 2012. 10

[38] B Linet and P Teyssandier. Time transfer and frequency shift to the order $1/c^4$ in the field of an axisymmetric rotating body. *Physical Review D*, 66(2):024045, 2002. 10

[39] C Lisdat, G Grosche, N Quintin, C Shi, SMF Raupach, C Grebing, D Nicolodi, F Stefani, A Al-Masoudi, S Dörscher, et al. A clock network for geodesy and fundamental science. *Nature Communications*, 7, 2016. 10

[40] G Edward Marti, Ross B Hutson, Akihisa Goban, Sara L Campbell, N Poli, and J Ye. Imaging optical frequencies with 100 μ hz precision and 1.1 μ m resolution. *Physical Review Letters*, 120(10):103201, 2018. 12

[41] WF McGrew, X Zhang, RJ Fasano, SA Schäffer, K Beloy, D Nicolodi, RC Brown, N Hinkley, G Milani, M Schioppo, et al. Atomic clock performance enabling geodesy below the centimetre level. *Nature*, 564(7734):87, 2018. 12

[42] RL Kurucz and B Bell. Atomic line data, Kurucz CD-ROM No. 23. Cambridge, MA. *Smithsonian Astrophysical Observatory*, 1995. 12

[43] E Oelker, RB Hutson, CJ Kennedy, L Sonderhouse, T Bothwell, A Goban, D Kedar, C Sanner, JM Robinson, GE Marti, et al. Demonstration of 4.8× 10- 17 stability at 1 s for two independent optical clocks. *Nature Photonics*, page 1, 2019. 13

[44] I Ushijima, M Takamoto, M Das, T Ohkubo, and H Katori. Cryogenic optical lattice clocks. *Nature Photonics*, 9(3):185–189, 2015. 13, 31

[45] G Vallet, S Bilicki, R Le Targat, and J Lodewyck. Study of accuracy and stability of sr lattice clocks at lne-syrte. In *2018 Conference on Precision Electromagnetic Measurements (CPEM 2018)*, pages 1–2. IEEE, 2018. 13

[46] A Al-Masoudi, S Dörscher, S Häfner, U Sterr, and C Lisdat. Noise and instability of an optical lattice clock. *Physical Review A*, 92(6):063814, 2015. 13

[47] S Falke, N Lemke, C Grebing, B Lipphardt, S Weyers, V Gerginov, N Huntemann, C Hagemann, A Al-Masoudi, S Häfner, et al. A strontium lattice clock with 30×10^{-17} inaccuracy and its frequency. *New Journal of Physics*, 16(7):073023, 2014. 13

[48] N Poli, M Schioppo, S Vogt, U Sterr, Ch Lisdat, GM Tino, et al. A transportable strontium optical lattice clock. *Applied Physics B*, 117(4):1107–1116, 2014. 13, 93

[49] R Hobson. *An optical lattice clock with neutral strontium*. PhD thesis, University of Oxford, 2016. 13, 81

[50] IR Hill, R Hobson, W Bowden, EM Bridge, S Donnellan, EA Curtis, and P Gill. A low maintenance Sr optical lattice clock. In *Journal of Physics: Conference Series*, volume 723, page 012019. Institute of Physics Publishing, 2016. 13

[51] S Origlia, MS Pramod, S Schiller, Y Singh, K Bongs, R Schwarz, A Al-Masoudi, S Dörscher, S Herbers, S Häfner, et al. Towards an optical clock for space: Compact, high-performance optical lattice clock based on bosonic atoms. *Physical Review A*, 98(5):053443, 2018. 13

[52] TW Hänsch and AL Schawlow. Cooling of gases by laser radiation. *Optics Communications*, 13(1):68–69, 1975. 14

[53] S Chu. Nobel lecture: The manipulation of neutral particles. *Reviews of Modern Physics*, 70(3):685, 1998. 14

[54] CN Cohen-Tannoudji. Nobel lecture: Manipulating atoms with photons. *Reviews of Modern Physics*, 70(3):707, 1998. 14

[55] WD Phillips. Nobel lecture: Laser cooling and trapping of neutral atoms. *Reviews of Modern Physics*, 70(3):721, 1998. 14, 15

[56] AD Ludlow. *The Sr Optical Lattice Clock: Optical Spectroscopy with sub-Hertz Accuracy*. PhD thesis, PhD thesis, University of Colorado, 2008. https://jila. colorado. edu/yelabs . 14, 102

[57] PD Lett, WD Phillips, SL Rolston, CE Tanner, RN Watts, and CI Westbrook. Optical molasses. *Journal of Optical Society of America B*, 6(11):2084–2107, 1989. 15

[58] MM Boyd. *High precision spectroscopy of strontium in an optical lattice: Towards a new standard for frequency and time*. PhD thesis, University of Colorado at Boulder, 2007. 17

[59] GK Woodgate. Elementary atomic structure. *Oxford Science Publications, ISBN: 9780198511564*, 1980. 18

[60] SB Nagel, PG Mickelson, AD Saenz, YN Martinez, YC Chen, T C Killian, P Pellegrini, and R Côté. Photoassociative spectroscopy at long range in ultracold strontium. *Physical Review Letters*, 94(8):083004, 2005. 18

[61] X Xu, TH Loftus, JL Hall, A Gallagher, and J Ye. Cooling and trapping of atomic strontium. *Journal of Optical Society of America B*, 20(5):968–976, 2003. 18, 19

[62] X Xu, TH Loftus, MJ Smith, JL Hall, A Gallagher, and J Ye. Dynamics in a two-level atom magneto-optical trap. *Physical Review A*, 66(1):011401, 2002. 19

[63] TH Loftus, T Ido, MM Boyd, AD Ludlow, and J Ye. Narrow line cooling and momentum-space crystals. *Physical Review A*, 70(6):063413, 2004. 19

[64] H Katori, T Ido, Y Isoya, and M Kuwata-Gonokami. Magneto-optical trapping and cooling of strontium atoms down to the photon recoil temperature. *Physical Review Letters*, 82(6):1116, 1999. 19

[65] S Snigirev, AJ Park, A Heinz, I Bloch, and S Blatt. Fast and dense magneto-optical traps for strontium. *Physical Review A*, 99(6):063421, 2019. 20

[66] CG Townsend, NH Edwards, CJ Cooper, KP Zetie, CJ Foot, AM Steane, P Szriftgiser, H Perrin, and J Dalibard. Phase-space density in the magneto-optical trap. *Physical Review A*, 52(2):1423, 1995. 20

[67] K Shibata, S Yonekawa, and S Tojo. Loading of atoms into an optical trap with high initial phase-space density. *Physical Review A*, 96(1):013402, 2017. 20

[68] VD Ovsiannikov and VG Pal'chikov. Magic wavelengths for frequency standards of deeply cooled alkaline-earth atoms in a Stark-free optical lattice. *Laser Physics*, 15(7):1040–1045, 2005. 22

[69] H Katori, K Hashiguchi, E Yu Ilinova, and VD Ovsiannikov. Magic wavelength to make optical lattice clocks insensitive to atomic motion. *Physical Review Letters*, 103(15):153004, 2009. 22

[70] A Kaplan, MF Andersen, and N Davidson. Suppression of inhomogeneous broadening in rf spectroscopy of optically trapped atoms. *Physical Review A*, 66(4):045401, 2002. 22

[71] H Katori, T Ido, and M Kuwata-Gonokami. Optimal design of dipole potentials for efficient loading of Sr atoms. *Journal of the Physical Society of Japan*, 68(8):2479–2482, 1999. 22

[72] J McKeever, JR Buck, AD Boozer, A Kuzmich, H-C Nägerl, DM Stamper-Kurn, and HJ Kimble. State-insensitive cooling and trapping of single atoms in an optical cavity. *Physical Review Letters*, 90(13):133602, 2003. 22

[73] T Ido and H Katori. Recoil-free spectroscopy of neutral Sr atoms in the lamb-dicke regime. *Physical Review Letters*, 91(5):053001, 2003. 22, 23

[74] M Takamoto, FL Hong, R Higashi, and H Katori. An optical lattice clock. *Nature*, 435(7040):321–324, 2005. 22

[75] A Brusch, R Le Targat, X Baillard, M Fouché, and P Lemonde. Hyperpolarizability effects in a Sr optical lattice clock. *Physical Review Letters*, 96(10):103003, 2006. 22

[76] T Akatsuka, M Takamoto, and H Katori. Optical lattice clocks with non-interacting bosons and fermions. *Nature Physics*, 4(12):954–959, 2008. 23

[77] M Takamoto, T Takano, and H Katori. Frequency comparison of optical lattice clocks beyond the Dick limit. *Nature Photonics*, 5(5):288–292, 2011. 23

[78] H Katori. Spectroscopy of strontium atoms in theLamb-Dicke confinement. In *Frequency Standards and Metrology*, pages 323–330, 2002. 23

[79] T Hong, C Cramer, W Nagourney, and EN Fortson. Optical clocks based on ultranarrow three-photon resonances in alkaline earth atoms. *Physical Review Letters*, 94(5):050801, 2005. 25

[80] R Santra, E Arimondo, T Ido, CH Greene, and J Ye. High-accuracy optical clock via three-level coherence in neutral bosonic ^{88}Sr. 25

[81] AD Ludlow, MM Boyd, J Ye, E Peik, and PO Schmidt. Optical atomic clocks. *Reviews of Modern Physics*, 87(2):637, 2015. 29, 31

[82] C Gross, T Zibold, E Nicklas, J Esteve, and MK Oberthaler. Nonlinear atom interferometer surpasses classical precision limit. *Nature*, 464(7292):1165–1169, 2010. 29, 30

[83] J Appel, PJ Windpassinger, D Oblak, UB Hoff, Niels K, and ES Polzik. Mesoscopic atomic entanglement for precision measurements beyond the standard quantum limit. *Proceedings of the National Academy of Sciences*, 106(27):10960–10965, 2009. 29

[84] GJ Dick. Local oscillator induced instabilities in trapped ion frequency standards. Technical report, DTIC Document, California Institute of Tech Pasadena Jet Propulsion Lab, 1987. 30

[85] A Quessada, RP Kovacich, I Courtillot, A Clairon, G Santarelli, and P Lemonde. The Dick effect for an optical frequency standard. *Journal of Optics B: Quantum and Semiclassical Optics*, 5(2):S150, 2003. 30

[86] J Lodewyck, PG Westergaard, and P Lemonde. Nondestructive measurement of the transition probability in a Sr optical lattice clock. *Physical Review A*, 79(6):061401, 2009. 30

[87] N Poli, ZW Barber, ND Lemke, CW Oates, LS Ma, JE Stalnaker, TM Fortier, SA Diddams, L Hollberg, JC Bergquist, et al. Frequency evaluation of the doubly forbidden $^1S_0$ - $^3P_0$ transition in bosonic ^{174}Yb. *Physical Review A*, 77(5):050501, 2008. 30

[88] MM Boyd, T Zelevinsky, AD Ludlow, S Blatt, T Zanon-Willette, SM Foreman, and J Ye. Nuclear spin effects in optical lattice clocks. *Physical Review A*, 76(2):022510, 2007. 30

[89] AD Ludlow, T Zelevinsky, GK Campbell, S Blatt, MM Boyd, Marcio HG de Miranda, MJ Martin, JW Thomsen, Seth M Foreman, J Ye, et al. Sr lattice clock at 1×10^{-16} fractional uncertainty by remote optical evaluation with a ca clock. *Science*, 319(5871):1805–1808, 2008. 31

[90] C Lisdat, JS Raaj Vellore Winfred, T Middelmann, F Riehle, and U Sterr. Collisional losses, decoherence, and frequency shifts in optical lattice clocks with bosons. *Physical Review Letters*, 103(9):090801, 2009. 31, 104

[91] SG Porsev and A Derevianko. Multipolar theory of blackbody radiation shift of atomic energy levels and its implications for optical lattice clocks. *Physical Review A*, 74(2):020502, 2006. 31

[92] K Beloy, N Hinkley, NB Phillips, JA Sherman, M Schioppo, J Lehman, A Feldman, LM Hanssen, CW Oates, and AD Ludlow. Atomic clock with 1×10^{-18} room-temperature blackbody Stark uncertainty. *Physical Review Letters*, 113(26):260801, 2014. 31

[93] S Origlia. *A high-performance bosonic optical lattice clock*. PhD thesis, Heinrich-Heine-Universität Düsseldorf, 2018. 31, 102, 107, 112

[94] F Riehle. *Frequency standards: basics and applications*. John Wiley & Sons, ISBN: 9783527605958, 2006. 32, 42, 76

[95] ED Black. An introduction to Pound–Drever–Hall laser frequency stabilization. *American Journal of Physics*, 69(1):79–87, 2001. 32, 39

[96] RWP Drever, John L Hall, FV Kowalski, J_ Hough, GM Ford, AJ Munley, and H Ward. Laser phase and frequency stabilization using an optical resonator. *Applied Physics B*, 31(2):97–105, 1983. 32

[97] James I Thorpe, K Numata, and J Livas. Laser frequency stabilization and control through offset sideband locking to optical cavities. *Optics Express*, 16(20):15980–15990, 2008. 32, 41

[98] A Nevsky, S Alighanbari, Q-F Chen, I Ernsting, S Vasilyev, S Schiller, G Barwood, P Gill, N Poli, and GM Tino. Robust frequency stabilization of multiple spectroscopy lasers with large and tunable offset frequencies. *Optics Letters*, 38(22):4903–4906, 2013. 32, 97

[99] S Seel, R Storz, G Ruoso, J Mlynek, and S Schiller. Cryogenic optical resonators: a new tool for laser frequency stabilization at the 1 Hz level. *Physical Review Letters*, 78(25):4741, 1997. 33

[100] BC Young, FC Cruz, WM Itano, and JC Bergquist. Visible lasers with subhertz linewidths. *Physical Review Letters*, 82(19):3799, 1999. 33, 59

[101] M Notcutt, L-S Ma, AD Ludlow, SM Foreman, J Ye, and JL Hall. Contribution of thermal noise to frequency stability of rigid optical cavity via hertz-linewidth lasers. *Physical Review A*, 73(3):031804, 2006. 33

[102] L Chen, JL Hall, J Ye, T Yang, E Zang, and T Li. Vibration-induced elastic deformation of Fabry-Perot cavities. *Physical Review A*, 74(5):053801, 2006. 33

[103] J Alnis, A Matveev, N Kolachevsky, T Udem, and TW Hänsch. Subhertz linewidth diode lasers by stabilization to vibrationally and thermally compensated ultralow-expansion glass fabry-pérot cavities. *Physical Review A*, 77(5):053809, 2008. 33

[104] SA Webster, M Oxborrow, and P Gill. Vibration insensitive optical cavity. *Physical Review A*, 75(1):011801, 2007. 33, 90, 91

[105] T Kessler, C Hagemann, C Grebing, T Legero, U Sterr, F Riehle, MJ Martin, L Chen, and J Ye. A sub-40-mHz-linewidth laser based on a silicon single-crystal optical cavity. *Nature Photonics*, 6(10):687–692, 2012. 33

[106] Y Cunyun. *Tunable external cavity diode lasers*. World Scientific, ISBN: 9789812560889, 2004. 35, 36

[107] A Liem, J Limpert, H Zellmer, and A Tünnermann. 100-W single-frequency master-oscillator fiber power amplifier. *Optics Letters*, 28(17):1537–1539, 2003. 36

[108] AC Wilson, JC Sharpe, CR McKenzie, PJ Manson, and DM Warrington. Narrow-linewidth master-oscillator power amplifier based on a semiconductor tapered amplifier. *Applied Optics*, 37(21):4871–4875, 1998. 36

[109] S-B Xiang, X Xiang, and C-G Feng. Effects of temperature on laser diode ignition. *Optik-International Journal for Light and Electron Optics*, 120(2):85–88, 2009. 37

[110] JCB Kangara, AJ Hachtel, MC Gillette, JT Barkeloo, ER Clements, S Bali, BE Unks, NA Proite, DD Yavuz, PJ Martin, et al. Design and construction of cost-effective tapered amplifier systems for laser cooling and trapping experiments. *American Journal of Physics*, 82(8):805–817, 2014. 39

[111] DZ Anderson. Alignment of resonant optical cavities. *Applied Optics*, 23(17):2944–2949, 1984. 45

[112] H Kogelnik and T Li. Laser beams and resonators. *Applied Optics*, 5(10):1550–1567, 1966. 45, 60

[113] WT Silfvast. Laser fundamentals. *Cambridge University press, ISBN: 9780521541053*, 1996. 45, 60

[114] L Smith. *A transportable strontium optical lattice clock towards space*. PhD thesis, University of Birmingham, 2016. ix, 47, 48, 95

[115] IR Hill, YB Ovchinnikov, EM Bridge, EA Curtis, and P Gill. Zeeman slowers for strontium based on permanent magnets. *Journal of Physics B: Atomic, Molecular and Optical Physics*, 47(7):075006, 2014. 48, 94

[116] W He. *Towards miniaturized strontium optical lattice clock*. PhD thesis, University of Birmingham, 2017. ix, 48, 49, 50

[117] KI Lee, JA Kim, HR Noh, and W Jhe. Single-beam atom trap in a pyramidal and conical hollow mirror. *Optics Letters*, 21(15):1177–1179, 1996. 48

[118] D Świerad. *Stable and ultra-stable laser systems for mobile strontium optical lattice clocks*. PhD thesis, University of Birmingham, 2017. 58, 75, 83

[119] QF Chen, A Nevsky, M Cardace, S Schiller, T Legero, S Häfner, A Uhde, and U Sterr. A compact, robust, and transportable ultra-stable laser with a fractional frequency instability of 1×10^{-15}. *Review of Scientific Instruments*, 85(11):113107, 2014. 58

[120] AD Ludlow, X Huang, M Notcutt, T Zanon-Willette, SM Foreman, MM Boyd, S Blatt, and J Ye. Compact, thermal-noise-limited optical cavity for diode laser stabilization at 1×10^{-15}. *Optics Letters*, 32(6):641–643, 2007. 58, 98

[121] T Legero, T Kessler, and U Sterr. Tuning the thermal expansion properties of optical reference cavities with fused silica mirrors. *Journal of Optical Society of America B*, 27(5):914–919, 2010. 59, 98

[122] SA Webster, M Oxborrow, and P Gill. Subhertz-linewidth nd: Yag laser. *Optics Letters*, 29(13):1497–1499, 2004. 59

[123] T Skettrup, T Meelby, K Færch, S Frederiksen, and C Pedersen. Triangular laser resonators with astigmatic compensation. *Applied Optics*, 39(24):4306–4312, 2000. 60

[124] JJ Ferme. Optical contacting. In *Optical Systems Design (Book)*, pages 26–34. International Society for Optics and Photonics, ISBN: 9780819451361, 2004. 62

[125] G Kalkowski, S Risse, C Rothhardt, M Rohde, and R Eberhardt. Optical contacting of low-expansion materials. In *SPIE Optical Engineering+ Applications*, pages 81261F–81261F. International Society for Optics and Photonics, 2011. 62, 64

[126] RB Holt, HI Smith, and MS Gussenhoven. Research on optical contact bonding. Technical report, 1966. 62

[127] HA Adam, S Kaufman, and BS Liley. Indium seals for dismountable vacuum systems. *Journal of Scientific Instruments*, 34(3):123, 1957. 68

[128] U Hochuli and P Haldemann. Indium sealing techniques. *Review of Scientific Instruments*, 43(8):1088–1089, 1972. 68

[129] B Kaltenhäuser, H Kübler, A Chromik, J Stuhler, and T Pfau. Low retaining force optical viewport seal. *Review of Scientific Instruments*, 78(4):046107, 2007. 68

[130] MD Swallows, MJ Martin, M Bishof, C Benko, Y Lin, S Blatt, Ana M Rey, and J Ye. Operating a ^{87}Sr optical lattice clock with high precision and at high density. *IEEE Transactions on Ultrasonics, Ferroelectrics, and Frequency Control*, 59(3):416–425, 2012. 76

[131] YY Jiang, AD Ludlow, ND Lemke, RW Fox, JA Sherman, L-S Ma, and CW Oates. Making optical atomic clocks more stable with 10^{-16} level laser stabilization. *Nature Photonics*, 5(3):158–161, 2011. 76

[132] S Webster and P Gill. Low-thermal-noise optical cavity. In *Frequency Control Symposium (FCS), 2010 IEEE International*, pages 470–473. IEEE, 2010. 76

[133] H Katori, M Takamoto, T Takano, I Ushijima, T Ohkubo, K Yamanaka, N Ohmae, Y Aso, A Shoda, T Ushiba, et al. Prospects for frequency comparison of Sr and Hg optical lattice

clocks toward 10^{-18} uncertainties. In *Frequency Control Symposium (FCS), 2012 IEEE International*, pages 1–6. IEEE, 2012. 76

[134] S Johnson. *Narrow Linewidth Lasers for use with Neutral Strontium as a Frequency Standard*. PhD thesis, University of Birmingham, 2013. 90

[135] Yu Levin. Internal thermal noise in the ligo test masses: A direct approach. *Physical Review D*, 57(2):659, 1998. 90

[136] JS Raaj Vellore Winfred. *Investigation of Collisional Losses and Decoherence in a 1-D Optical Lattice Clock with ^{88}Sr*. PhD thesis, University of Hannover, 2010. 105

[137] S Häfner, S Falke, C Grebing, S Vogt, T Legero, M Merimaa, C Lisdat, and U Sterr. 8×10^{-17} fractional laser frequency instability with a long room-temperature cavity. *Optics Letters*, 40(9):2112–2115, 2015. 107, 113

[138] DG Matei, T Legero, S Häfner, Ch Grebing, R Weyrich, W Zhang, L Sonderhouse, JM Robinson, J Ye, F Riehle, et al. 1.5 μm lasers with sub-10 mHz linewidth. *Physical review letters*, 118(26):263202, 2017. 107

[139] S Blatt, Jan Westenkær Thomsen, GK Campbell, AD Ludlow, MD Swallows, MJ Martin, MM Boyd, and J Ye. Rabi spectroscopy and excitation inhomogeneity in a one-dimensional optical lattice clock. *Physical Review A*, 80(5):052703, 2009. 108, 110, 112